

The Pennsylvania State University

The Graduate School

Department of Chemistry

**BIOLOGICAL AND ARTIFICIAL MODEL SYSTEMS TO INVESTIGATE  
FUNDAMENTAL PROPERTIES AND STRUCTURES  
RELATED TO EXOCYTOSIS**

A Dissertation in

Chemistry

by

Kelly L. Adams

© 2010 Kelly L. Adams

Submitted in Partial Fulfillment  
of the Requirements  
for the Degree of

Doctor of Philosophy

May 2010

The dissertation of Kelly L. Adams was reviewed and approved\* by the following:

Andrew G. Ewing  
Professor of Chemistry  
Professor of Neural and Behavioral Sciences  
J. Lloyd Huck Chair in Natural Science  
Dissertation Advisor  
Chair of Committee

Anne M. Andrews  
Associate Professor of Molecular Toxicology

Thomas E. Mallouk  
DuPont Professor of Materials Chemistry and Physics

Peter J. Butler  
Associate Professor of Bioengineering

Barbara J. Garrison  
Shapiro Professor of Chemistry  
Head of the Department of Chemistry

\*Signatures are on file in the Graduate School

## ABSTRACT

Neurotransmitter release via exocytosis, a fundamental process facilitating synaptic transmission in the brain, has been investigated by use of single or multiple carbon fiber microelectrodes, and by pairing with complementary optical microscopy techniques. The use of pheochromocytoma (PC12) and lipidic, artificial soybean liposome cell model systems are presented as means to examine the physical properties and structures influencing exocytotic release, specifically fusion pore size and stability, lipid membrane mechanics and composition, and pharmacological manipulation with a neuromodulator. First in Chapter 2, the effects of elevated osmolarity on neurotransmitter secretion from PC12 cells are presented. The number of pre-spike “feet” and the amount of transmitter released during these feet measured by carbon fiber amperometry were notably increased compared to control, a finding strongly suggesting that membrane mechanics play a modulatory role in presynaptic release by prolonging the lifetime of the fusion pore. Next in Chapter 3, the fabrication and characterization of a seven-barrel carbon fiber microelectrode array are presented. The tightly packed, individually addressed microelectrodes can be used to monitor exocytotic release from PC12 cells and events have been resolved at the sub-cellular level. In Chapter 4, the inhibitory effect of estrogen on depolarization-induced release of dopamine from PC12 cells is discussed. This effect is dose-dependent and involves N-type voltage-gated calcium channels, both results that have not been reported previously for this neuromodulator. Two concentrations of estrogen (10 nM and 50  $\mu$ M) elicit release; however, intracellular calcium imaging reveals that calcium influx is significantly

decreased for 10 nM E2, whereas it is unaffected for 50  $\mu$ M E2. This suggests two probable mechanisms for estrogen: one involving voltage-gated calcium channels at low, physiological estrogen concentrations and another altering cell function at higher pharmacological estrogen concentrations. Such dissimilarity is important to consider when postulating a neuroprotective mechanism for estrogen. The thesis moves to the direct measurement of the dimensions of a lipid nanotube present in an artificial cell model for exocytosis in Chapters 5 and 6. A difference is shown to exist between situations when a micropipette is attached to the lipid nanotube which is then attached to a liposome (the tube-only case) versus when there is a vesicle at the end of the micropipette (the two-vesicle configuration case). A method to electrochemically measure the inner diameter of the lipid nanotube is presented in Chapter 5 and these measurements as well as the differences between the tube-only and two-vesicle cases are compared with a theoretical model considering the different elastic free energy components of the entire system. Membrane composition and the effect of increased lipid concentration in the membrane are further explored in Chapter 6. Lipid composition has a direct effect on the measured size of the lipid nanotube, therefore implicating a more active role for phospholipids in influencing sizes of nanostructures in nature. Lastly in Chapter 7, a summary of this thesis as well as suggested future research directions aimed at furthering the understanding of neurotransmitter release are presented.

## TABLE OF CONTENTS

List of Figures.....	ix
List of Tables.....	xi
List of Equations.....	xii
Acknowledgements.....	xiv
 Chapter 1. Exocytosis and Electrochemical Methods.....	 1
Introduction.....	1
Developments in modifications of microelectrodes.....	2
Single cell amperometry: details of the method to explore exocytotic release.....	5
Recent achievements exploring dopamine and catecholamine release.....	7
Lipid incubation appears to affect the biophysics of exocytosis.....	7
L-DOPA loading of cells fills the halo not the dense core.....	10
Multiple populations of vesicles in catecholamine-containing cells.....	11
Is exocytotic release the same at the top and bottom of a cell?.....	12
Fluorescence imaging for monitoring intracellular calcium affecting exocytosis.....	13
Electroporation for biological and artificial cell manipulation and analysis.....	14
Scope of the Thesis.....	19
References.....	21
 Chapter 2. High osmolarity and L-DOPA augment release via the fusion pore in PC12 cells.....	 27
Introduction.....	27
Experimental Methods.....	30
Cell culture.....	30
Reagents and Solutions.....	31
Electrode preparation and experimental setup.....	31

Data acquisition and data analysis.....	32
Amperometry experiments.....	33
Statistical analysis.....	33
Results and Discussion.....	33
Amperometric release via the fusion pore under hypertonic conditions.....	34
Foot parameters as a function of osmolarity.....	34
Mechanical regulation of release via the fusion pore under high osmolarity conditions.....	37
Model to explain the effect of high osmolarity on the biophysics of release via the fusion pore.....	42
Conclusions.....	46
References.....	47
Chapter 3. Spatially and temporally resolved single-cell exocytosis utilizing individually addressable carbon microelectrode arrays.....	50
Introduction.....	50
Experimental Methods.....	52
Chemicals.....	52
Fabrication of carbon MEAs.....	52
Electrochemical Apparatus.....	55
Scanning Electron Microscopy.....	55
Finite-Element Simulations.....	56
Results and Discussion.....	56
Surface and size characterization by SEM.....	56
Steady-state voltammetric response of the two-fiber MEAs.....	56
Finite-element simulation of the steady-state diffusive flux at a two-fiber MEA.....	60
Voltammetric response of a seven-fiber MEA.....	62
Amperometric detection of neurotransmitter release from single PC12 cells: an electrochemical array image.....	68
Resolving concurrent exocytotic events in single-cell amperometric detection using multi-fiber MEAs.....	70
Conclusions.....	72
References.....	73

Chapter 4. Estradiol inhibits depolarization-induced exocytosis in PC12 cells via N-type voltage-gated calcium channels.....	78
Introduction.....	78
Experimental Methods.....	79
Materials.....	79
Solutions.....	79
Cell culture.....	80
Carbon fiber amperometry.....	80
Electrochemical data acquisition and analysis.....	81
Intracellular calcium imaging and analysis.....	83
Results.....	84
Estradiol inhibits depolarization-evoked exocytosis.....	84
Estradiol modulates calcium influx initiated by depolarization with $K^+$ .....	86
Estradiol inhibition of exocytosis depends on N-type voltage-gated calcium channels.....	89
Discussion.....	89
References.....	97
Chapter 5. Steady-state electrochemical determination of lipidic nanotube diameter utilizing an artificial cell model.....	99
Introduction.....	99
Experimental Methods.....	102
Chemicals and materials.....	102
Liposome preparations and manipulations.....	102
Microscopy and digital video recording.....	103
Electrode fabrication and electrochemical data acquisition.....	105
Tube radius measurements.....	105
Results and Discussion.....	106
Initial nanotube measurements.....	106
Comparison of tube measurements in the two-liposome and tube-only configurations.....	108
Modeling the difference in the trend of diameter between nanotube configurations.....	111

Conclusions.....	117
References.....	119
 Chapter 6. Lipid membrane composition controls the diameter of a lipid nanotube in an artificial cell model for exocytosis.....	122
Introduction.....	122
Experimental Methods.....	126
Chemicals and materials.....	126
Liposome preparations and manipulations.....	126
Nanotube radius measurements and calculations.....	126
Results and Discussion.....	130
Lipid composition affects intrinsic curvature in lipid nanotubes.....	130
Electrochemical measurements of lipid nanotube diameter.....	131
Conclusions.....	137
References.....	139
 Chapter 7. Future Directions and Thesis Conclusions.....	141
Introduction.....	141
Hypotonic conditions and cellular release.....	141
Exploiting the spatial resolution of microelectrode arrays.....	143
Coupling microelectrode arrays with calcium imaging.....	143
Utilizing microelectrode arrays in conjunction with E2.....	144
Elucidating the involvement of an estrogen membrane receptor in the mechanism by which E2 inhibits exocytosis.....	144
Lysolipid addition and estimation of nanotube size.....	145
Measuring a lipid nanotube constructed from a liposome-lipid nanotube system within a “blebbed” cell.....	146
Inducing lipid phase separation within the liposome-lipid nanotube system.....	146
Conclusions.....	147
References.....	149



## LIST OF FIGURES

Figure 1-1. Basic introduction to amperometric detection of exocytosis at single cells....	8
Figure 1-2. Formation and distension of a vesicle in an artificial cell model of exocytosis.....	18
Figure 2-1. Amperometric data from a single PC12 cell.....	35
Figure 2-2. Amperometric foot characteristics.....	38
Figure 2-3. Optical micrographs of PC12 cells.....	41
Figure 2-4. Model of exocytotic vesicle fusion occurring from PC12 cells under different osmolarity conditions.....	43
Figure 3-1. Schematic drawing of carbon fiber MEAs.....	54
Figure 3-2. Scanning Electron Microscopy of carbon fiber MEAs.....	57
Figure 3-3. Steady-state voltammograms of a two-fiber MEAs.....	58
Figure 3-4. Geometry of the electrochemical cell used for numerical simulations.....	61
Figure 3-5. Comparison of experimental and simulated data of the normalized steady-state limiting current at a two-fiber MEA.....	63
Figure 3-6. Simulated distribution of steady-state diffusive flux at the cross section of a 5- $\mu\text{m}$ two-fiber MEA as a function of the interelectrode distance.....	64
Figure 3-7. Steady-state voltammetric response of a seven-fiber MEA.....	65
Figure 3-8. Fast-scan voltammetric response of a seven-fiber MEA.....	67
Figure 3-9. Optical image of MEA experimental setup, seven representative amperometric traces collected from one seven-fiber MEA, and summary of normalized number of exocytotic events per channel.....	69
Figure 3-10. One-second amperometric trace illustrating concurrent release events.....	71
Figure 4-1. Representative amperometric traces of exocytosis.....	87
Figure 4-2. Dose response curves for the effect of E2 on exocytosis.....	88

Figure 4-3. Comparison of the effects of E2 on exocytosis for selected cell types.....	90
Figure 4-4. Potassium-evoked intracellular calcium levels are affected by E2 application.....	92
Figure 4-5. Calcium entry during cell stimulation is reduced by low levels of E2.....	93
Figure 4-6. E2-induced inhibition of exocytosis depends on N-type VGCCs in PC12 cells.....	95
Figure 5-1. Schematics of tube-only and two-vesicle configurations and representative current versus time trace illustrating typical change in current measured.....	104
Figure 5-2. Representative amperometric “staircase” measurement.....	109
Figure 5-3. Measured current versus inverse of the nanotube length for different model configurations.....	112
Figure 5-4. Calculated diameter versus nanotube length for different model configurations.....	113
Figure 5-5. Model of the two-vesicle and tube-only configurations.....	116
Figure 6-1. Chemical structures of PC and PE and schematics of physical structures present in model system.....	125
Figure 6-2. Schematic of tube-only configurations and representative current versus time trace illustrating typical change in current measured.....	129
Figure 6-3. Measured current versus inverse of the nanotube length for different membrane compositions.....	134
Figure 6-4. Calculated diameter versus nanotube length for different membrane compositions.....	135
Figure 6-5. Average nanotube diameter for different membrane compositions.....	136

**LIST OF TABLES**

Table 6-1. Membrane composition for liposome preparations.....	128
--	-----

## LIST OF EQUATIONS

Equation 3-1. Steady-state limiting current for a disk-shape microelectrode.....	56
Equation 3-2. Steady-state limiting current for a hemispherical microelectrode.....	59
Equation 4-1. Treatment ratio for reporting inhibition of exocytosis.....	82
Equation 4-2. Percent inhibition for estrogen treatments.....	83
Equation 4-3. FURA-2 ratio calculation based on fluorescence intensities.....	84
Equation 4-4. FURA treatment ratio for calcium imaging.....	84
Equation 4-5. Treatment ratio for Group 2 cells.....	85
Equation 4-6. Treatment ratio for Group 1 cells.....	85
Equation 5-1. Fick's first law of diffusion.....	106
Equation 5-2. Rearrangement of Equation 5-1 with the assumption of a constant concentration gradient.....	107
Equation 5-3. Rearrangement of Equation 5-2.....	107
Equation 5-4. Solving Equation 5-3 for radius.....	107
Equation 5-5. Solving Equation 5-4 for change in current.....	110
Equation 5-6. Elastic free energy of the membrane.....	115
Equation 5-7. Elastic free energy of the overall system.....	115
Equation 5-8. Elastic free energy of the neck interaction for the two-vesicle configuration.....	117
Equation 5-9. Elastic free energy of the neck interaction for the tube-only configuration.....	117
Equation 6-1. Radius of a cylindrical nanotube.....	130
Equation 6-2. Solving Equation 6-1 for change in current.....	131
Equation 6-3. Elastic free energy of the membrane.....	133

Equation 6-4. Free energy of a membranous nanotube of a specified length.....133

Equation 6-5. Equilibrium radius of a nanotube.....133

## ACKNOWLEDGEMENTS

To say that “many people” helped me to complete this dissertation would be a gross understatement. In my effort to formally acknowledge **all** who have assisted me scientifically and personally, I sure hope I do not forget anyone!

I was fortunate to be guided for the past 5 years by my research advisor, Andy Ewing. His continuous, unfaltering enthusiasm for science is contagious and has made his research group a true privilege to be a part of. I am grateful for all of the opportunities Andy has afforded me over the years, including attending several scientific meetings around the globe (England, Spain, Mexico, and 4 PittCons), moving across the Atlantic to continue evolving as a scientist at the University of Gothenburg in Sweden, and sparking my interest in Tang Soo Do that I will [hopefully] continue practicing for many years to come. Above all, thank you for treating me like I was a member of your own family and not simply a grad student brain on a stick.

Next I would like to acknowledge all of the Penn State faculty who have participated as members of my committee: Professor Anne M. Andrews, Professor Thomas E. Mallouk, and Professor Peter J. Butler for serving as my final defense committee in Sweden (in person or via Skype) and Professor Christine D. Keating, Professor Erin D. Sheets, and Professor Ryan S. Clement for serving as my comprehensive exam committee. I benefited greatly from the discussions generated during these sessions, and I also learned what they called Sponge Bob in France.

The following chapters would surely not exist without a supportive cast of characters around the lab. First, thank you to my lab mates who I have had the opportunity to coauthor papers with: Johan Engelbrektsson, Dan Eves, Michael Heien, Sarah Luber, Marc Maxson, Lisa Mellander, Maja Puchades, Leslie Sombers, Nate Wittenberg, and Bo Zhang. Next, thank you to my collaborators outside of the PSU/GU network: Professor Christian Amatore for his discussions about the osmolarity data presented in Chapter 2; Dr. Remco H.S. Westerink for his continuous involvement in interpreting (and re-interpreting) the tangled web that estrogen weaves as shown in Chapter 4; Professor Roger Karlsson for his insight into the complex world that is working with artificial cell networks (presented in Chapters 5 and 6); and Professor Marina Voinova for developing the complementary theoretical explanation that helped explain our experimental observations contained within Chapters 5 and 6. A special thank you to Ann-Sofie Cans for not only being a phenomenal collaborator (and cheerleader) for Chapters 5 and 6, but for being an exceptional friend. Our many conversations have been invaluable with you always giving me sound advice. I will always remember that there is no danger on the roof...and that somewhere someone is picking coconuts.

I would like to thank all of the past and present AEGrp-ers members I had the pleasure of working alongside and getting to know: Gulnara Safina, Yoshiko Niimura, Bo Zhang, Yan Dong, Maja Puchades, Niklas Strömberg, Johan Engelbrektsson, Leslie Sombers, Paula Ream Powell, Tracy Paxson, Sara Ostrowski, Nate Wittenberg, Dan Eves, Marc Maxson, Dean Santamaria-Capetanelis, Angélique Blackburn, Junior Philip, Mike Kurczy, Mike Santillo, Imee Arcibal, Nick Kuklinski, Paul Piehowski, Anar Pitre,

Monique Makos, Donna Omiatek, Carina Berglund, Lisa Mellander, Ingela Lanekoff, Jenny Bergman, Maria Svensson, Jennifer Smith, Amanda Weaver, and Sarah Lubner. I look forward to hearing about your many successes and thank you again for being willing consumers of my baked goods. A special thanks to Tammy Sauter for being ever-so patient with all of the purchasing nightmares I seemed to create for her. Your chocolate payment is in the mail.

A big “tack kram” to the members of the 4<sup>th</sup> floor in the Kemihuset at GU. I will miss the twice daily fikas. Titta på sälen! To the dedicated members of Göteborg TSD Club: Tang Soo! We will all meet and train again at a black belt clinic in the near future, I just know it.

I also owe a great deal of gratitude to my relentless personal cheerleaders outside of lab: my friends and family. Amanda B, I am in debt to you for keeping the train on the tracks and introducing me to several fabulous television series. Jays, thank you for providing my thesis writing soundtrack. Abby, thanks for cluing me in on the secret. Nick, tack for undertaking this wild Svenska adventure with me and smuggling Ben & Jerry’s with baby spoons into the movie theater. Be some careful. Carina, tack så mycket för att min svenska interpreter. Jag skulle ha gått förlorade utan dig. Ola, jag kommer att sakna den bästa karate partner och jag kan inte vänta på din och Anna Ananas bröllop. Johan, tack för skrek åt mig i vetenskapens namn och införa mig till Guinness. Den personliga helvete titel är allt ditt.

Katie and Steve, thanks for being the best older sister and brother in-law I could ever ask for. I owe you guys a vacation with free baby-sitting! Taylor, you are not old enough to read this big book yet, but when you are, Auntie Puppy will take you for ice



cream. And last, but not least, a big thank you to my mom, the hardest working person I know. Thank you for the countless sacrifices you made to ensure Katie and I had the best. Your encouragement and unconditional love have helped make me into the person I am today, and I hope I have made you proud.

## **Chapter 1**

### **Exocytosis and Electrochemical Methods**

#### **Introduction**

Electrochemistry in ultra-small environments has emerged as an increasingly important technique for fundamental studies of single cell neuronal communication and release and reuptake of chemical messenger molecules as well as cellular imaging and small-scale electroporation applications. The development of electrochemical methods for detection of neurotransmitters began with the ground-breaking work of Adams<sup>1</sup> and has progressed to the point where it is now possible to detect the release of a neurotransmitter from a single vesicle, first demonstrated in the seminal work by Wightman and co-workers.<sup>2, 3</sup> In the pioneering experiments, a carbon fiber electrode 5  $\mu\text{m}$  in diameter was placed adjacent to a bovine adrenal chromaffin cell isolated in a culture dish. The cell was then stimulated to release either by chemical or mechanical means.

Understanding chemistry and structure at the single cell level are areas of great interest in the biological and medical sciences. Books have been written on this broad topic.<sup>4</sup> In neuroscience, knowledge of the chemical composition and dynamics of single nerve cells should lead to better models of the cellular neurotransmission process. The key dynamic event in neuronal communication is exocytosis. This is a process that has been extensively investigated for several decades.<sup>5, 6</sup> The process of exocytosis can be summarized as the docking of vesicles (storage compartments) to the cell membrane and subsequent release of the contents to the extracellular space by fusion of the vesicular and

cellular membranes. This process allows the conversion of an electrical signal (action potential) to a chemical signal (messenger release and receptor recognition), which is necessary for exocytotic communication between cells.

Methods to observe and to quantify individual exocytotic events have traditionally revolved around electron microscopy and patch-clamp capacitance measurements.<sup>7</sup> Wightman and co-workers published their pioneering work in 1990 showing that they could directly monitor individual exocytotic events involving easily oxidized messengers on the millisecond time scale by use of amperometric measurements at microelectrodes.<sup>3</sup> This was first applied by Wightman's group to adrenal chromaffin cells<sup>2</sup>, followed shortly by Neher's group.<sup>8</sup>

#### **Developments in modifications of microelectrodes.**

Carbon fiber microelectrodes were developed in several laboratories in the late 1970s for work *in vivo*. Leading this development were the Wightman<sup>9, 10</sup> and Gonon<sup>11, 12</sup> groups who applied this tool to neuroscience. The method was a major breakthrough for several reasons. First, the carbon fiber electrodes are biocompatible and can therefore carry a current while maintaining sensitivity to reductants, thus increasing the working lifetime of an electrode. Second, carbon fibers as small as 5  $\mu\text{m}$  were available, making it possible to develop very small probes that cause little tissue damage. For *in vitro* work developed later, carbon fiber electrodes were advantageous as they were highly resistant to strain and could be placed firmly against cell surfaces without physically breaking, thus providing greater sensitivity and reproducible measurements. For a more in-depth discussion of the factors affecting electrode sensitivity, selectivity, and temporal response, refer to the paper by Cahill and coworkers.<sup>13</sup>

Electrodes used for studying single cells are usually constructed by first aspirating a single carbon fiber through a glass capillary. The capillary is then pulled using a commercial pipette puller, producing two long-tapered fiber-containing pipettes. Each is later cut at a cross sectional diameter of 8 to 10  $\mu\text{m}$  on a microscope using a scalpel blade. Cut electrodes are immersed in freshly prepared high quality epoxy to create a tight seal between the glass tip and carbon fiber. Finally, no more than a few hours before experiments, electrodes are beveled on a rotary microgrinder to produce a finely-polished, angled tip.<sup>14, 15</sup> Working electrodes are generally prepared from 5 to 10  $\mu\text{m}$  diameter carbon fibers. The signal-to-noise ratio improves as the electrode size approaches the size of the detection area of interest, but larger electrodes can detect a greater number of electrochemical events.<sup>13, 16</sup>

A great deal of work has been carried out to develop better electrodes for measurements at single cells and some of the more interesting work is summarized here. Electrode sensitivity requires the electrode surface to be free of adsorbed molecules, such as proteins and oxidized products.<sup>13, 17</sup> Several groups, however, have modified the working electrode surface in hopes of enhancing electrode sensitivity and/or selectivity.<sup>18-20</sup> A common modification to enhance cation detection is through the application of a thin coating of Nafion<sup>®</sup>, a perfluorinated cation-exchange polymer. Anions are primarily excluded by this thin barrier while cations are able to pass and accumulate at the electrode surface, thus improving their detection, particularly in central nervous system studies.<sup>17, 21-23</sup> Due to this unique exclusionary property, Nafion<sup>®</sup>-coated carbon fiber microelectrodes can be utilized to differentiate between neurochemicals possessing similar oxidation potentials if they are differentially charged, for example

dopamine and ascorbic acid. Electrode response time, however, can be compromised when coating with a thin film of Nafion<sup>®</sup> and a significant loss in temporal resolution may occur. Wightman's group recently modified 10- $\mu$ m carbon fiber microelectrodes via the reduction of 4-sulfobenzenediazonium tetrafluoroborate to create an electroactive surface that has enhanced sensitivity to cationic species, specifically dopamine, without a severe loss of electrode response time.<sup>24</sup> These modified electrodes, unlike those coated with Nafion<sup>®</sup>, also allow anionic species to diffuse to the electrode surface, thus not limiting detection to cationic species alone. Moreover, the sensitivity for dopamine and other positively-charged analytes was increased by a factor of 5 compared to unmodified electrodes, a significant increase compared to an enhancement of 1.5 at best attainable with Nafion<sup>®</sup> coating.<sup>24</sup>

Single-walled carbon nanotubes have also been used to modify carbon fiber electrodes in an effort to improve detection of molecules at the single cell and sub-cellular level. Cheng and coworkers fabricated ultra-small (100-300 nm in diameter) carbon fiber nanoelectrodes via flame-etching followed by immersing the tips into a solution of suspended single-walled carbon nanotubes. The electrodes were subsequently dried, yielding tips covered with sheets of single-walled carbon nanotubes which effectively increased the working surface area of the electrode.<sup>25</sup> Combined with the fine intrinsic electrical properties of single-walled carbon nanotubes, these modified electrodes improved the limit of detection of select neurotransmitters when characterized with cyclic voltammetry. For example, unmodified, ultra-small carbon fiber nanoelectrodes exhibited detection limits on the order of 76 nM, whereas the same electrode geometry modified with single-walled carbon fiber nanotubes resulted in a

detection limit of 7.7 nM.<sup>25</sup> Both the improved sensitivity and the small size of these particular electrodes make them potentially useful in ultra-small environments as high-quality detectors with good temporal and spatial resolution.

Fabrication of electrode surfaces in conjunction with a photoresist has also been explored. Orwar, Weber and coworkers controlled the electroactive area of a carbon fiber working electrode by electrodepositing a negative photoresist onto an exposed carbon fiber microelectrode surface.<sup>26</sup> The face of the tip was then exposed using a xenon arc lamp, subsequently removing the resist layer upon immersion in the developing solution. Experimental parameters, such as temperature of the photoresist solution and the length of time the photoresist was exposed to light, strongly influenced the photoresist thickness and area of exposed electroactive surface, respectively; thus, fine adjustments to the photoresist removal procedure would allow one to reproducibly fabricate an electrode of a specific size as well as to be able to effectively increase the electroactive surface area without making a fresh electrode.<sup>26</sup> Likewise, Wightman and coworkers used a photoresist/pyrolysis method to fabricate carbon ultramicroelectrodes from tungsten microelectrodes substrates.<sup>27</sup> Electrodes made in this way still exhibited electrochemical properties comparable to their glass enclosed fiber counterparts, but an additional dimension of flexibility and rigidity inherent in tungsten microelectrodes was obtained. Furthermore, since these electrodes lack a “bulky” glass capillary encasement, a tightly configured array format of individual electrodes might be possible, thus allowing spatial and temporal information to be conserved within an ultra-small cellular environment.<sup>27</sup>

**Single cell amperometry: details of the method to explore exocytotic release.**

Amperometric experiments involve setting the electrode at potentials sufficient to oxidize molecules near the electrode surface at a diffusion-limited rate. In constant potential amperometric mode, a change in the concentration of an easily oxidized species results in a concomitant change in the oxidation current. Integrating the current of such a transient provides the charge passed which, by Faraday's law ( $N=Q/nF$ ), is directly related to the number of molecules oxidized. Amperometry has been used to study exocytosis in primary cultures,<sup>3, 10, 28, 29</sup> immortalized cell lines,<sup>30, 31</sup> brain slices,<sup>32</sup> and at intact neurons *in vivo*.<sup>33, 34</sup> My thesis will focus on works using single cells.

In general, candidate cell systems have been limited to those that release an oxidizable substance, usually a catecholamine, serotonin, or tyrosine/tryptophan-containing peptide. Immortalized cultures permit single, isolated cells to be studied, while primary cultures offer the advantage of cells that can be studied in the context of a network, continuing to receive information from adjacent cells. Amperometry is well suited to measuring secretion from cells because of its ability to quantify release from vesicles on the millisecond time scale (Figure 1-1).<sup>16</sup> To carry out amperometry at single cells, a small electrode is placed near the cell and held at a potential where oxidation is diffusion limited. Stimulant is applied with a small pipette (Figure 1-1A) to cause exocytosis. This results in current transients when oxidizable species are released. The first experiment to measure exocytosis used adrenal cells and the catechols norepinephrine and epinephrine were detected.<sup>2, 3</sup> The general oxidation reaction for catechols is shown in Figure 1-1B and a typical current-time trace (in this case at a pheochromocytoma cell) is shown in Figure 1-1C. The number of molecules detected can be calculated by Faraday's law as discussed above and shown in Figure 1-1D. Estimates

of the distance between an electrode placed flush against the cell and the cell membrane surface suggest that a small solution filled gap of about 300 nm exists.<sup>35, 36</sup>

The shape of amperometric peaks is characteristic of the various aspects of the release event. Specifically, the half-width of the peak (full width at half maximum) measures the duration of the release event. The rise time, typically the time it takes to change from 10% to 90% of the peak height, relates to the time it takes the fusion pore to open. Thus, basic amperometric measurements are suitable for providing information about the amount of transmitter released, the duration of each event, and the opening of the fusion pore.

#### **Recent achievements exploring dopamine and catecholamine release.**

**Lipid incubation appears to affect the biophysics of exocytosis.** Recent work employing amperometric detection *in vitro* aims to capitalize on the ability of amperometry to detect small oxidative current changes of molecules like dopamine (corresponding to quantities as small as a few zeptomoles), to obtain sub-millisecond kinetic information about secretory event release processes, or both.<sup>28</sup> Recently, this methodology has been used to study the biophysics of the exocytosis process focusing on the membrane composition. Amatore and coworkers have used short (2-3 min) incubations of adrenal cells with different lipids to demonstrate that the shape of the lipid might affect the rate of release.<sup>37</sup> The Ewing laboratory has used the amperometric method to demonstrate that dopamine release from PC12 cells (pheochromocytoma cells) is altered upon three-days incubation with 100  $\mu$ M phospholipids.<sup>38</sup> This neuron-like, immortalized cell line is as an excellent model system to work with due to its large, circular size, ease in culturing and manipulation, and robust nature.<sup>39</sup> Although these



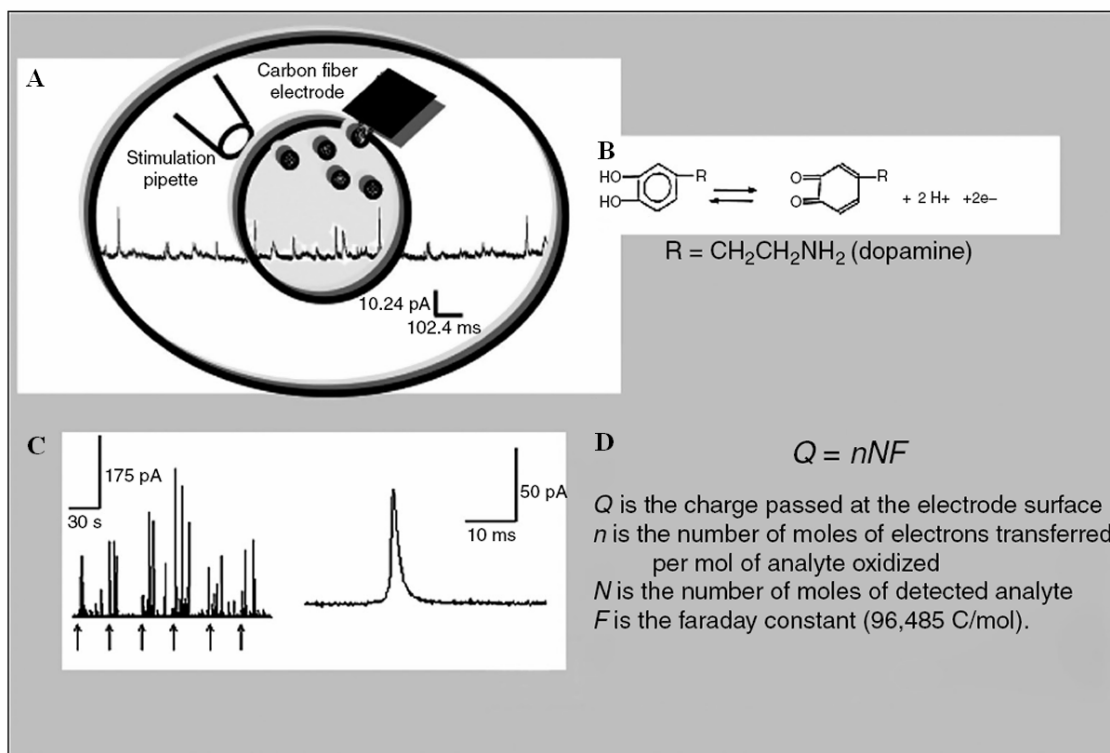


**Figure 1-1.** Basic introduction to amperometric detection of exocytosis at single cells. (A) Foreground image is the typical setup for amperometry for a single cell. Exocytosis is stimulated by a pipette containing a stimulant, and release is monitored by a carbon fiber electrode. The background image shows typical amperometric data. (B) The oxidation reaction for catecholamines. The catecholamine is oxidized to the orthoquinone form, losing two electrons. (C) Left trace shows a series of stimulations, denoted by the arrows, and the electrochemical responses detected after each stimulation. The right hand trace shows a single amperometric current transient. (D) Faraday's equation, which is used to determine the amount of material released during exocytosis. (Reproduced from Sombers et al.,<sup>71</sup>).

cells do not form functional synapses to neighboring cells, they provide an excellent model to examine pre-synaptic cellular machinery. In these experiments, phosphatidylserine incubation increased the number of events elicited by a high potassium stimulus, whereas phosphatidylcholine reduced the quantal size (total amount of transmitter released) per event. Furthermore, phosphatidylethanolamine accelerated the rate of the release process resulting in a shortened average halfwidth and decay time and increased the average peak amplitude of amperometric measurements. In contrast, phosphatidylcholine incubation decreased the rate of the release process by lengthening the halfwidth and decay time while decreasing the average peak amplitude. These data are exciting and support a phospholipid-based mechanism to regulating cell-to-cell communication by altering local membrane composition, thereby impacting exocytosis machinery.

Enhancements of secretion were also observed for another similar incubation protocol. PC12 cells differentiated with nerve growth factor and subsequently treated with 1 mM lithium for two days exhibited a greater frequency of stimulant-evoked release without noticeable changes to the quantity and rate of release.<sup>40</sup> Electron microscopy, however, revealed a lack of increase in the number of secretory vesicles per unit area in these treated cells, but an overall increase in vesicular diameter (~15%). Alongside an immunoblotting assay, electrochemical measurements in this work compliment the observation that lithium, a common therapeutic for bipolar disorder, changes dense core vesicle protein expression by altering secretion machinery and generating a therapeutic response.<sup>40</sup>

**L-DOPA loading of cells fills the halo not the dense core.** Release of dopamine from PC12 cells was augmented by loading them with L-DOPA and exocytosis under both physiological and hypertonic conditions has been monitored with amperometry.<sup>41</sup> A majority of the loaded dopamine was hypothesized to be preferentially stored in the halo region of the vesicle rather than the dense protein core of the vesicle. Under high osmolarity conditions (hypertonic), the dense core matrix does not fully dissociate during exocytosis.<sup>42</sup> Therefore, a relatively larger amount of the release observed under hypertonic conditions is attributed to expulsion of material held in the clear halo region of the vesicle, an area not commonly noted to be an important storage location for transmitter when compared to the dense core matrix. Amperometry data reflected statistically similar peak area increases (26-36%) for both isotonic and hypertonic conditions after loading with L-DOPA, therefore implying supplemental transmitter preferentially stays in the halo regardless of osmolaric conditions. Conversely, Amatore and coworkers have also investigated exocytosis under varying osmolaric conditions using carbon fiber amperometry on bovine chromaffin cells that release catecholamines.<sup>43</sup> Here the release frequency and the average amount of catecholamine released notably increased under hypotonic conditions (low osmolarity). These findings support the swelling of the dense core more favorably under such conditions. Moreover, this finding may be explained by the presence of two different populations of vesicles: the first being of small content and favorably release under isotonic conditions (83% of events vs. 35% at hypotonic) and the second of larger content and more favorably released at hypotonic conditions (65% of events versus 17% at isotonic conditions).<sup>43</sup> However, additional reports from Amatore and coworkers<sup>44</sup> and Wightman and coworkers<sup>45</sup> showed the total

amount of neurotransmitter secreted per vesicle for chromaffin cells under hypo-osmotic conditions did not change compared to isotonic conditions, suggesting this area remains highly controversial.

**Multiple populations of vesicles in catecholamine-containing cells.** Multiple population types of catecholamine vesicles have been suggested, based on results obtained with carbon fiber amperometry, in several cell lines including the large dopamine cell of *Planorbis corneus*<sup>33</sup> and PC12 cells.<sup>46</sup> Tse and coworkers also propose the existence of multiple vesicle populations in rat chromaffin cells.<sup>47</sup> In these cells, each population (small, medium, and large quantal release (Q) granules) can be manipulated separately by lengthening culture duration or simultaneously via co-culturing with cyclic AMP. When culture duration was extended from 1 day to 3 days, the overall detected average quantal size decreased with both small and large Q granule populations changing their distribution proportionalities (each to a different degree). Additionally, introduction of cAMP to the culture media resulted in an increase in the overall average Q for the cell as well as an increased release amount for each vesicle population without significant changes to the distribution proportions for each Q subpopulation. Probable mechanisms for this increased release from all granule sizes triggered by the addition of cAMP include, but are not limited to, provoked increase in catecholamine synthesis, improved reuptake of free catecholamine to all granules sizes, fused multiple granules, and dissolving of the dense core matrix.<sup>47</sup> Similarly, enhanced catecholamine release from bovine chromaffin cells was attributed to molecular interaction with D1 dopaminergic receptors.<sup>48</sup> The time required to reestablish initial cellular calcium levels after a stimulus was optimized by decreasing the length of high-potassium stimulus application

(from 2 s to ~0.5 s). This resulted in the observation of more release events after the second potassium stimulation and this effect could be blocked by a D1 antagonist (SCH-23390). Even more release events following the second potassium stimulation could be evoked by another D1 agonist (SKF-38393). The number of events was unaffected by the D2 antagonist, raclopride. These findings imply that a D1-like receptor on bovine chromaffin cells plays a key role in catecholamines promoting release of themselves within the same cell.<sup>48</sup>

**Is exocytotic release the same at the top and bottom of a cell?** All of the amperometric data discussed to this point has been acquired from the top of the cell surface. It is worth noting here a recent study by Amatore and coworkers in which they discovered that events detected from the top of the cell differed in terms of release dynamics and frequency from those monitored at the bottom of cells directly adhered to the electrode surface.<sup>49</sup> This disparity is extremely important when results are compared for techniques that examine similar phenomena in different geometric set-ups (i.e. amperometry vs. total internal reflectance fluorescence microscopy).<sup>49</sup> When monitoring events with amperometry above and below the cell, those events originating from the top of the cell demonstrated a faster rise time and halfwidth, but the average flux of electroactive material was 40% of that for events monitored below the cell. Several hypotheses were suggested for these findings, the most convincing of which centered on membrane dynamics. The cell surface is firmly affixed to the electrode surface when monitoring release from the bottom compared to the top of the cell where the electrode is lightly contacted with the cell membrane. Thus, the cell membrane under the cell is not as efficient at incorporating new membrane from fusing vesicles and might not flow as

easily. It also seems possible that different vesicle populations exist at each pole of chromaffin cells. These data, collected in different geometric configurations must be carefully interpreted both analytically and biologically to avoid erroneous conclusions.<sup>49</sup>

### **Fluorescence imaging for monitoring intracellular calcium affecting exocytosis.**

Pairing complementary analytical techniques, such as fluorescence microscopy with carbon fiber amperometry, is highly advantageous when investigating complex effects neuromodulators may have on transmitter release. Specifically, calcium entry following cell membrane depolarization is known to induce exocytotic release of dopamine.<sup>50</sup>

The basic principle of fluorescence can be briefly summarized as the excitation of a fluorophore from its ground state to an excited state via absorption of a photon. Following relaxation to the lowest vibrational level of the excited state, a photon of a longer wavelength (i.e. lower energy) is emitted. Experimentally, excitation and emission wavelengths are specific to the selected dye molecule and are set with bandpass filters. Furthermore, the emission intensity is typically measured with a CCD camera.

There are numerous fluorescent calcium indicators available, enabling changes in calcium concentrations ranging from low nanomolar to high micromolar levels to be quantified.<sup>51</sup> A majority of these calcium indicators are derived from calcium-chelating agents, such as EGTA, and have originated from the works of Roger Tsien and coworkers.<sup>52</sup> One example probe is FURA-2, a ratiometric dye used in Chapter 4 of this thesis. This dye can be excited at two different wavelengths (340 and 380 nm) and a ratio comparing the emission intensities generated from each excitation wavelength can be calculated. When calcium enters the cell upon depolarization and binds to FURA-2, the

absorption maximum shifts from 380 nm toward 340 nm. This results in an increased ratio since the intensity of the emission from the 340 nm excitation increases while the intensity of the emission from 380 nm excitation decreases. The use of a ratio instead of raw fluorescence intensity makes the measurements largely independent of dye loading efficiency and photobleaching, common problems encountered when performing live-cell time-lapsed experiments. Therefore, utilizing a ratiometric fluorescence method to monitor changes in intracellular calcium in combination with amperometric detection to record individual dopamine release events allows for the correlation of intracellular calcium levels with dopamine release or vice versa, adding a new dimension to data interpretation.

### **Electroporation for biological and artificial cell manipulation and analysis.**

Examining the composition and functioning chemical processes inside intact cellular environments remains an exciting area of study with much to be learned. To probe the internal environment of a cell while maintaining cell viability, electroporation methods have been developed to passively introduce into a cell a numerous collection of antisense agents, fluorescent dyes, pharmacological stimulants, and other relatively small molecules normally unable to permeate cell membranes.<sup>53-56</sup> Traditionally, a strong electric field exceeding the transmembrane potential (and thus creating small pores in the plasma membrane) is applied in pulses to a bulk population of suspended cells and the agent to be introduced is administered via the bathing solution.<sup>57-59</sup> Typically the field is generated by passing large voltage pulses between two large, fixed millimeter-sized electrodes positioned on either side of the cells to be electroporated. This creates a broad, unfocused electric field useful for bulk transfection applications. Lundqvist and

coworkers developed the first single-cell electroporation scheme, which takes advantage of the small dimensions of carbon fiber electrodes to generate more localized, high electric fields.<sup>60</sup> With a concentrated electric field produced at the electrode tip, individual or smaller groupings of cells could now be addressed.

Since then, other single-cell electroporation methods have been developed (for a more detailed discussion of the various single-cell electroporation methodologies available, please see the review by Orwar, Weber and coworkers<sup>61</sup>). Here, I will highlight specifically a method that generates a highly concentrated electric field at the tip of a fused silica capillary that also transports the agent to be loaded into the cells.<sup>62, 63</sup> These electrolyte-filled capillaries (EFCs) had previously been shown to produce an intense electric field at the capillary outlet when used in capillary electrophoresis.<sup>64</sup> By use of this finely focused electric field near single cells or small groups of cells, materials in small defined quantities can be introduced into single cells via electroporation. A nice illustration of electroporation via an EFC is the introduction of YOYO-1, an RNA-/DNA-intercalating dye, into NG108-15 cells (a glial-neuronal hybrid).<sup>62</sup> Here single cells and/or single cell processes were selectively loaded with YOYO-1 using various potential ranges at a constant cell-EFC tip distance. Different success rates were obtained for each applied potential, most notably when focusing poration to small processes. For an applied potential of 2 kV, only 20% of poration attempts were successful, probably due to insufficient pore formation with such a low potential; however, a potential of 6 kV increased success to 92%. Still higher potentials did not yield greater success, with 10 kV only producing a 70% success rate, exemplifying a potential-dependence on both poration success rate and cell viability.



In addition to the magnitude of the applied potential, other key parameters have also been carefully considered, including pulse duration, distance between the EFC tip and the cell surface, cell size, and cell morphology.<sup>65, 66</sup> In these experiments, the effectiveness of the method to introduce fluorescent dyes into cells or their processes was examined. Briefly, longer pulses (120 ms -150 ms) produced greater decreases in internal fluorescence intensity of cells loaded with fluorescent molecules. This implies more extensive pore formation that allows labeled molecules inside the cell to escape by movement along a concentration gradient. This decreases the total concentration of labeled molecule inside the cell, thus decreasing its fluorescence intensity. EFC tip distances on the order of multiple micrometers (3 or 4) also yielded favorable poration results. With these two parameters simultaneously optimized, over 90% of cells were electroporated with greater than 80% cells remaining viable.<sup>65</sup> Moreover, big, semi-circular cells were more likely to be successfully permeated and remain viable for subsequent studies.<sup>66</sup>

Single-cell electroporation methodology can also be used to manipulate liposomes, or phospholipid membrane-bound vesicles, to mimic the final stages of exocytosis (i.e. after pore formation to expulsion of material by way of membrane distension).<sup>36, 67</sup> Various liposome preparation methods exist, including but not limited to high-pressure extrusion,<sup>68</sup> sonication,<sup>69</sup> and electroformation.<sup>70</sup> Work in this thesis dealing with liposomes was carried out by use of a dehydration/rehydration method<sup>67</sup> to obtain a specific liposome geometry: a unilamellar component comprised of a single lipid bilayer affixed to a multilamellar component consisting of several lipid bilayers.

To create the exocytosis mimic from a liposome, electroporation is used to assist in micromanipulation with an injection pipette filled with a pre-determined solution (buffer, electroactive species, fluorescent dye molecules, etc.). Briefly, an electric field is generated by passing ~30-50-volts in ~1-ms pulses between a 5- $\mu$ m carbon fiber counter electrode and the injection pipette positioned on either side of the unilamellar component (Figure 1-2 a). Like in the single cell electroporation experiments previously described, this electric field creates small openings in the membrane bilayers, allowing the injection pipette to be inserted into the unilamellar interior. Then the injection pipette can be maneuvered to puncture through the second wall of the unilamellar liposome (Figure 1-2 b), again with the assistance of an applied electric field. The pipette is then slowly retracted back into the vesicle interior, bringing with it lipid material adhered to the pipette tip and forming a lipid nanotube between the unilamellar vesicle and the injection pipette (Figure 1-2 c).

To create a liposome inside of a liposome, a small pressure is applied through the injection pipette, creating a small, inner daughter vesicle inside the parent vesicle with a lipid nanotube connection (Figure 1-2 d). Continuous application of pressure through the injection pipette subsequently increases the size of the daughter vesicle and, in turn, decreases the length of the nanotube connection. Eventually the nanotube connection becomes so small that it is comparable to the fusion pore in biological cells (Figure 1-2 f). This structure is energetically unstable, causing the daughter vesicle to distend and subsequently expel its contents, thus mimicking transmitter expulsion from a synaptic vesicle that has fused with the cell plasma membrane (Figure 1-2 g-i). In Chapters 5 and 6, the dimensions of the nanotube created between the daughter and parent vesicle will be

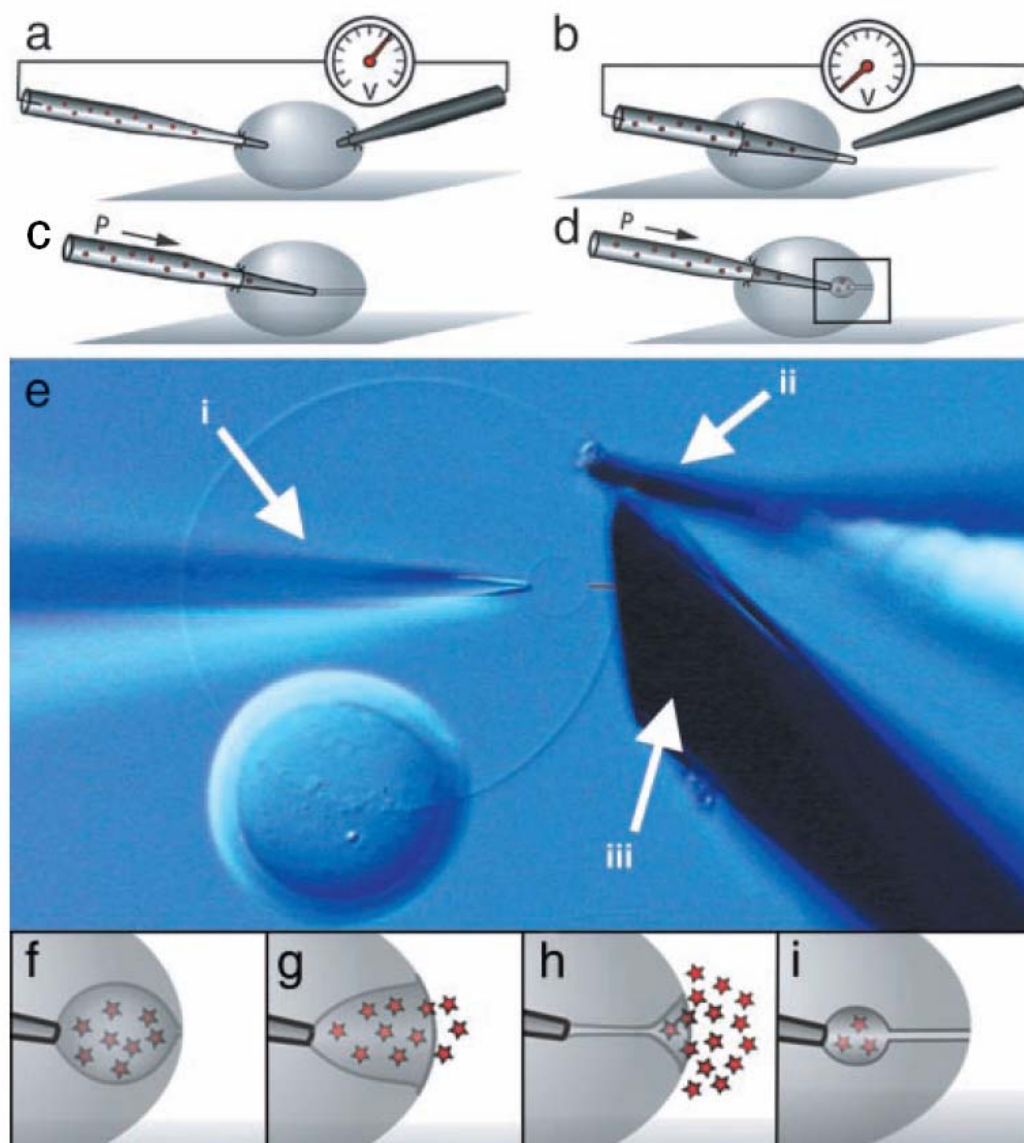


**Figure 1-2.** Formation and distension of the vesicle in an artificial cell model of exocytosis. (a–d) Schematics of an injection pipette inserted into the interior of a unilamellar liposome via electroporation. The injection pipette is pushed through the opposing wall and then retracted back in to the vesicle interior. A lipid nanotube spontaneously forms followed by the formation of a daughter vesicle from applied pressure through the injection pipette tip. (e) Nomarski image of a unilamellar vesicle attached to a multilamellar liposome, injection pipette (i), counter-electrode for electroporation (ii), and beveled carbon fiber working electrode (iii). A small red line depicts the location of the lipid nanotube connecting the two vesicles. (f–i) Inflation of a daughter vesicle due to applied pressure through the injection pipette subsequently shortens the length of the nanotube until the daughter vesicle spontaneously distends, expels its contents, and forms a new daughter vesicle with nanotube attachment. (Reproduced from Cans et al.,<sup>67</sup>.) Scale bar represents 10  $\mu\text{m}$ .

discussed. Work here has been aimed at determining the diameter of the nanotube, as well as to explore the impact membrane composition and lipid curvature has on this structure.

### **Scope of the Thesis**

In this thesis, methods involving electrochemical detection at single or multiple microelectrodes will be discussed in conjunction with complementary optical microscopy techniques to investigate fundamental properties related to exocytosis, an important process facilitating neuronal communication. Both biological and artificial cell model systems have been implemented, allowing membrane mechanics, fusion pore stability, and nanotube size, for example, to be examined in two different yet comparable environments. In Chapter 2, the effects of high osmolarity on vesicular exocytosis from PC12 cells using carbon fiber amperometry are discussed. The fabrication, characterization, and application of a seven-barrel carbon fiber microelectrode array is presented in Chapter 3, demonstrating the high, sub-cellular spatial resolution afforded by such an electrode geometry. In Chapter 4, the inhibitory effect that estrogen has on depolarization-induced release from PC12 cells is presented and two probable neuroprotective mechanisms by which estrogen might inhibit release are proposed. In Chapters 5 and 6, the direct amperometric measurement of a lipid nanotube present in an artificial cell model for exocytosis is presented. An important difference between the tube-only and two-vesicle configurations at shorter nanotube lengths is also addressed in Chapter 5, and a theoretical model is presented considering the elastic free energy of primary components of the model system. In Chapter 6, membrane composition and lipid curvature theory and the effect of increased lipid concentration in the membrane are

explored, implicating a more active role for phospholipids in size determination of nanostructures in nature. Finally, Chapter 7 offers both a summary of the thesis and potential future research directions that should provide new and exciting data relevant to neurotransmitter release at the single-cell and sub-cellular level.

## References

- (1) Adams, R. N. *Anal. Chem.* **1976**, 48, 1126A-1138A.
- (2) Leszczyszyn, D. J.; Jankowski, J. A.; Viveros, O. H.; Diliberto, E. J., Jr.; Near, J. A.; Wightman, R. M. *J. Biol. Chem.* **1990**, 265, 14736-14737.
- (3) Wightman, R. M.; Jankowski, J. A.; Kennedy, R. T.; Kawagoe, K. T.; Schroeder, T. J.; Leszczyszyn, D. J.; Near, J. A.; Diliberto, E. J., Jr.; Viveros, O. H. *Proc. Natl. Acad. Sci. USA* **1991**, 88, 10754-10758.
- (4) Durack, G. R., J.P. *Emerging Tools for Single-Cell Analysis: Advances in Optical Measurement Technologies Cytometric Cellular Analysis*; Wiley: New York, 2000.
- (5) Stamford, J. A.; Justice, J. B. *J. Anal. Chem.* **1996**, 68, 359A-363A.
- (6) Valtorta, F.; Fesce, R.; Grohovaz, F.; Haimann, C.; Hurlbut, W. P.; Iezzi, N.; Tarelli, F. T.; Villa, A.; Ceccarelli, B. *Neuroscience* **1990**, 35, 477-489.
- (7) Neher, E.; Marty, A. *Proc. Natl. Acad. Sci. USA* **1982**, 79, 6712-6716.
- (8) Chow, R. H.; von Ruden, L.; Neher, E. *Nature* **1992**, 356, 60-63.
- (9) Dayton, M. A.; Ewing, A. G.; Wightman, R. M. *Eur. J. Pharmacol.* **1981**, 75, 141-144.
- (10) Ewing, A. G.; Wightman, R. M.; Dayton, M. A. *Brain Res.* **1982**, 249, 361-370.
- (11) Cespuglio, R.; Faradji, H.; Ponchon, J. L.; Riou, F.; Buda, M.; Gonon, F.; Pujol, J. F.; Jouvét, M. *J. Physiol.* **1981**, 77, 327-332.
- (12) Gonon, F.; Buda, M.; Cespuglio, R.; Jouvét, M.; Pujol, J. F. *Nature* **1980**, 286, 902-904.

- (13) Cahill, P. S.; Walker, Q. D.; Finnegan, J. M.; Mickelson, G. E.; Travis, E. R.; Wightman, R. M. *Anal. Chem.* **1996**, *68*, 3180-3186.
- (14) Kawagoe, K. T.; Zimmerman, J. B.; Wightman, R. M. *J. Neurosci. Methods* **1993**, *48*, 225-240.
- (15) Pothos, E. N.; Davila, V.; Sulzer, D. *J. Neurosci.* **1998**, *18*, 4106-4118.
- (16) Travis, E. R.; Wightman, R. M. *Annu. Rev. Biophys. Biomol. Struct.* **1998**, *27*, 77-103.
- (17) Gerhardt, G. A.; Oke, A. F.; Nagy, G.; Moghaddam, B.; Adams, R. N. *Brain Res.* **1984**, *290*, 390-395.
- (18) Friedemann, M. N.; Robinson, S. W.; Gerhardt, G. A. *Anal. Chem.* **1996**, *68*, 2621-2628.
- (19) Gmucova, K.; Weis, M.; Barancok, D.; Cirak, J.; Tomcik, P.; Pavlasek, J. *J. Biochem. Biophys. Methods* **2007**, *70*, 385.
- (20) Wang, Y.; Joshi, P. P.; Hobbs, K. L.; Johnson, M. B.; Schmidtke, D. W. *Langmuir* **2006**, *22*, 9776-9783.
- (21) Kristensen, E. W.; Kuhr, W. G.; Wightman, R. M. *Anal. Chem.* **1987**, *59*, 1752-1757.
- (22) Nagy, G.; Gerhardt, G. A.; Oke, A. F.; Rice, M. E.; Adams, R. N.; Szentirmay, M. N.; Martin, C. R. *J. Electroanal. Chem.* **1985**, *188*, 85-94.
- (23) Rice, M. E.; Oke, A. F.; Bradberry, C. W.; Adams, R. N. *Brain Res.* **1985**, *340*, 151-155.
- (24) Hermans, A.; Seipel, A. T.; Miller, C. E.; Wightman, R. M. *Langmuir* **2006**, *22*, 1964-1969.

- (25) Chen, R. S.; Huang, W. H.; Tong, H.; Wang, Z. L.; Cheng, J. K. *Anal. Chem.* **2003**, 75, 6341-6345.
- (26) Lambie, B. A.; Orwar, O.; Weber, S. G. *Anal. Chem.* **2006**, 78, 5165-5171.
- (27) Hermans, A.; Wightman, R. M. *Langmuir* **2006**, 22, 10348-10353.
- (28) Hochstetler, S. E.; Puopolo, M.; Gustincich, S.; Raviola, E.; Wightman, R. M. *Anal. Chem.* **2000**, 72, 489-496.
- (29) Pothos, E. N.; Mosharov, E.; Liu, K.-P.; Setlik, W.; Haburcak, M.; Baldini, G.; Gershon, M. D.; Tamir, H.; Sulzer, D. *J. Physiol.* **2002**, 542, 453-476.
- (30) Chen, T. K.; Luo, G.; Ewing, A. G. *Anal. Chem.* **1994**, 66, 3031-3035.
- (31) Colliver, T. L.; Pyott, S. J.; Achalabun, M.; Ewing, A. G. *J. Neurosci.* **2000**, 20, 5276-5282.
- (32) Schmitz, Y.; Lee, C. J.; Schmauss, C.; Gonon, F.; Sulzer, D. *J. Neurosci.* **2001**, 21, 5916-5924.
- (33) Chen, G.; Gavin, P. F.; Luo, G.; Ewing, A. G. *J. Neurosci.* **1995**, 15, 7747-7755.
- (34) Schonfu, D.; Reum, T.; Olshausen, P.; Fischer, T.; Morgenstern, R. *J. Neurosci. Methods* **2001**, 112, 163-172.
- (35) Anderson, B. B.; Chen, G.; Gutman, D. A.; Ewing, A. G. *J. Neurosci. Methods* **1999**, 88, 153-161.
- (36) Cans, A. S.; Wittenberg, N.; Eves, D.; Karlsson, R.; Karlsson, A.; Orwar, O.; Ewing, A. *Anal. Chem.* **2003**, 75, 4168-4175.
- (37) Amatore, C.; Arbault, S.; Bouret, Y.; Guille, M.; Lemaître, F.; Verchier, Y. *Chem. Bio. Chem.* **2006**, 7, 1998-2003.



- (38) Uchiyama, Y.; Maxson, M. M.; Sawada, T.; Nakano, A.; Ewing, A. G. *Brain Res.* **2007**, *1151*, 46.
- (39) Greene, L. A.; Tischler, A. S. *Proc. Natl. Acad. Sci. USA* **1976**, *73*, 2424-2428.
- (40) Umbach, J. A.; Zhao, Y.; Gundersen, C. B. *J. Neurochem.* **2005**, *94*, 1306-1314.
- (41) Sombers, L. A.; Maxson, M. M.; Ewing, A. G. *J. Neurochem.* **2005**, *93*, 1122-1131.
- (42) Troyer, K. P.; Wightman, R. M. *J. Biol. Chem.* **2002**, *277*, 29101-29107.
- (43) Amatore, C.; Arbault, S.; Bonifas, I.; Lemaître, F.; Verchier, Y. *Chem. Phys. Chem.* **2007**, *8*, 578-585.
- (44) Amatore, C.; Arbault, S.; Bonifas, I.; Bouret, Y.; Erard, M.; Guille, M. *Chemphyschem* **2003**, *4*, 147-154.
- (45) Borges, R.; Travis, E. R.; Hochstetler, S. E.; Wightman, R. M. *J Biol Chem* **1997**, *272*, 8325-8331.
- (46) Westerink, R. H.; de Groot, A.; Vijverberg, H. P. *Biochem. Biophys. Res. Commun.* **2000**, *270*, 625-630.
- (47) Tang, K. S.; Tse, A.; Tse, F. W. *J. Neurochem.* **2005**, *92*, 1126-1139.
- (48) Villanueva, M.; Wightman, R. M. *Biochem.* **2007**, *46*, 3881-3887.
- (49) Amatore, C.; Arbault, S.; Lemaitre, F.; Verchier, Y. *Biophys. Chem.* **2007**, *127*, 165.
- (50) Cooper, J. R.; Bloom, F. E.; Roth, R. H. *The Biochemical Basis of Neuropharmacology*, 8th ed.; Oxford University Press, 2003.
- (51) Haugland, R. P. *The Handbook: A Guide to Fluorescent Probes and Labeling Technologies*, 10th ed.; Molecular Probes-Invitrogen, 2005.

- (52) Tsien, R. Y. *Biochemistry* **1980**, *19*, 2396-2404.
- (53) Templeton, N. S.; Roberts, D. D.; Safer, B. *Gene Ther.* **1997**, *4*, 700-709.
- (54) Tsong, T. Y. *Biophys. J.* **1991**, *60*, 297-306.
- (55) Weaver, J. C. *J. Cell. Biochem.* **1993**, *51*, 426-435.
- (56) Zimmermann, U. *Biochim. Biophys. Acta. Rev. Biomem.* **1982**, *694*, 227-277.
- (57) Gabriel, B.; Teissie, J. *Biophys. J.* **1999**, *76*, 2158-2165.
- (58) Golzio, M.; Teissie, J.; Rols, M.-P. *Proc. Natl. Acad. Sci. USA* **2002**, *99*, 1292-1297.
- (59) Hibino, M.; Itoh, H.; Kinosita, K. *Biophys. J.* **1993**, *64*, 1789-1800.
- (60) Lundqvist, J. A.; Sahlin, F.; Aberg, M. A. I.; Stromberg, A.; Eriksson, P. S.; Orwar, O. *Proc. Natl. Acad. Sci. USA* **1998**, *95*, 10356-10360.
- (61) Olofsson, J.; Nolkrantz, K.; Ryttsen, F.; Lambie, B. A.; Weber, S. G.; Orwar, O. *Curr. Opin. Biotechnol.* **2003**, *14*, 29-34.
- (62) Nolkrantz, K.; Farre, C.; Brederlau, A.; Karlsson, R. I. D.; Brennan, C.; Eriksson, P. S.; Weber, S. G.; Sandberg, M.; Orwar, O. *Anal. Chem.* **2001**, *73*, 4469-4477.
- (63) Nolkrantz, K.; Farre, C.; Hurtig, K. J.; Rylander, P.; Orwar, O. *Anal. Chem.* **2002**, *74*, 4300-4305.
- (64) Lu, W.; Cassidy, R. M. *Anal. Chem.* **1994**, *66*, 200-204.
- (65) Agarwal, A.; Zudans, I.; Orwar, O.; Weber, S. G. *Anal. Chem.* **2007**, *79*, 161-167.
- (66) Agarwal, A.; Zudans, I.; Weber, E. A.; Olofsson, J.; Orwar, O.; Weber, S. G. *Anal. Chem.* **2007**, *79*, 3589-3596.
- (67) Cans, A. S.; Wittenberg, N.; Karlsson, R.; Sombers, L.; Karlsson, M.; Orwar, O.; Ewing, A. *Proc Natl Acad Sci U S A* **2003**, *100*, 400-404.

- (68) Berger, N.; Sachse, A.; Bender, J.; Schubert, R.; Brandl, M. *Int J Pharm* **2001**, 223, 55-68.
- (69) Woodbury, D. J.; Richardson, E. S.; Grigg, A. W.; Welling, R. D.; Knudson, B. *H. J Liposome Res* **2006**, 16, 57-80.
- (70) Angelova, M. I.; Dimitrov, D. S. *Faraday Discuss. Chem. Soc.* **1986**, 81, 303-311.
- (71) Sombers, L. A.; Hanchar, H. J.; Colliver, T. L.; Wittenberg, N.; Cans, A.; Arbault, S.; Amatore, C.; Ewing, A. G. *J. Neurosci.* **2004**, 24, 303-309.

## **Chapter 2**

### **High osmolarity and L-DOPA augment release via the fusion pore in PC12 cells**

#### **Introduction**

Exocytosis, the process of cellular chemical secretion, is a highly complex process that requires the fusing of two discontinuous lipid bilayer membranes by a group of proteins called the SNARE complex.<sup>1</sup> These proteins are responsible for bringing the plasma membrane into a highly curved dimple, close to a tense secretory vesicle membrane. The resultant structure causes the plasma membrane and secretory vesicle membranes to form a 'hemifusion' intermediate, and completion of fusion by formation of an aqueous pore following rupture of the shared bilayers.<sup>2</sup>

There are clear differences of opinion regarding the structure of the fusion pore. Some hypothesize that it is made of proteins,<sup>3-7</sup> proposing that the fusion pore resembles a gap junction-type channel that is formed by proteins between the vesicle and plasma membranes. Another hypothesis, the stalk model, suggests that although proteins are involved in establishing the pore, this transient structure is formed from the combination and mixing of the vesicular and plasma membranes.<sup>8-12</sup>

When secretory granules fuse with the plasma membrane, there can be a tension-driven flow of lipid through the fusion pore.<sup>13</sup> Whether the fusion pore is transiently made of protein or is purely lipidic, at some point during the exocytotic process the connection between vesicular and plasma membranes must be lipidic, thus membrane biophysics can play a role in modulating the kinetics of pore opening and neurotransmitter release.<sup>9, 10, 14</sup>

One can quantitatively measure exocytotic release using amperometry. The area integrated under amperometric spikes is related by Faraday's law to the number of molecules of neurotransmitter released and subsequently oxidized at the electrode surface.<sup>15</sup> When release through a stable fusion pore precedes full vesicular fusion, it is distinguished in amperometric records of exocytosis as a pre-spike foot.<sup>16, 17</sup> The integrated area under the foot portion of the spike is representative of the number of molecules released through the fusion pore, prior to full fusion. The duration of release during the foot is indicative of the lifetime, or stability, of the fusion pore structure.<sup>18</sup> Finally, the frequency with which amperometric feet are observed is a direct measure of the frequency with which vesicles release neurotransmitter through a stable exocytotic fusion pore as an intermediate state, as opposed to explosive vesicular fusion. Release through the fusion pore that occurs without full fusion, termed 'kiss and run exocytosis', has also been measured with amperometry.<sup>19</sup> In this case, vesicles transiently fuse with the plasma membrane and rapidly pinch back off, effectively recycling back into the cytoplasmic vesicular pool. Transmitters are released through the transient pore, allowing a smaller 'message' to be sent and allowing one vesicle to send several signals without undergoing the full recycling and refilling process. Indeed, the fusion pore structure plays a key role in several modes of vesicular release, and analyses of this intermediate state are particularly interesting in light of recent studies suggesting that the kinetics of vesicular fusion may contribute to the expression of long-term potentiation and thus affect synaptic plasticity.<sup>20, 21</sup>

In previous work from the Ewing laboratory, rat pheochromocytoma (PC12) cell vesicle size has been manipulated (without a significant effect on the size of the vesicular core), and the resulting effects on release via the fusion pore have been characterized.<sup>18</sup> Interestingly, smaller (reserpine-treated) vesicles display a foot in the amperometric record more frequently than control (prior to reserpine treatment). My colleagues and I hypothesize that this result is largely an effect of the membrane tension differential that exists across the fusion pore. Immediately following vesicular fusion with the plasma membrane and pore formation, the vesicular dense core swells resulting in release of core-bound transmitter. Because the dense core of a reserpine-treated vesicle largely fills the vesicle, core expansion should increase the vesicular tension to a greater extent than in the control case, where the core does not occupy as much of the overall vesicular volume. The resultant tension differential across the pore induces transient pore stabilization until membrane flow relieves this tension and full distention of the vesicle can occur. Thus, the fusion pores of smaller vesicles are more significantly stabilized, and amperometric feet occur in the data record more frequently.

High osmolarity was originally shown to cause vesicles to fuse to planar membranes as a means to demonstrate that osmotic swelling is a driving force for full vesicular fusion.<sup>22</sup> Several published reports suggest or provide evidence for a reduced tension in the cell membrane in hyperosmotic solutions.<sup>23-25</sup> In this chapter, high osmolarity saline solution has been extracellularly applied to create a tension differential across the fusion pore. This treatment decreases the plasma membrane tension, and thus the total transpore membrane tension for PC12 cells undergoing exocytosis is decreased. This is opposite

to the prior experiments described above, in which the total tension across the fusion pore was hypothesized to increase upon treatment with reserpine; however, in this chapter presented here, the differential in tension is still from relatively high to relatively low from vesicle to plasma membrane, respectively. Some cells have also been pretreated with L-DOPA, a treatment which serves to increase the amount of catecholamine in the vesicular halo.<sup>26</sup> It was found that treatment with L-DOPA decreases the number of events with a foot.<sup>18</sup> Thus, L-DOPA was combined with hypertonic saline to examine if the effects of L-DOPA would plausibly counter the effect of hyperosmotic solution on the number of feet observed while increasing the fraction released in the foot part of the total event. The key finding is that the percentage of fusion events that exhibit a foot is increased in hypertonic saline as compared to stimulation in isotonic extracellular conditions. In addition, the duration and magnitude of fusion pore release is increased. Treatment with L-DOPA partially reduces the numbers of events observed with a foot in hypertonic saline but increases further the duration and magnitude of the foot events. These results suggest that one part of the mechanism of fusion pore stabilization is plausibly based on membrane biophysics.

### **Experimental Methods**

**Cell culture.** Stock PC12 cells were purchased from the American Type Culture Collection (Manassas, VA) and maintained as described previously.<sup>27</sup> In brief, PC12 cells were grown on mouse collagen IV coated culture dishes (Becton Dickinson, Bedford, MA) in supplemented RPMI-1640 medium. Cells were kept in a 7 % CO<sub>2</sub> atmosphere at

37°C and were subcultured approximately every 7 to 9 days or when confluency was reached. Cells were used for all experiments between days 7 and 12 of subculturing.

**Reagents and solutions.** All reagents were obtained from Sigma and used as received. Isotonic (335 mOsm) physiological saline was prepared with 150 mM NaCl, 5 mM KCl, 1.2 mM MgCl<sub>2</sub>, 5 mM glucose, 10 mM HEPES, and 2 mM CaCl<sub>2</sub>. Hypertonic saline (700 mOsm) was prepared by raising the NaCl concentration to 332 mM. For all solutions, pH was adjusted to 7.4 with concentrated NaOH. Solution osmolarities were confirmed with a vapor pressure osmometer (Vapro, Wescor, Inc., Logan, UT).

**Electrode preparation and experimental setup.** Carbon fiber microelectrodes (5-μm diameter) were constructed as described previously<sup>28</sup> and back-filled with 3 M KCl. Electrode tips were polished at a 45° angle on a diamond dust-embedded micropipette beveling wheel (Model BV-10, Sutter Instrument Co., Novato, CA). Cyclic voltammograms were generated for each electrode in a nitrogen-saturated 0.1 mM dopamine solution (in 0.1 M phosphate buffered saline, pH 7.4), and only electrodes with stable I-E curves were used.

The working electrode was gently lowered onto a single cell using a piezomicropositioner (PCS-750/1000, Burleigh Instruments, Fishers, NY). The close proximity of the electrode to the cell surface was confirmed by a slight deformation in the outline of the cell. Exocytosis was stimulated at approximately 1-min intervals with a 5-s, 20-psi pulse (Picospritzer II, General Valve, Fairfield, NJ) of saline containing 100 mM K<sup>+</sup>. This stimulation saline was of the same osmolarity as the saline used in the cell bath.



All experiments were performed at  $37 \pm 1^\circ\text{C}$ . Culture dishes were warmed using a solid state Peltier heating device (Bionomic System, 20/20 Technology, Inc., Wilmington, NC).

**Data acquisition and data analysis.** Electrodes were held at +0.65 V vs. a silver/silver chloride reference electrode (World Precision Instruments, Inc., Sarasota, FL) using a commercially available patch-clamp instrument (Axopatch 200B; Axon Instruments, Inc., Foster City, CA) configured as described previously.<sup>23</sup> The output was digitized at 5 kHz and filtered at 2 kHz using an internal 4-pole lowpass Bessel filter. Data were displayed in real time (Axoscope 8.1.0.07, Axon Instruments, Inc.) and stored digitally with no subsequent filtering.

Exocytotic spikes were identified and the spike characteristics area (fC),  $t_{1/2}$  (ms), and  $i_{\max}$  (pA), as well as foot area (fC) and foot duration (ms) were determined using Mini Analysis software (Synaptosoft, Inc., Decatur, GA). Signals were designated as spikes if their  $i_{\max}$  values were 5 times the standard deviation of a 1-s portion of stable baseline recorded prior to the first stimulation. The onset of the foot was defined as the time when the signal exceeded the peak-to-peak noise of a 5-ms time segment, and the end of the foot was defined by the inflection point between the foot and the main event. This threshold value was determined by mathematically taking the second derivative of the trace. Averaged signals were generated using Mini Analysis by aligning individual events at their peaks. All peaks identified by the program were visually inspected and unfit peaks were manually excluded from the data sets. Double peaks, those with more than one peak (jagged tops), and those without a smooth decline to baseline were removed.

Additionally “stand-alone” foot signals were removed, as these could not be definitively characterized.

**Amperometry experiments.** Cells were prepared for an experiment by removing culture medium, washing with isotonic saline, adding fresh isotonic (335 mOsm) saline and then placing them onto the stage of an inverted microscope (IM-35, Carl Zeiss, Thornwood, NY).

The protocol for these experiments was as follows. PC12 cells were initially allowed to equilibrate and warm in plain isotonic (335 mOsm) saline for 60 min before beginning amperometric recording. Some cells were loaded with dopamine during this time period by adding 100  $\mu$ M L-DOPA (biosynthetic dopamine precursor) to the incubation solution. This treatment leads to an increase in the volume of the vesicular halo, the clear space between the dense core and vesicular membrane.<sup>26</sup> Next, this saline was replaced with fresh isotonic or hypertonic (700 mOsm) saline, cells were allowed to re-equilibrate and re-warm for 10 min, and were stimulated with a 100 mM K<sup>+</sup> saline solution with NaCl levels balanced accordingly to maintain osmolarity with the extracellular bath. All rinses were done in saline of the same osmolarity as the prior incubation.

**Statistical analysis.** Data sets for foot characteristics from individual cells were pooled to draw conclusions. Data sets were tested for significant differences from isotonic or hypertonic control using the t-test (SigmaPlot, Version 8.0, SPSS, Inc.) Results for all tests were considered significant if associated p values were < 0.05. All values are reported as the mean  $\pm$  SEM and all plots were created using SigmaPlot.

## **Results and Discussion**

**Amperometric release via the fusion pore under hypertonic conditions.**

Amperometry has been used extensively to quantitatively measure neurotransmitter release from a variety of cell types.<sup>29</sup> Briefly, a 5- $\mu\text{m}$  carbon fiber electrode is placed flush on the surface of a PC12 cell, held at a constant potential (+650 mV vs. Ag/AgCl), and the cell is stimulated with high  $\text{K}^+$  solution to release oxidizable molecules via exocytosis (Figure 2-1). The oxidation of molecules (dopamine in this study) at the electrode results in a time resolved current spike that is characteristic of release from a single vesicle. The spike reveals the kinetics of the release event and can be integrated to determine the amount of neurotransmitter released using Faraday's law. In some cases, a prespike foot is observed. This foot has been determined to represent the release of molecules through the fusion pore that is initially present upon fusion of the vesicular and plasma membranes.<sup>16</sup> The duration of the prespike foot is indicative of the lifetime, or stability, of the fusion pore structure. The frequency with which amperometric feet are observed is a direct measure of the frequency of formation of a stable fusion pore.

**Foot parameters as a function of osmolarity.** The percentage of the amperometric events that exhibit feet in records of release from cells stimulated in isotonic and hypertonic salines are compared in Figure 2-2A. Exposure of PC12 cells to hypertonic saline for 10-min did not significantly change the overall number of release events detected; however, it did result in an increase in the number of events where release via the fusion pore was observed. The percentage of exocytotic events displaying a detectable foot was  $44 \pm 2 \%$  under isotonic (control) conditions, and  $57 \pm 3 \%$  under hypertonic conditions ( $p < 0.01$ ). After a 60-min exposure to 100

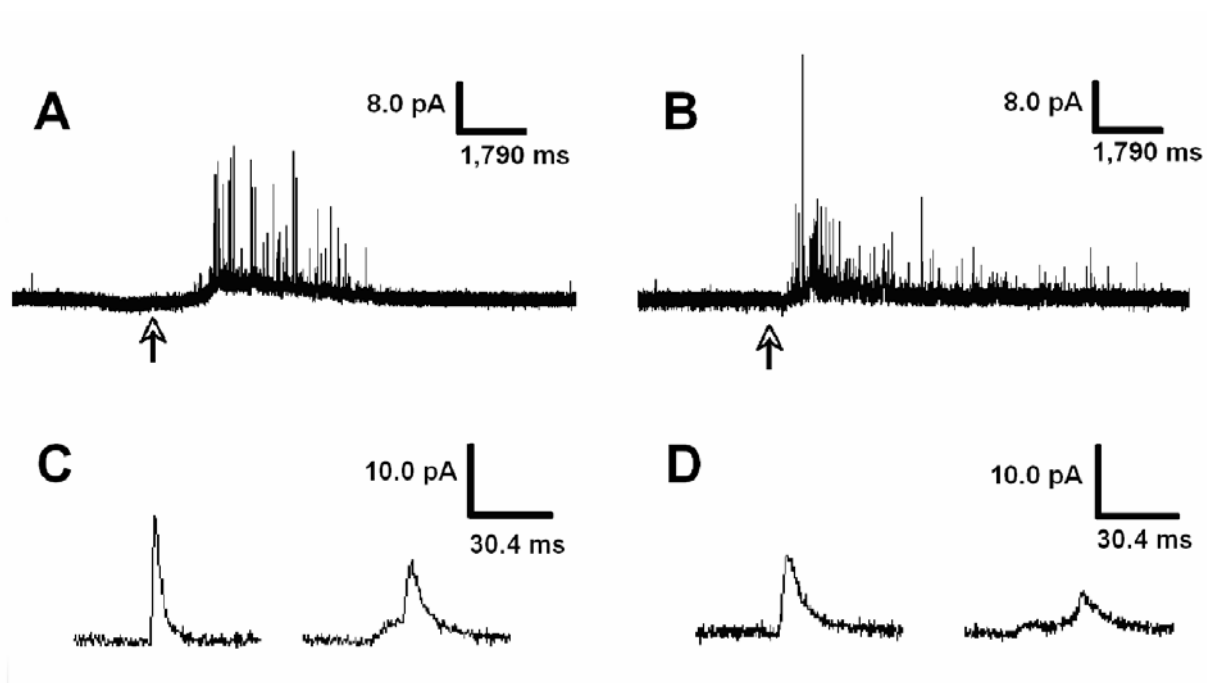


**Figure 2-1.** Amperometric data from a single PC12 cell. Cells stimulated in (A, C) isotonic (335 mOsm) or (B, D) hypertonic (700 mOsm) solutions. Arrow: stimulus (100 mM K<sup>+</sup>). (C, D) Individual amperometric current transients. Left: no discernable foot signal; Right: representative foot.

$\mu\text{M}$  L-DOPA,  $34 \pm 3 \%$  and  $44 \pm 6 \%$  of exocytotic release events exhibited feet for cells stimulated in isotonic or hypertonic extracellular saline, respectively. This difference was not statistically significant at the 95% confidence level ( $p = 0.09$ ).

Foot flux, or the foot area divided by the foot duration, increases under hypertonic conditions. Foot area (Figure 2-2B) and foot duration (Figure 2-2C) data are presented for release events from cells stimulated in either isotonic or hypertonic saline. The mean foot area collected under isotonic conditions was  $2.2 \pm 0.6$  fC. This value increased to  $6 \pm 1$  fC under hypertonic conditions, indicating that 3 times as many molecules were released through the fusion pore ( $p < 0.001$ ). Similarly, treatment with L-DOPA significantly increased both foot area and duration when cells were stimulated in hypertonic saline. Thus, both hypertonic conditions and pre-treatment with L-DOPA serve, at least in part, to increase the number of molecules released through the fusion pore.

Examining the data in Figure 2-2A compared to 2-2C, it is interesting to note that the foot duration should represent the lifetime of the intermediate that leads to full distension of the pore and exocytosis. Presumably the actual lifetimes of the intermediates are symmetrical around a distribution. However, the observed result is usually skewed to longer lifetimes. If the release via the fusion pore is merely leakage through the transient structure then some of the lifetimes will be too short to be detected and the release will be detected for only some percentage of the events. In this case, as the average lifetime of the intermediate increases, the percentage of events that show a detectable foot should increase. This should lead to a correlation between the average lifetime of the foot and

the percentage of events with a detectable foot. This is not observed here. Comparing Figure 2-2A to 2-2C, it is apparent that the average foot duration for spikes in cells treated with L-DOPA and stimulated in high osmolarity extracellular solution is approximately three times greater than the average foot duration for control cells stimulated in isotonic solution. However, there is no obvious difference between the percentage of events with a foot for these two groups of cells. This suggests that the foot is an all or none event and not merely leakage through the fusion pore intermediate. It seems plausible that some exocytosis events are predestined to release in two stages vs. some that open all at once.

The number of molecules released during the amperometric foot was also evaluated and this was compared to the total number of molecules released in both the foot and the larger full exocytosis event. The number of molecules released in the foot expressed as percentage of total release is shown in Figure 2-2D. A larger percentage of total vesicular content was released in the foot portion of the event when cells were stimulated in hypertonic saline, for both saline pretreated and L-DOPA pretreated experimental groups, due to stabilization of the fusion pore structure.

**Mechanical regulation of release via the fusion pore under high osmolarity conditions.** The foot of the amperometric spike displays a large alteration, relative to the rest of the spike, when exocytosis is elicited in high osmolarity saline. Understanding the effect of high osmolarity solution on release via the fusion pore is important because it allows postulation of a lipidic mechanism to, in part, explain stabilization of the fusion pore during the amperometric foot. Upon vesicle fusion with the plasma membrane and

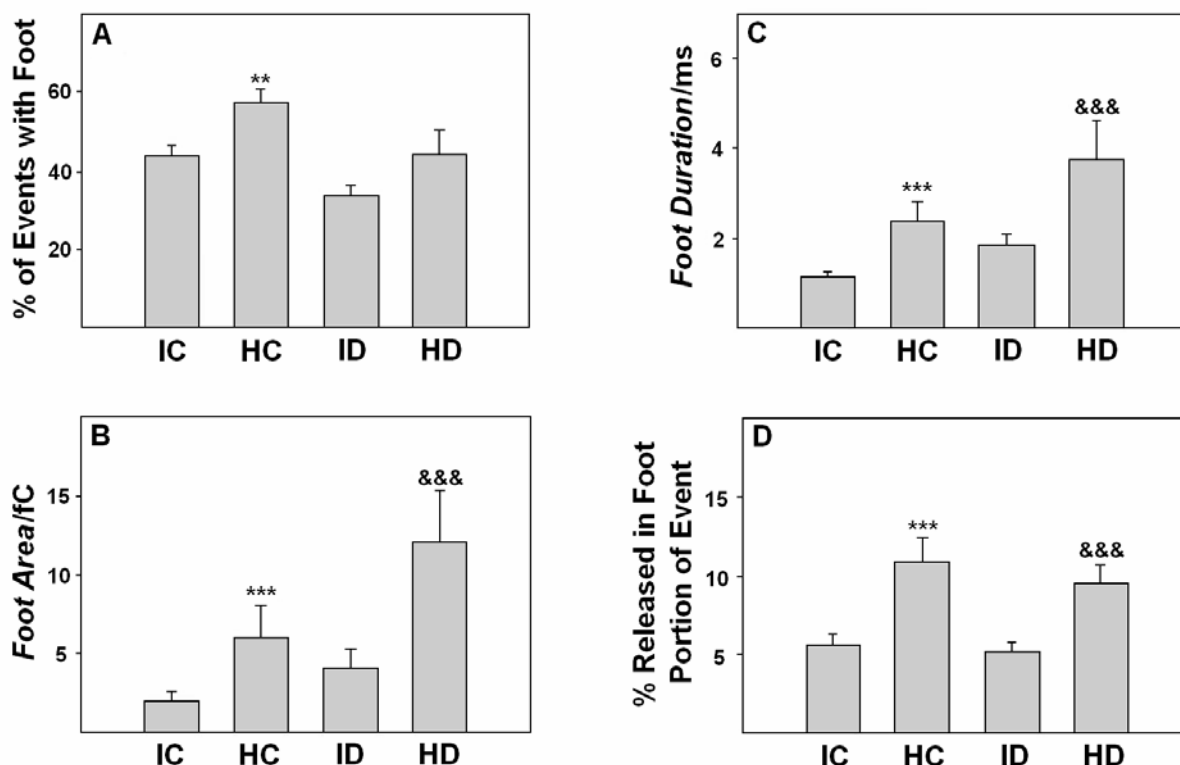


**Figure 2-2.** Amperometric foot characteristics. (A) Frequency of events exhibiting a foot for PC12 cells stimulated at four conditions: isotonic saline after a 60-min exposure to isotonic saline (IC) ( $n = 6$ ), hypertonic saline after a 60-min exposure to isotonic saline (HC) ( $n = 6$ ), isotonic saline after a 60-min exposure to isotonic L-DOPA (ID) ( $n = 5$ ), and hypertonic saline after a 60-min exposure to isotonic L-DOPA (HD) ( $n = 5$ ). An average of  $110 \pm 14$  amperometric spikes comprise the data sets for each group. (B) Foot area, (C) foot duration and (D) the % of the vesicular content released in the foot portion of the event for the same experimental groups. Means are for pooled data. \* and \*\* and \*\*\* are statistically different with  $p < 0.05$  and  $p < 0.01$  and  $p < 0.001$  vs. isotonic control, respectively (t-test). &&& signifies that the hypertonic L-DOPA data set is significantly different from isotonic L-DOPA with  $p < 0.001$  (t-test).

opening of the fusion pore, a mechanical pressure is generated within the vesicle as the dense core expands in response to the rapidly shifting osmolarity.<sup>8</sup> Under hypertonic conditions, dense core dissolution is prevented or significantly slowed, allowing preferential release of dopamine that is not directly associated with the dense core.<sup>18, 30</sup> The data presented here are consistent with this previous finding. The dopamine released via the pore when PC12 cells are stimulated in hypertonic saline and pre-treated with L-DOPA occasionally results in amperometric feet that are large in area and long in duration as compared to the area and halfwidth of the subsequent amperometric spike. The loss of catecholamine from the vesicular halo could contribute to the destabilization of the core structure and affect the rate of core expansion. However, in comparing this hypothesis to the structurally similar adrenal chromaffin cells, it is important to note that the dense core appears to occupy less of the overall vesicle volume in PC12 cells, and thus the mechanical pressure generated by core expansion<sup>8</sup> will have different effects in each cell line. Indeed, hypertonic extracellular saline prevents vesicles in bovine chromaffin cells from proceeding to full fusion until isotonic conditions are restored.<sup>23</sup>

Evans and Yeung have experimentally shown that a lipid nanotube connected to a vesicle constricts when the tension on the vesicle is increased.<sup>31</sup> A nanotube transition state is suggested as an intermediate step in some biological release events.<sup>18</sup> If the fusion pore is, at some stage, considered to be a short lipidic nanotube connecting the vesicle to the cell membrane, then an increased differential tension across the fusion pore should lead to constriction and transient stabilization of the pore structure, stalling the progression of the vesicle to full distension of the membrane. Previous work from this



laboratory has supported this hypothesis by demonstrating that under isotonic conditions smaller vesicles in PC12 cells, which demonstrate an increased dense core to halo volume ratio, exhibit amperometric feet with an increased frequency as compared to larger vesicles with dense cores occupying less of the total vesicular volume.<sup>18</sup> In that work, it was hypothesized that as exocytosis is initiated, an expanding dense core increases tension on the vesicular membrane leading to stabilization of the fusion pore intermediate state. The isotonic data presented here are in agreement with data from this previous study in that the percentage of amperometric events exhibiting feet is higher for saline treated cells than it is for L-DOPA treated cells.

In earlier work, it was hypothesized that the expanding dense core increased tension on the vesicular membrane leading to a tension differential from high inside to low outside and thus stabilizing a pore/nanotube transition state.<sup>18</sup> Here PC12 cells were bathed in hypertonic saline to reduce the already low tension on the cell plasma membrane to cause a tension differential from relatively high in the vesicle to low in the membrane. As expected, and reported before, the cell membranes look somewhat wrinkled in hypertonic solution (Figure 2-3). This is most prevalent shortly after the solution is changed and then the cells appear to partially recover. In this condition, the tension on the plasma membrane is thought to be less than that of the membrane of a connected vesicle, decreasing the total tension across the fusion pore structure and creating a tension differential that should stabilize the fusion pore. The data collected from cells bathed in hypertonic saline (Figure 2-2) are consistent with this idea, indicating that a tension differential due to a decreased total tension on the plasma

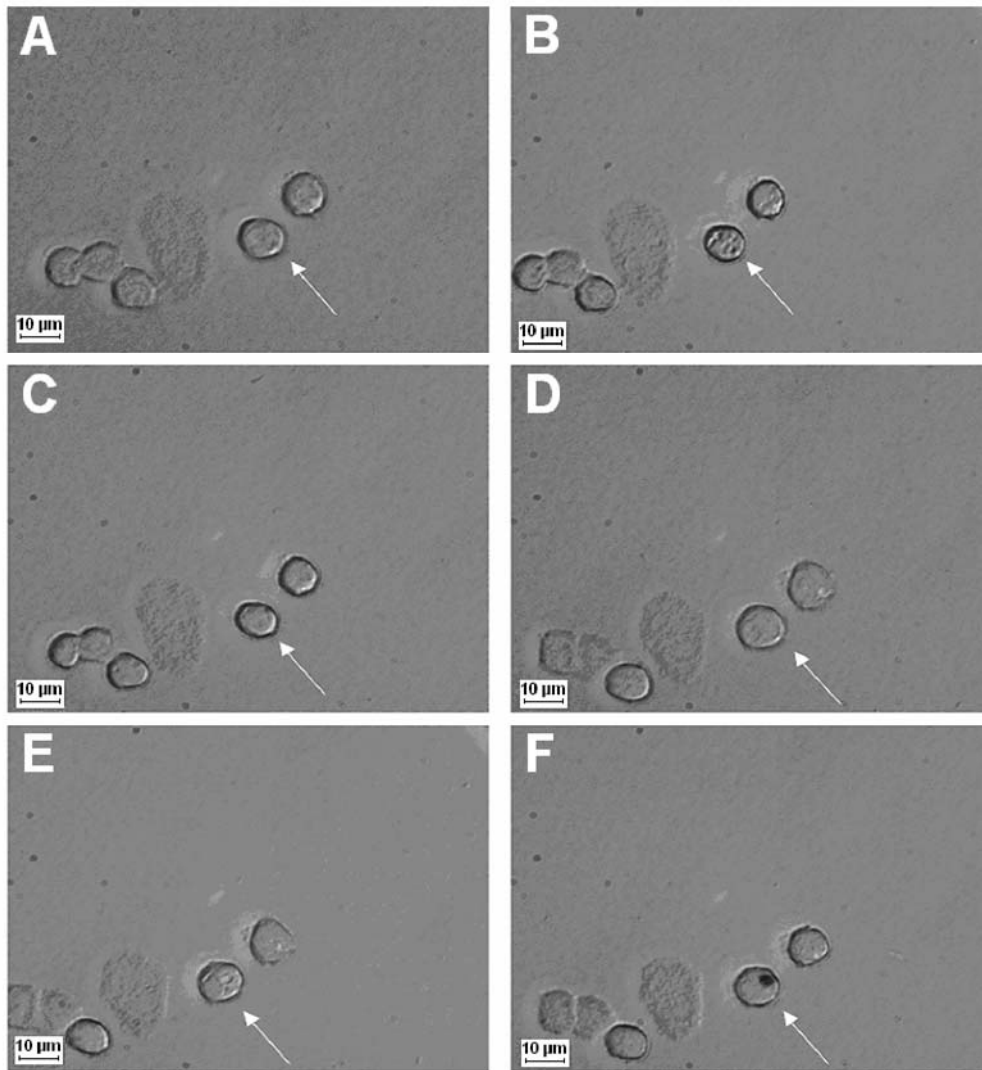


**Figure 2-3.** Optical micrographs of PC12 cells taken with an Olympus IX71 inverted microscope with 600X magnification. These cells were treated with isotonic and then hypertonic saline in sequence. A) Cells in isotonic saline for 10 min, B) in hypertonic saline for 1 min, C) hypertonic saline after 10 min, D) isotonic saline for 60 min, E) hypertonic for 1 min again and F) hypertonic for 10 min. The cell marked by the arrow is notably more wrinkled in hypertonic saline as are the cells flanking it. This wrinkling diminishes after time in hypertonic saline, but is still present.

membrane-fusion pore-vesicular membrane system may slow the destabilization the pore and the onset of full vesicular fusion in PC12 cells. These results are also consistent with theoretical results indicating that the total tension across a lipidic pore determines the rate of pore expansion after membrane fusion.<sup>10</sup> Finally, the results here are consistent with data and discussion published on adrenal cells treated with hyper and hypo-osmotic solutions prior to measuring exocytosis. Adrenal cells treated with hyperosmotic solution have been shown by Amatore and coworkers<sup>24</sup> to reduce the number of exocytosis events and their published theory suggests that the lack of an expanding dense core results in nonrupture or expansion of the fusion pore. That publication does not examine changes in the amperometric feet with hyperosmotic conditions, but interestingly notes that treatment with cholesterol increases the number of feet and their duration. In another publication by Amatore and coworkers hypo-osmotic conditions were examined for effects on the amperometric foot.<sup>25</sup> Under both isotonic and hypertonic conditions, they indicate that increased numbers of events will decrease the tension of the cell membrane thus decreasing theoretically the efficiency of the full fusion event in exocytosis. This is consistent with the data presented here. In addition, they noted a small decrease in the number of events with a foot under hyperosmotic conditions, but the change was not statistically significant. Hence, their data are consistent with data from the study presented here that further examines the mechanics of the fusion pore.

**Model to explain the effect of high osmolarity on the biophysics of release via the fusion pore.** A schematic depiction of the proposed mechanism of fusion pore stabilization when the cells are stimulated in isotonic solution is shown in Figure 2-4A.

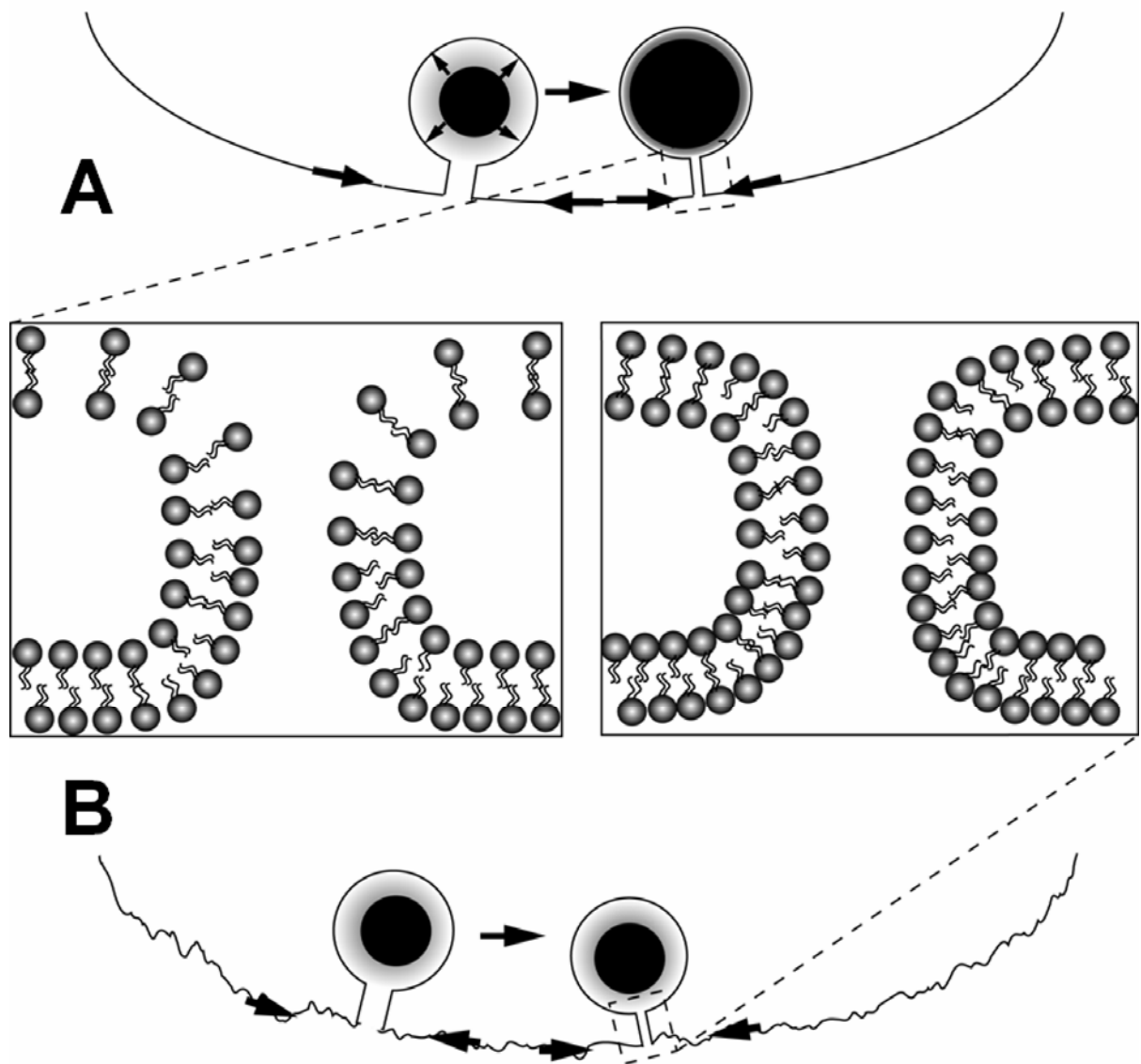


**Figure 2-4.** Model of exocytotic vesicle fusion occurring from PC12 cells stimulated in either isotonic (A) or hypertonic (B) extracellular saline. The magnitude of the membrane wrinkling is exaggerated to make the point that the membrane tension is reduced in hyperosmotic solution.

Here it is hypothesized that in this control condition a tension differential between the vesicular and plasma membranes is rapidly generated owing to pressure from an expanding polymeric dense core. In previous work a model system has been used to suggest that for large vesicles, membrane mechanics provides sufficient energy to drive the opening of the lipidic fusion pore.<sup>32</sup> While it is likely that the protein matrix created by the SNARE complex might require unravelling and an expanding dense core could expedite and regulate this in a mechanism similar to that proposed by Amatore,<sup>8, 33, 34</sup> it certainly appears that membrane dynamics play a role in opening the pore. The proposed hypothesis is that upon opening of the exocytotic fusion pore, the swelling of the dense core matrix produces a fluidic pressure (depicted with inner arrows) on the intravesicular wall, which increases tension on the vesicular membrane as compared to that on the plasma membrane, causing a differential tension from inside to outside. The increased vesicular tension is shown schematically in Figure 2-4A inset by expanding the distance between lipid molecules. Vesicles having a Brownian motion away from the plasma membrane during the time of an open, but stabilized, fusion pore will go through an intermediate state involving a short lipid nanotube. This will lead to a transient constriction of the fusion pore, as shown. Subsequently, the increase in the difference in membrane tension between the vesicular and plasma membranes should result in increased lipid flow from the plasma membrane through the fusion pore (tension-based flow shown by the arrows on the plasma membrane), equilibrating the membrane tension on either side of the pore and thus diminishing its overall stability. This results in an abrupt opening of the pore and full vesicular fusion. A model of exocytosis from PC12

cells placed in hypertonic saline is shown in Figure 2-4B and this is physically different from that in isotonic saline in two distinct ways. Upon opening of the fusion pore, dissociation of the dense core matrix is largely inhibited and thus core expansion does not rapidly increase the tension on the vesicle membrane. A tension differential between the vesicle and plasma membrane exists, however, because tension in the plasma membrane is decreased relative to the control condition. The tension differential along the fusion pore (shown schematically by the change in lipid density from high outside where the tension is low to low inside where the tension is normal) likely leads to stabilization of the pore until lipid flow through the pore equilibrates the tensions and results in full vesicular fusion.

The model proposed here is a simple, yet descriptive membrane-based explanation of the specific data presented. It is to be emphasized that this model is only one part of the overall process of exocytotic release and might only be important for those events where release via the fusion pore occurs. Note that increasing solution osmolarity is not the only method known to alter release from the fusion pore. Work by Jackson and coworkers has demonstrated that genetic manipulation of the proteins that make up the SNARE complex, such as syntaxin (syt), synaptobrevin (syb) and SNAP-25, can result in altered fusion pore characteristics.<sup>35</sup> These genetic manipulations seem to affect the fusion pore only in the cases of point and double point mutations, including mutation of residues lining the pore when it is thought to be at the stage of being mostly protein.<sup>36</sup> Overexpression of wild-type syt, syb and SNAP-25 does not alter foot duration nor catecholamine flux through the fusion pore, indicating no change in relative pore stability due to changes in

the ratio of SNARE proteins.<sup>35</sup> In the experiments presented here, no deliberate genetic mutations were carried out; therefore it is unlikely that changes to fusion pore stability imparted by the SNARE complex are leading to the changes in foot characteristics observed under these conditions.

In hypertonic solution there is the possibility of altered SNARE functionality and subsequent effects on vesicle docking and fusion due to high salt conditions. However, no difference in the frequency or total number of events in hypertonic solutions compared to isotonic conditions was observed; therefore, the increased salinity of hyperosmotic solutions does not denature the SNARE complex or affect any of its constituent proteins in an adverse way.

## **Conclusions**

The model presented here addresses the lipid contribution to fusion pore formation in a manner consistent with the general model of protein-initiated fusion pore formation. Although the characteristics of SNARE complex proteins dominate interactions during fusion pore formation and might indeed at some point in the process constitute the pore, the fusion pore must at some point enter a primarily lipidic structure to fully integrate into the plasma membrane. The evidence presented in this chapter indicates that during this latter stage of fusion membrane biophysics contribute to the stability of the fusion pore. These data help to elucidate the modulatory role of lipid membrane mechanics in vesicular exocytosis, a concept that is important when considering models to describe altered release through the fusion pore and its effects on synaptic transmission.

## References

- (1) Burgoyne, R. D.; Morgan, A. *Physiol Rev* **2003**, 83, 581-632.
- (2) Monck, J. R.; Oberhauser, A. F.; Fernandez, J. M. *Mol Membr Biol* **1995**, 12, 151-156.
- (3) Bai, J.; Wang, C. T.; Richards, D. A.; Jackson, M. B.; Chapman, E. R. *Neuron* **2004**, 41, 929-942.
- (4) Gong, L. W.; Hafez, I.; Alvarez de Toledo, G.; Lindau, M. *J Neurosci* **2003**, 23, 7917-7921.
- (5) Han, X.; Wang, C. T.; Bai, J.; Chapman, E. R.; Jackson, M. B. *Science* **2004**, 304, 289-292.
- (6) Lindau, M.; Alvarez de Toledo, G. *Biochim Biophys Acta* **2003**, 1641, 167-173.
- (7) Ventriglia, F.; Maio, V. D. *Biol Cybern* **2003**, 88, 201-209.
- (8) Amatore, C.; Bouret, Y.; Travis, E. R.; Wightman, R. M. *Biochimie* **2000**, 82, 481-496.
- (9) Chizmadzhev, Y. A.; Kumenko, D. A.; Kuzmin, P. I.; Chernomordik, L. V.; Zimmerberg, J.; Cohen, F. S. *Biophys J* **1999**, 76, 2951-2965.
- (10) Chizmadzhev, Y. A.; Kuzmin, P. I.; Kumenko, D. A.; Zimmerberg, J.; Cohen, F. S. *Biophys J* **2000**, 78, 2241-2256.
- (11) Chanturiya, A.; Chernomordik, L. V.; Zimmerberg, J. *Proc Natl Acad Sci U S A* **1997**, 94, 14423-14428.
- (12) Nanavati, C.; Markin, V. S.; Oberhauser, A. F.; Fernandez, J. M. *Biophys J* **1992**, 63, 1118-1132.



- (13) Monck, J. R.; Alvarez de Toledo, G.; Fernandez, J. M. *Proc Natl Acad Sci U S A* **1990**, *87*, 7804-7808.
- (14) Chizmadzhev, Y. A.; Cohen, F. S.; Shcherbakov, A.; Zimmerberg, J. *Biophys J* **1995**, *69*, 2489-2500.
- (15) Wightman, R. M.; Jankowski, J. A.; Kennedy, R. T.; Kawagoe, K. T.; Schroeder, T. J.; Leszczyszyn, D. J.; Near, J. A.; Diliberto, E. J., Jr.; Viveros, O. H. *Proc Natl Acad Sci U S A* **1991**, *88*, 10754-10758.
- (16) Chow, R. H.; von Ruden, L.; Neher, E. *Nature* **1992**, *356*, 60-63.
- (17) Alvarez de Toledo, G.; Fernandez-Chacon, R.; Fernandez, J. M. *Nature* **1993**, *363*, 554-558.
- (18) Sombers, L. A.; Hanchar, H. J.; Colliver, T. L.; Wittenberg, N.; Cans, A.; Arbault, S.; Amatore, C.; Ewing, A. G. *J Neurosci* **2004**, *24*, 303-309.
- (19) Staal, R. G.; Mosharov, E. V.; Sulzer, D. *Nat Neurosci* **2004**, *7*, 341-346.
- (20) Choi, S.; Klingauf, J.; Tsien, R. W. *Nat Neurosci* **2000**, *3*, 330-336.
- (21) Choi, S.; Klingauf, J.; Tsien, R. W. *Philos Trans R Soc Lond B Biol Sci* **2003**, *358*, 695-705.
- (22) Cohen, F. S.; Akabas, M. H.; Finkelstein, A. *Science* **1982**, *217*, 458-460.
- (23) Borges, R.; Travis, E. R.; Hochstetler, S. E.; Wightman, R. M. *J Biol Chem* **1997**, *272*, 8325-8331.
- (24) Amatore, C.; Arbault, S.; Bonifas, I.; Bouret, Y.; Erard, M.; Guille, M. *Chemphyschem* **2003**, *4*, 147-154.

- (25) Amatore, C.; Arbault, S.; Bonifas, I.; Lemaitre, F.; Verchier, Y. *Chemphyschem* **2007**, 8, 578-585.
- (26) Sombers, L. A.; Maxson, M. M.; Ewing, A. G. *J Neurochem* **2005**, 93, 1122-1131.
- (27) Kozminski, K. D.; Gutman, D. A.; Davila, V.; Sulzer, D.; Ewing, A. G. *Analytical Chemistry* **1998**, 70, 3123-3130.
- (28) Pothos, E. N.; Przedborski, S.; Davila, V.; Schmitz, Y.; Sulzer, D. *J Neurosci* **1998**, 18, 5575-5585.
- (29) Travis, E. R.; Wightman, R. M. *Annu Rev Biophys Biomol Struct* **1998**, 27, 77-103.
- (30) Troyer, K. P.; Wightman, R. M. *J Biol Chem* **2002**, 277, 29101-29107.
- (31) Evans, E.; Yeung, A. *Chem Phys Lipids* **1994**, 73, 39-56.
- (32) Cans, A. S.; Wittenberg, N.; Eves, D.; Karlsson, R.; Karlsson, A.; Orwar, O.; Ewing, A. *Anal Chem* **2003**, 75, 4168-4175.
- (33) Amatore, C.; Bouret, Y.; Midrier, L. *Chem Eur J* **1999**, 5, 2151-2162.
- (34) Amatore, C.; Bouret, Y.; Travis, E. R.; Wightman, R. M. *Angew Chem Int Ed Engl* **2000**, 39, 1952-1955.
- (35) Han, X.; Jackson, M. B. *J Cell Biol* **2006**, 172, 281-293.
- (36) Han, X.; Jackson, M. B. *Biophys J* **2005**, 88, L20-22.

## Chapter 3

### **Spatially and temporally resolved single-cell exocytosis utilizing individually addressable carbon microelectrode arrays (MEAs)**

#### **Introduction**

Neuronal communication is facilitated by the release of chemical messengers, often via a process called exocytosis. In exocytosis, intracellular vesicles containing neurotransmitters fuse with the cell membrane to release their contents into the extracellular space.<sup>1</sup> Such vesicle-fusion processes are known to be triggered by calcium ions and regulated by various membrane proteins (e.g., the soluble N-ethylmaleimide-sensitive factor attachment protein receptor (SNARE) proteins).<sup>2</sup>

Electrochemical methods utilizing carbon-fiber microelectrodes have been extremely useful in the detection of easily oxidizable neurochemicals (e.g., dopamine, epinephrine, 5-hydroxytryptamine, and histamine) from single cells.<sup>3, 4</sup> In a typical experiment, a carbon-fiber microdisk electrode is placed flush with the cell surface. The electrode potential is held constant (in amperometry) or scanned (in cyclic voltammetry) with respect to a reference electrode placed in the extracellular media. Quantitative and qualitative information about neurotransmission can be obtained from *i-t* and *i-V* responses.<sup>5</sup> Experiments using a single carbon-fiber microelectrode provide valuable information such as chemical identity, amount of the neurotransmitter released, event frequency, and kinetic information relating to fusion pore opening.<sup>6</sup> However, information concerning spatial heterogeneity of exocytotic events is difficult to obtain. Such information can be useful in understanding the molecular mechanisms and the chemical basis for regulation of neural secretion. By comparing the number of exocytotic

events recorded simultaneously at two 1- $\mu\text{m}$  carbon microelectrodes placed on the same chromaffin cell, Wightman and coworkers discovered the presence of “hot-spots” (where exocytosis was more frequent) and “cold-spots” (where exocytosis was less frequent) on the same cell.<sup>7</sup> Due to the difficulties in micromanipulation, it is extremely challenging to record from more than one microelectrode concurrently at a single cell. Simultaneously monitoring exocytotic events from multiple subcellular sites of a single cell would be greatly facilitated by microelectrode arrays (MEAs).

MEAs have been intensively studied over the past two decades not only by the chemical community,<sup>8</sup> but also by scientists probing neuronal communication in brain tissue slices,<sup>9, 10</sup> and in cultured networks of neuronal cells. MEAs have also been used in a variety of studies, including drug discovery,<sup>14, 15</sup> diffusion of chemical species in solid electrolyte and electrolyte solutions,<sup>16, 17</sup> and chemical and biochemical sensing. Micro-fabrication technologies have been widely applied in the fabrication of MEAs. Alternative techniques have also been developed. Examples include chemical or electrochemical deposition of metals in nanoporous or microporous materials (polymers<sup>38-42</sup> or glass<sup>43, 44</sup>), chemical etching<sup>45, 46</sup> or micro-patterning<sup>47</sup> on metal-supported self-assembled monolayers (SAMs), and chemically attaching metal nanoparticles onto SAMs at the electrode surface.<sup>48</sup>

Individually addressable MEAs offer many advantages compared to their counterparts, such as high spatial resolution, the possibility of sensing multiple analytes using different microelectrodes in the array, and probing signal transmission in a network of biological cells. The Michael group reported a method of constructing two or four individually addressable carbon ultra-microelectrodes (radii  $\sim 1\ \mu\text{m}$ ) separated by a

distance  $\sim 15\text{ }\mu\text{m}$ .<sup>49</sup> Each carbon fiber was etched into a sharp tip and then electrically isolated by coating the tip with poly(allylphenol). These electrochemical arrays were used to simultaneously probe dopamine release in the brain at multiple sites. In a recent report, Lindau and coworkers micro-fabricated an array of four gold disk electrodes on a chip and recorded exocytotic events simultaneously from these MEAs positioned under a single chromaffin cell.<sup>50</sup> However, due to the patterning of the microelectrodes and relative size of the array compared to the cell, a large fraction of the cell membrane was not directly exposed to the electrode surfaces.

In this chapter, I present the fabrication and characterization of micrometer-sized electrochemical probes containing closely-packed arrays of carbon microdisk electrodes. These MEAs have compatible sizes to individual neuronal cells (10-20  $\mu\text{m}$ ). The fabrication method eliminates the need for complicated wiring allowing several microelectrodes to fit in a small area. Steady-state voltammetry and numerical simulations have been compared to study the overlap of steady-state diffusive flux between adjacent microelectrodes and its effect on the independence of each microelectrode. I also describe differential electrochemical detection of exocytosis on single PC12 cells using an array of seven tightly packed carbon microelectrodes.

## **Experimental Methods**

**Chemicals.** KCl (99.9% Aldrich) and ferrocene methanol ( $\text{FcCH}_2\text{OH}$ , 100%, Aldrich) were used as received. All solutions were made using  $18\text{ M}\Omega\cdot\text{cm}$  water from a Millipore purification system.

**Fabrication of Carbon MEAs.** A single 5- $\mu\text{m}$ -diameter carbon fiber (Amoco, Greenville, SC) was initially inserted into each barrel of a multi-barrel glass capillary

(2B150F-4, 3B120F-4, 7B100F-4, World Precision Instruments), to create electrodes of 2, 3 and 7 barrels (Figure 3-1). Multiple 12-cm long pieces of carbon fiber were isolated from a bundle and immobilized using tape. A home-pulled thin glass capillary ( $\sim 0.4$  mm o.d.,  $\sim 30$  cm long) connected to an in-house vacuum was used to pull a single carbon fiber into each barrel. The thin vacuum glass was pre-inserted into one barrel of the multi-barrel glass capillary. A single carbon fiber was then aspirated into the thin glass capillary. The vacuum capillary was then pulled out from the multibarrel glass, leaving the fiber in the large capillary. The above step was repeated until each barrel was filled with a single carbon fiber. The multi-barrel glass capillary was then pulled using a regular glass capillary puller (P-97, Sutter Instruments) to form two micro-tips. The pulled electrode tip was visually inspected under an optical microscope to ensure the fibers were uniform inside the pulled glass tip. To produce a good seal between the glass and the fibers, the pulled electrode tip was dipped into a freshly prepared epoxy (Epo-Tek, Epoxy Technology) for  $\sim 5$  min and cured in an oven ( $100^\circ\text{C}$ ) for  $> 24$  hours. The electrode tip was cut and polished at an angle of  $\sim 60^\circ$  on a microelectrode beveller (BV-10, Sutter Instruments). Each barrel was then back-filled with silver paint (Dupont). Electrical connection was made using a tungsten rod placed in each barrel. Epoxy was applied to secure the tungsten rods.

The number and the arrangement of the microelectrodes included in the array are pre-selected by using different multi-barrel glass capillaries. Two, three, and seven-barrel glass capillaries are used. The MEAs fabricated in the present research contain exclusively  $5\text{-}\mu\text{m}$ -diameter carbon fibers. The distance between different electrodes is an important parameter in the response of MEAs. Due to the conical shape and tapered tip of

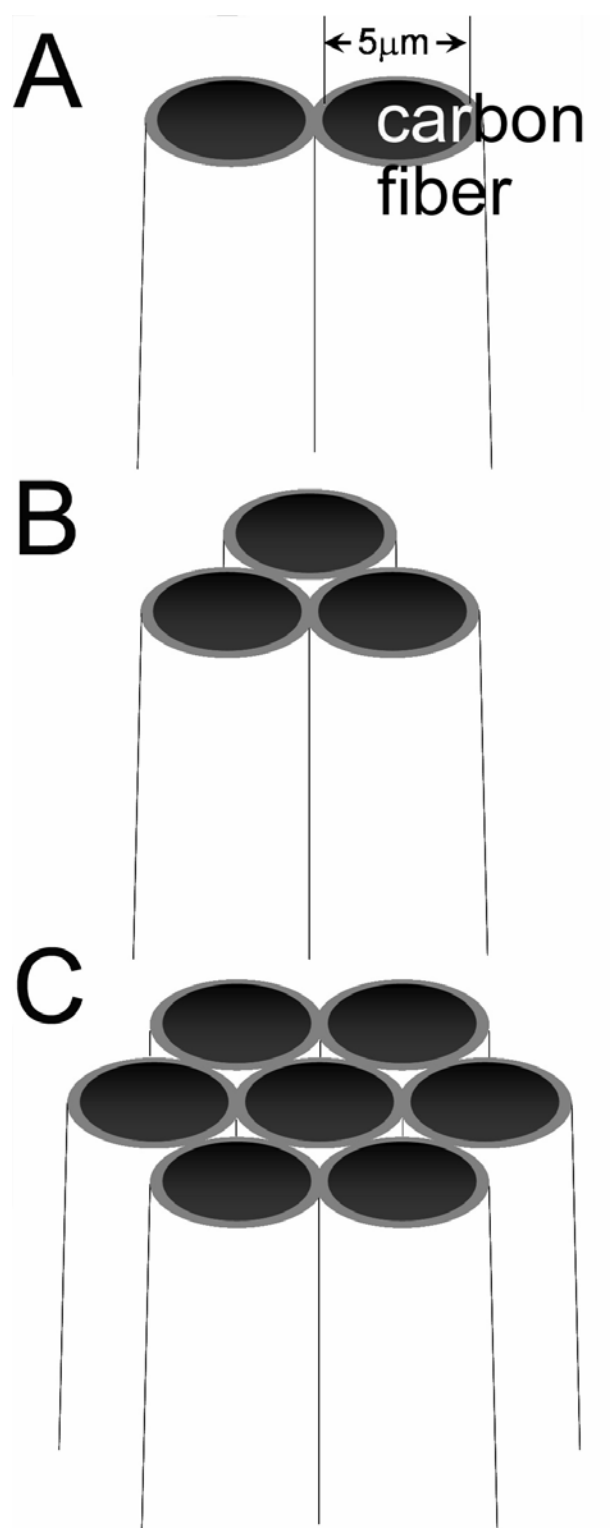


**Figure 3-1.** A schematic drawing of carbon fiber MEAs containing two (A), three (B), and seven (C) microdisks.

the pulled electrode, this geometric parameter can be controlled in the polishing of the electrode. The more electrode material removed by polishing, the larger the inter-electrode distance will be. My coworkers and I have been able to obtain MEAs having inter-electrode distance (center to center) from as small as  $\sim 6\ \mu\text{m}$  to as large as  $100\ \mu\text{m}$ . Insulation is still maintained even when adjacent fibers are separated by sub- $\mu\text{m}$ -thick glass due to the high resistivity of glass ( $> 10^{14}\ \Omega\cdot\text{m}$  for borosilicate glass<sup>55</sup>).

**Electrochemical Apparatus.** A one-compartment, two-electrode cell was employed with the cell and preamplifier in a homebuilt Faraday cage. A silver/silver chloride electrode was used as the reference/auxiliary electrode. Four bipotentiostats (EI-400, Ensmann) were used to perform the multi-channel voltammetric measurements. The triangular waveform was generated from one potentiostat and was output to the other three bipotentiostats. The bipotentiostats were interfaced to a PC computer through a multi-channel data acquisition system (Digidata 1440A, Molecular Devices). Voltammetric responses were plotted using Origin<sup>®</sup> 7.5 (OriginLab<sup>®</sup>). Electrochemical recordings on single PC12 cells were made using an inverted microscope (CK30, Olympus) placed in a Faraday cage. A glass micropipette containing high  $\text{K}^+$  (100 mM) solution was positioned  $\sim 100\ \mu\text{m}$  away to stimulate cell secretion. Each stimulus was applied for 5 s every 45 s at 30 psi using a Femtojet microinjector (Eppendorf). A constant potential (+800 mV) was applied to each carbon microdisk with respect to a single Ag/AgCl reference electrode placed in the cell bathing solution. Other experimental details were performed as previously described.<sup>56</sup>

**Scanning Electron Microscopy.** SEM images of the carbon fiber MEAs were obtained using a FEI Quanta 3D 200 FIB/SEM at the Penn State nanofabrication facilities.



**Finite-Element Simulations.** The steady-state voltammetric response of a double-fiber-array microelectrode was simulated using Comsol Multiphysics® 3.2 software (Comsol, Inc.) on a Dell PC (3GHz CPU, 2GB memory).

## Results and Discussion

**Surface and size characterization by SEM.** Carbon MEAs have been characterized using SEM. Figure 3-2 shows typical SEM images of MEAs containing two, three, and seven microdisks, respectively. The electrodes are structurally well defined and the overall diameters of the three-fiber and seven-fiber MEAs are between 15 and 20  $\mu\text{m}$ , respectively. The 2.5- $\mu\text{m}$ -radius carbon disks are tightly packed together and surrounded by a thin layer of glass (about 1-2  $\mu\text{m}$ ).

**Steady-state voltammetric response of the two-fiber MEAs.** Figure 3-3 shows the steady-state voltammetric response of a two-fiber MEA at 10 mV/s in an aqueous solution containing 1 mM  $\text{FcCH}_2\text{OH}$  and 0.2 M KCl. The interelectrode distance,  $d$ , is  $\sim 6.5$   $\mu\text{m}$  in this case. Figure 3-3A and 3-3B display the voltammetric response of  $E_a$  and  $E_b$  when the other is open circuited, respectively. Figure 3-3C shows the steady-state voltammetric response when  $E_a$  and  $E_b$  are connected and voltammetry measured at both electrodes collectively.

For a disk-shape microelectrode embedded in an infinitely thick insulating material, the steady-state limiting current,  $i_d$ , is described using the following equation,<sup>57</sup>

$$i_d = 4nFDC^*a$$

Equation 3-1

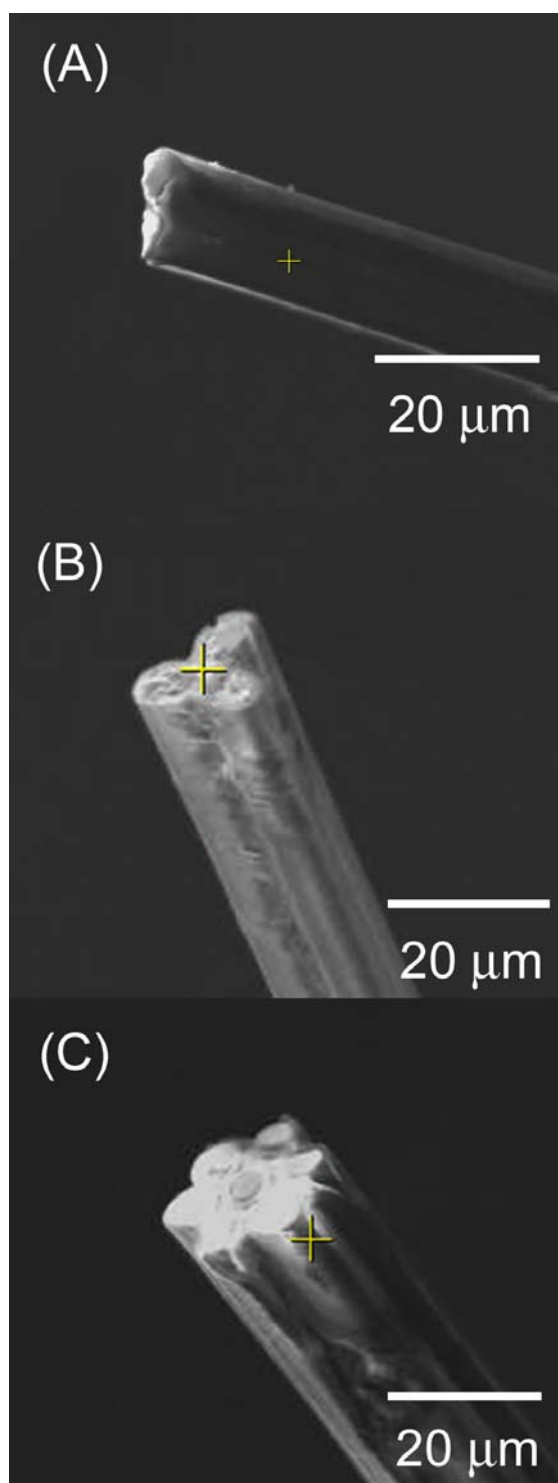


**Figure 3-2.** Scanning electron microscopy of carbon fiber MEAs having two (A), three (B), and seven (C) microdisks.

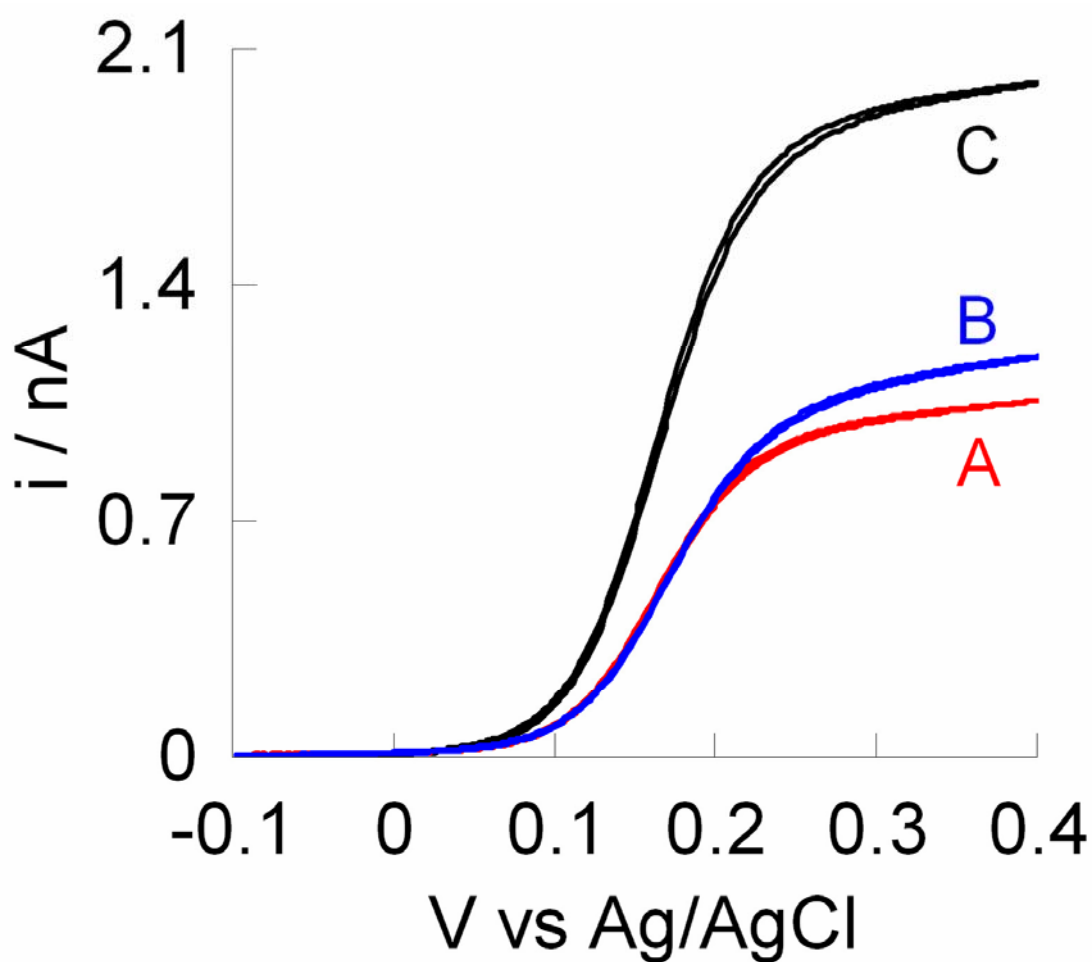


**Figure 3-3.** Steady-state voltammetric response of a two-fiber MEA in 1 mM  $\text{FcCH}_2\text{OH}$  containing 0.2 M KCl at a scan rate of 10 mV/s; (A) the response of microelectrode A alone, (B) the response of microelectrode B alone, and (C) the response of both microelectrodes operated and connected together.

where  $n$  is the number of electrons transferred per molecule,  $F$  is Faraday's constant,  $D$  is the diffusion coefficient, and  $C^*$  and  $a$  are the bulk concentration of the redox molecule and the radius of the microelectrode, respectively. In the case of carbon MEAs, the thickness of the insulating glass is small compared to the radii of the carbon microdisks. Thus, the measured steady-state limiting current is, in fact, larger than what is predicted using Equation 3-1. The predicted limiting current,  $i_d$ , using Equation 3-1, is 753 pA for a 2.5- $\mu\text{m}$ -radius disk microelectrode in 1 mM  $\text{FcCH}_2\text{OH}$  ( $D = 7.8 \times 10^{-6} \text{ cm}^2/\text{s}$ ).<sup>58</sup> The actual measured limiting currents are 1100 and 1020 pA for  $E_a$  and  $E_b$ , respectively, which are ~46% and ~35% larger than the predicted value. The difference in limiting current is apparently due to the underestimated diffusive flux of redox molecule from the bulk to the electrode. This concept has been simulated for small electrodes of varied insulation thickness.<sup>59</sup> In this perspective, the steady-state voltammetric response of a carbon microelectrode is better described by using the equation for a hemispherical microelectrode<sup>60</sup>

$$i_d = 2\pi n F D C^* a \quad \text{Equation 3-2}$$

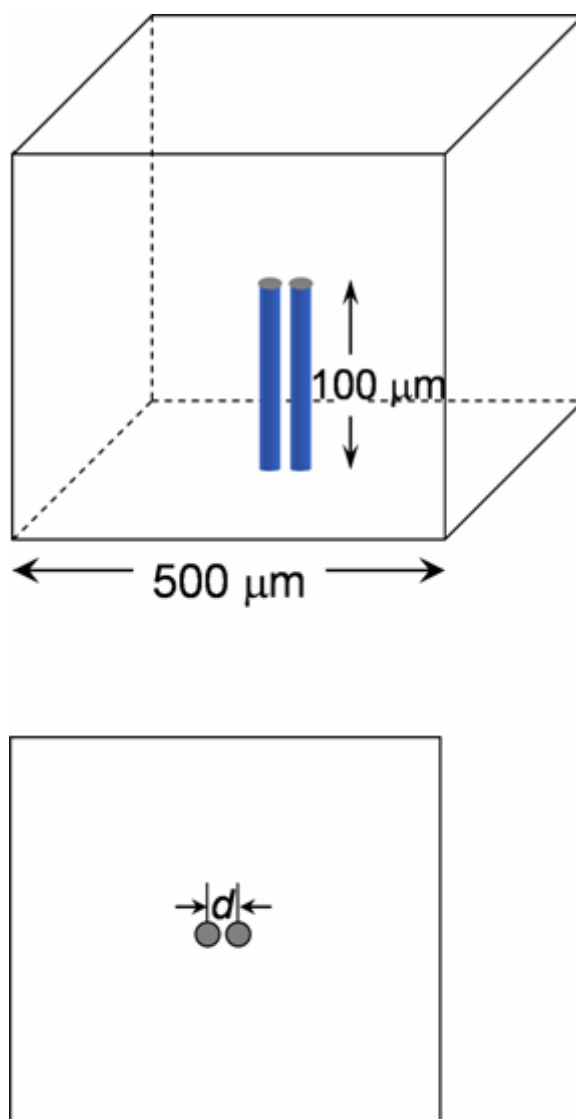
where the only difference is a larger constant,  $2\pi$ , as compared to 4 in Equation 3-1. The computed limiting current,  $i_d$ , is 1180 pA using Equation 3-2, in fair agreement with what is measured at each carbon microelectrode.

Figure 3-3C shows the overall steady-state voltammetric response of the two carbon fibers measured when they are connected. The limiting current in Figure 3-3C is in fact ~15% smaller than the sum of the limiting currents individually measured at the

two microelectrodes. Experiments and numerical simulations have shown that the voltammetric response of a 2D microdisk electrode array is largely affected by its interelectrode distances: when microdisks are well separated, they behave like individual electrodes; when they are close to each other, they behave like a macroelectrode.<sup>32, 51-54</sup> In the case presented here, there is clearly overlap of the depletion layers at the two electrodes.

The effect of  $d$  on the steady-state voltammetric response of a two-fiber MEA has been studied by Baur and Motsegood by the use of both steady-state electrochemical measurements and numerical simulations.<sup>61</sup> In the following section, I present a finite-element simulation of the distribution of diffusive flux at the electrodes to visualize the overlap of the diffusion layers.

**Finite-element simulation of the steady-state diffusive flux at a two-fiber MEA.** The numerical simulation of diffusive flux was accomplished in 3D space using a steady-state diffusion model (using Comsol software Ver. 3.2, Comsol Inc.).<sup>62</sup> In the simulation, the radii ( $a = 2.5 \mu\text{m}$ ) and the length ( $100 \mu\text{m}$ , 40x larger than  $a$ ) of the microdisk electrodes were held constant and the interelectrode distance was varied. A  $500 \mu\text{m}$  (200x larger than  $a$ ) cubic box was used as the electrochemical cell, in which the concentration of redox species at the surface of cubic box (1 mM) and at the electrode surface (0 mM) were held constant. For simplicity, the thickness of the insulation material surrounding and between the two microdisks was not considered, thus the calculated current is likely to be slightly larger than what is obtained experimentally. However, this should not affect the analysis of the “cross-talk” between the two microelectrodes significantly. A schematic drawing



**Figure 3-4.** The geometry of the electrochemical cell and the electrodes used in the numerical simulations.

of the electrochemical cell and the electrodes is given in Figure 3-4. The normalized steady state-current from the simulation is in good agreement with the experimental data (Figure 3-5). Both the simulation and the experiment show that when  $(d/a)$  is  $\sim 5$ , the electrodes behave independently.

The inter-electrode distance required for isolation of responses can be qualitatively understood by use of a computer simulated spatial distribution of steady-state flux of redox species. The simulated cross-sectional distribution of the steady-state flux of the redox molecules (1 mM  $\text{FcCH}_2\text{OH}$ ,  $V_{app} = 0.5 \text{ V}$  vs  $\text{Ag/AgCl}$ ) near the electrode surface is displayed in Figure 3-6. The overlap of the flux of redox molecules from bulk solution to the two microdisks can be easily visualized when  $d$  is small compared to the radius of the electrode (e.g.,  $d/a = 2.4$ ), as shown in Figure 3-6A. It is smaller (but still noticeable) when  $d/a$  is 4, as shown in Figure 3-6B. However, when  $d$  becomes even larger, as displayed in Figure 3-6C ( $d/a = 10$ ) and 3-6D ( $d/a = 20$ ), no significant overlap is observed in the simulated data. This is in agreement with the steady-state electrochemical responses of the two microelectrodes.

**Voltammetric response of a seven-fiber MEA.** Steady-state and fast-scan voltammetry has been used to characterize a seven-carbon-fiber MEA. An optical microscopy image shows that the electrode has a total tip dimension of  $\sim 20 \mu\text{m}$  which indicates that the interelectrode distance in the array is  $\sim 7 \mu\text{m}$ . As the diameter of each microdisk is  $5 \mu\text{m}$ , the thickness of the glass between adjacent fibers is  $\sim 2 \mu\text{m}$ . Figure 3-7 (parts A-G) shows the steady-state voltammetric response of each microelectrode (Figure 3-7H shows the relative position of each microelectrode in the array) measured simultaneously at  $20 \text{ mV/s}$  in 1 mM  $\text{FcCH}_2\text{OH}$  and 0.2 M KCl. The voltammetric response is well defined and

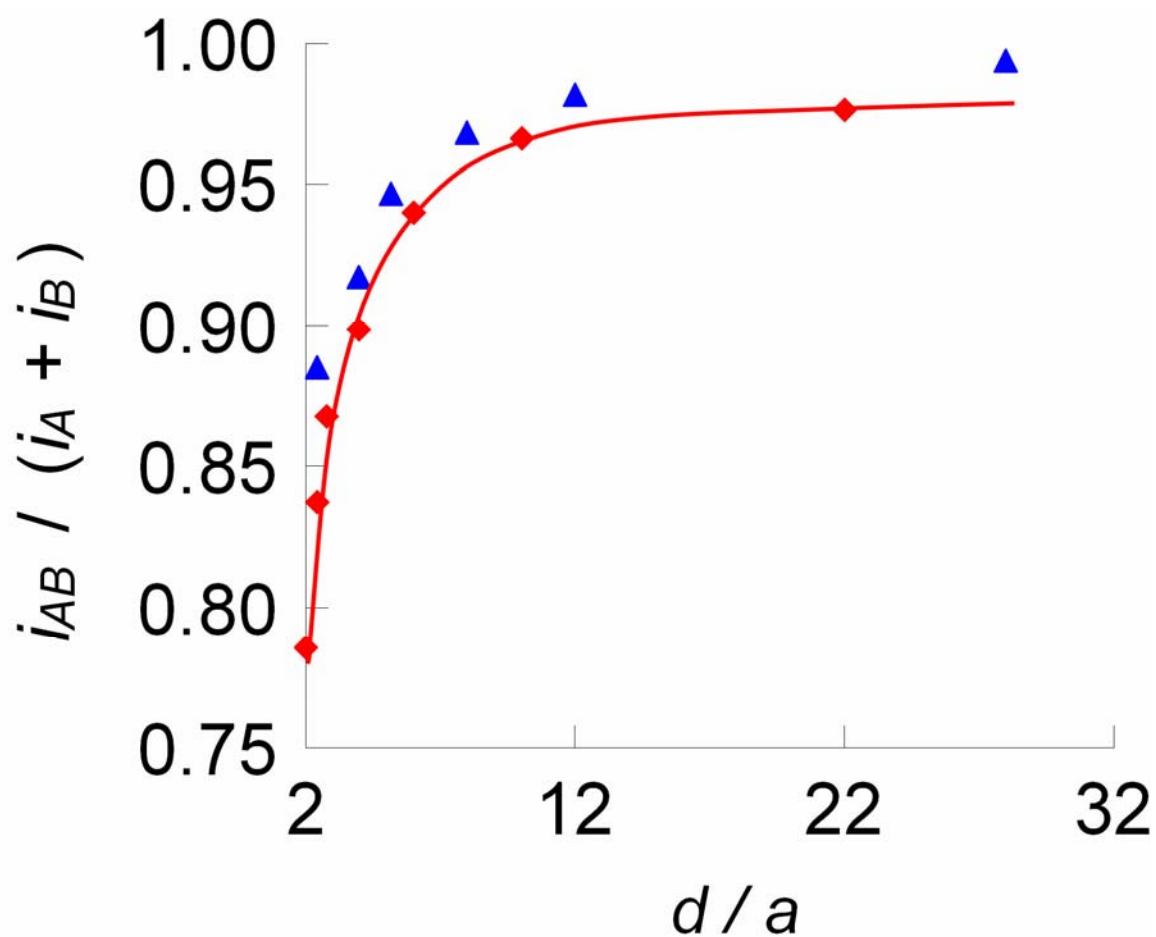


**Figure 3-5.** A comparison of the experimental and the simulated data of the normalized steady-state limiting current at a two-fiber MEA,  $i_{AB} / (i_A + i_B)$ , as a function of  $d/a$ , in 1 mM FcCH<sub>2</sub>OH and 0.2 M KCl.  $i_{AB}$ ,  $i_A$ , and  $i_B$  are the steady-state limiting currents when  $E_b$  and  $E_b$  are connected together, for  $E_a$  alone ( $E_b$  not connected), and for  $E_b$  alone ( $E_a$  not connected), respectively. The blue triangles are experimental data and the red diamonds are from numerical simulations. A line is drawn through the diamonds to fit the simulated data.



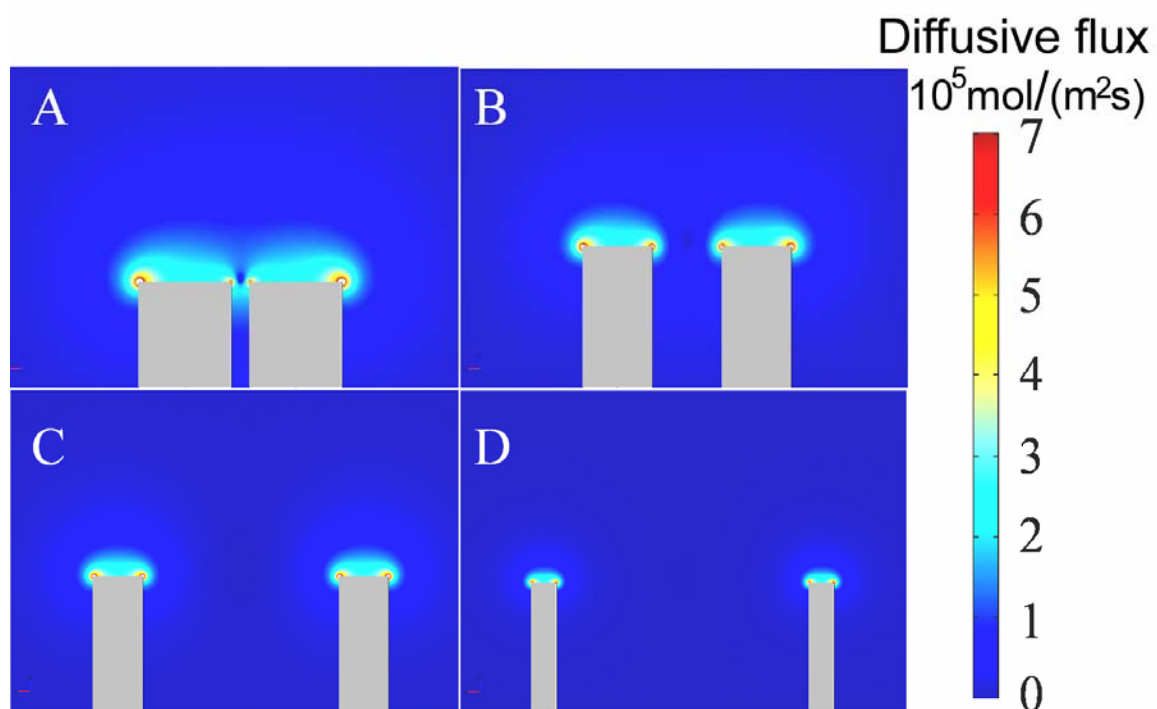


**Figure 3-6.** Simulated distribution of steady-state diffusive flux at the cross section of a 5-  $\mu\text{m}$  two-fiber MEA as a function of the interelectrode distance. The  $d/a$  are (A) 2.4, (B) 4, (C) 10, and (D) 20, respectively.

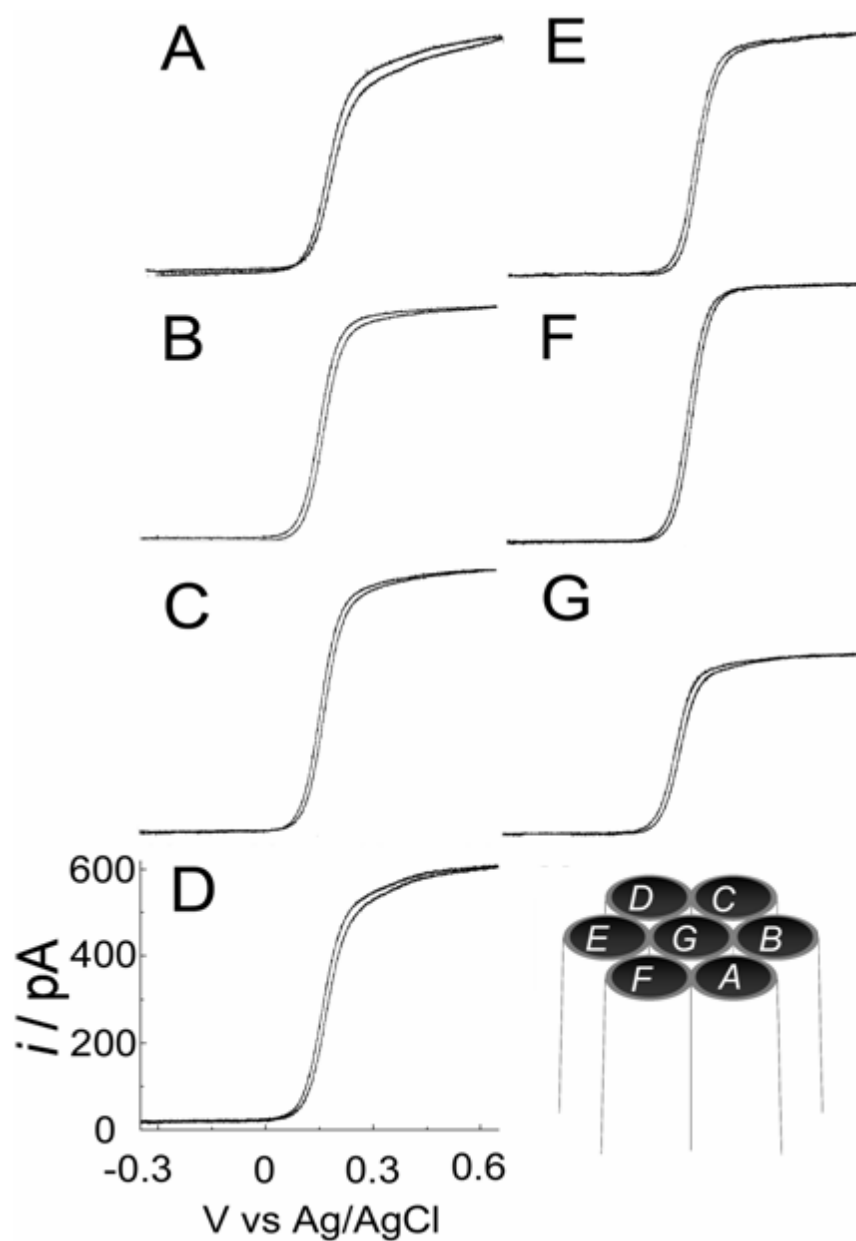


**Figure 3-7.** Steady-state voltammetric response at 20 mV/s of a seven-fiber MEA in 1 mM  $\text{FcCH}_2\text{OH}$  and 0.2 M KCl. (A) through (G) are the voltammetric responses of individual microelectrodes labeled A through G as shown in the schematic of the microelectrode assembly shown in the bottom right.

has a sigmoidal shape at this scan rate. The steady-state limiting current at each microelectrode is approximately the same, except for  $E_g$  (Figure 3-7G). Close inspection of the voltammogram in Figure 3-7G indicates that the diffusion limited steady-state current for the center electrode is ~40% smaller than that observed for the edge electrodes (A-F). The limiting current for the surrounding electrodes is ~610 pA, which is 48% smaller than what is predicted using Equation 3-2. This difference is apparently due to geometrically-hindered diffusion combined with depletion of the analyte by the surrounding electrodes. This is more evident for the center electrode as the limiting current at this electrode is somewhat shielded by the collection of microelectrodes surrounding it.

Figure 3-8 (parts A-G) shows the raw fast-scan voltammetric responses of each electrode in the same seven-fiber MEA at 300 V/s in the same solution. On top of the capacitive charging current are two voltammetric peaks corresponding to oxidation and reduction of  $\text{FcCH}_2\text{OH}$  and  $\text{FcCH}_2\text{OH}^+$ , respectively. The average double-layer charging current is ~3 nA, which corresponds to a double-layer capacitance of ~10 pF at each electrode (~51  $\mu\text{F}/\text{cm}^2$ ). The peak currents at electrodes  $E_a$  through  $E_g$  are approximately the same, ~3 nA. No significant difference is found in the fast-scan voltammetric response of  $E_g$  (e.g., Figure 3-8G) indicating that the depletion layer is small as the voltammetric response is due mainly to molecules adjacent to the electrode at this scan rate.<sup>63</sup> These results demonstrate that the microelectrodes are individually addressable and behave ideally in voltammetric measurements.

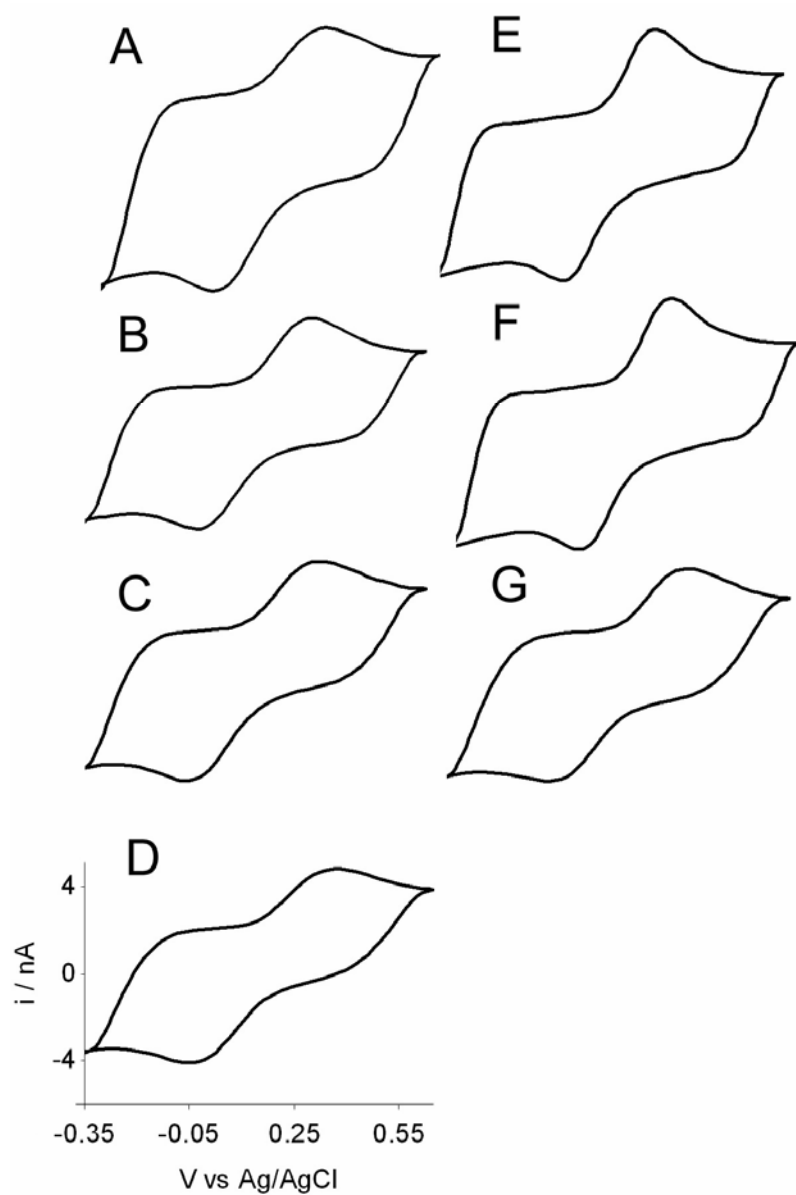


**Figure 3-8.** Fast-scan voltammetric response (300 V/s) of the same seven-fiber MEA in 1 mM  $\text{FcCH}_2\text{OH}$  and 0.2 M KCl. (A) through (G) are the voltammetric responses of individual microelectrodes A through G (as in Figure 3-7).

In single-cell type experiments, microdisk electrodes are placed close to cell membranes. In this case, released neurotransmitters are oxidized locally and free diffusion is minimized by the small electrode/cell separation.

**Amperometric detection of neurotransmitter release from single PC12 cells: an electrochemical array image.** Electrochemical recordings using carbon MEAs are expected to provide excellent temporal resolution, and allow simultaneous examination of different membrane areas with subcellular resolution. My coworkers and I have used this ability to compare biofunctionality in terms of exocytosis. Figure 3-9A shows an optical micrograph of a carbon MEA placed on a single PC12 cell. A glass micropipette containing high  $K^+$  solution (100 mM) was positioned  $\sim 100\ \mu\text{m}$  away to stimulate secretion. Figure 3-9B displays a 16-min amperometric recording of exocytotic events at a single PC12 cell. Each current transient corresponds to the electrochemical oxidation of dopamine molecules secreted from a single intracellular vesicle.

Noticeable in Figure 3-9B is subcellular heterogeneity observed in single-cell exocytosis. For example, the area of cell membrane under  $E_f$  shows fewer events than the others during the first 8 min and appears to be a “cold-spot”. More interestingly, spots may be “hot” during a specific period, but then change to be “cold” (or vice versa) after another stimulus. Close inspection of the response from  $E_a$  shows there are fewer events detected after the second and the fifth stimuli than after the third and fourth. In addition,  $E_f$  and  $E_g$  clearly detected more events in the last 8 min than in the first. Thus, it appears that the array electrode format allows detection of localized membrane function in terms of exocytosis at a single cell.

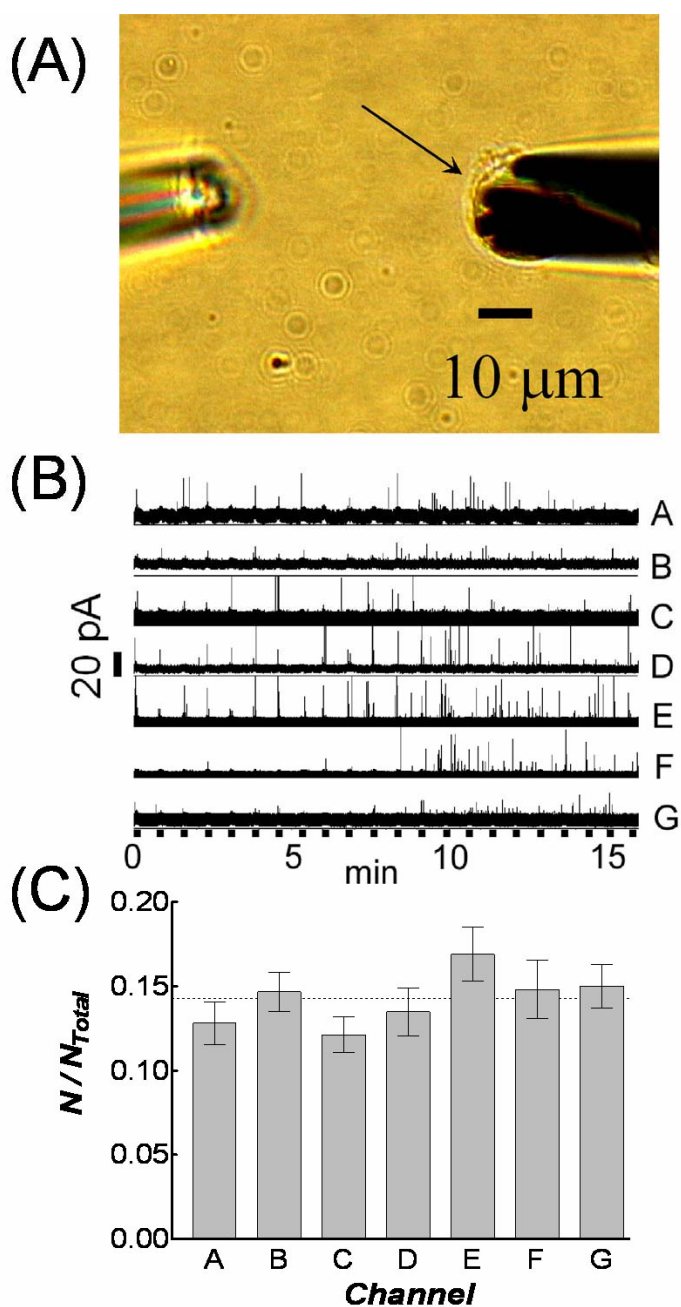


**Figure 3-9.** (A) An optical image showing a microelectrode-array positioned over a single PC12 cell (right) and a stimulation pipette (left). The cell is denoted with an arrow. (B) Amperometric traces of exocytotic release from a PC12 cell recorded using a microelectrode-array. Thick black lines along the time axis indicate exposure to high potassium stimuli (100 mM, 5-s pulse every 45 s). (C) The average value of normalized number of exocytotic events recorded with each electrode in the array. Eight different microelectrode arrays were used to examine 16 PC12 cells. Error bars are  $\pm$  S.E.M.

The detection probability on each channel was compared from sixteen different PC12 cells ( $n = 8$  electrode arrays) to ensure the differences detected with each channel do not arise from systematic errors, such as electrode placement or response. The number of events at each channel was normalized to the total number of events at a cell before averaging. Figure 3-9C displays a comparison of the averaged value of normalized number of events for each channel recorded from sixteen PC12 cells. From the averaged data, there are no significant differences among the channels ( $P$  value = 0.35, one-way ANOVA), indicating that differences seen in the number of detected exocytotic events at a given cell reflect the subcellular spatial heterogeneity in the exocytosis process.

**Resolving concurrent exocytotic events in single-cell amperometric detection using multi-fiber MEAs.** Another issue that can be examined with array electrodes is the incidence of concurrent events on the same cell. When more than one event occurs simultaneously it is challenging to resolve them using a single microelectrode. In the absence of spatial resolution, these events will overlap and result in a large, broad current spike. Simultaneous, parallel recordings using multiple microelectrodes allows these events to be resolved based on spatial identification. Figure 3-10 shows a one-second amperometric recording on a single PC12 cell using a seven-fiber MEA. The red arrows indicate three different exocytotic events detected from  $E_b$ ,  $E_c$ , and  $E_g$ , respectively. The events are extremely similar temporally such that when using one electrode, they would form a single large, broader current spike. Although rare, these overlapping events can be spatially resolved by the seven-fiber MEA. The multiple detection sites present allow the temporally synchronous release events present at different electrodes to be resolved.

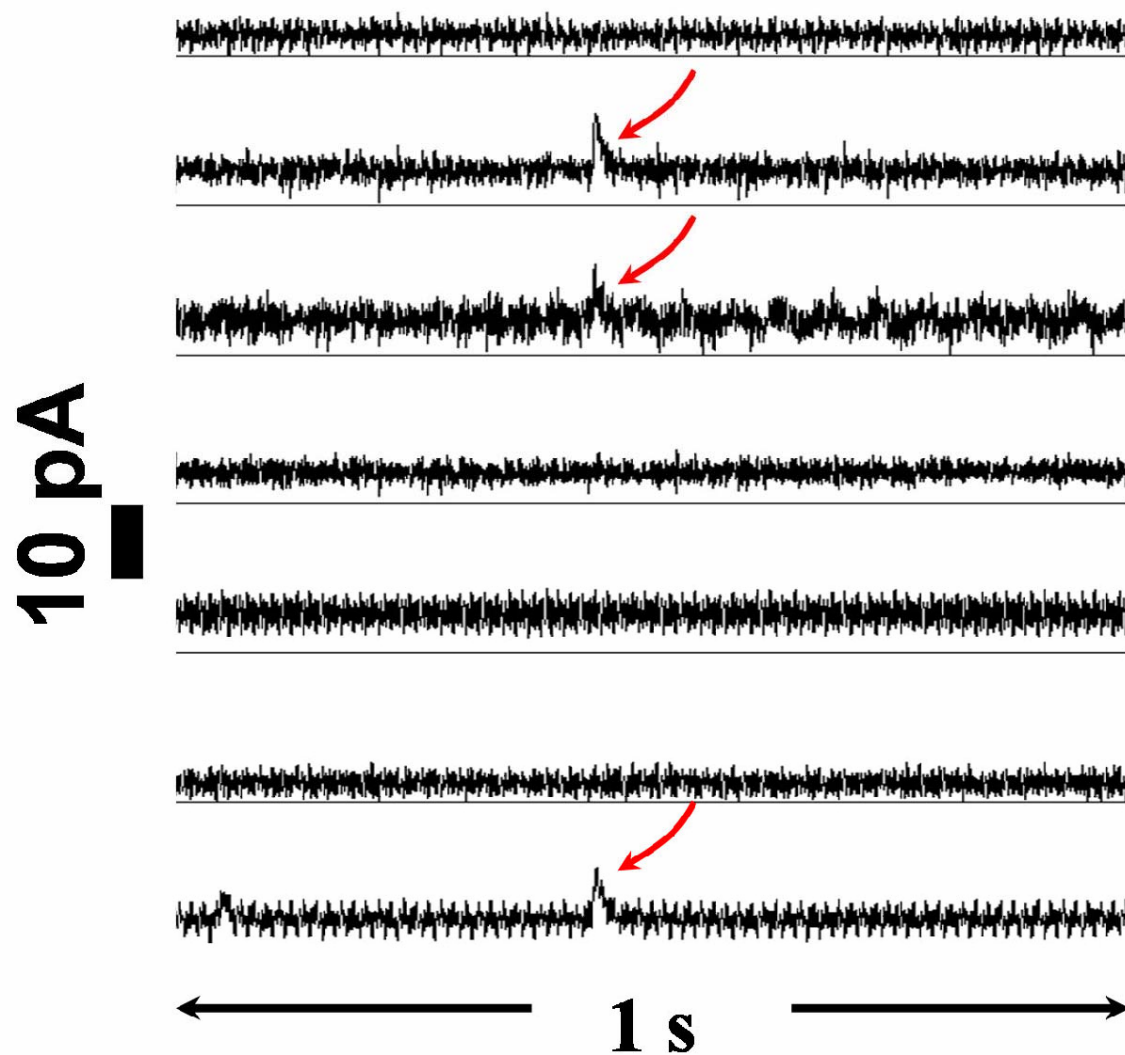


**Figure 3-10.** A one-second time period of an exocytotic response of a PC12 cell after potassium stimulation showing simultaneous detection of concurrent events at different locations on the same cell. Red arrows indicate these events.



## Conclusions

Carbon fiber MEAs have been fabricated and are applicable for spatially probing chemical changes in tight spaces, such as studying exocytosis from different regions of single cell surfaces. Electron microscopic characterization showed that these micro-sensor arrays were on the order of 20  $\mu\text{m}$  and were geometrically well defined. Finite element simulation was applied to qualitatively study the “cross-talk” in a two-fiber MEA. Steady-state and fast-scan voltammetric responses demonstrated that the MEAs have well defined electrochemical behavior and each microelectrode can be individually addressed. A seven-fiber MEA was used for simultaneous electrochemical monitoring of exocytotic events from different surface regions of single PC12 cells. Subcellular heterogeneity in exocytosis was shown with 5- $\mu\text{m}$  resolution. Concurrent exocytotic events under different microelectrodes were also temporally resolved using MEAs. These results show that carbon-fiber based microelectrode-arrays are suitable for electrochemical imaging of fast exocytotic events at single cells.

## References

- (1) Kandel, E. R.; Schwartz, J. H.; Jessell, T. M. *Principles of Neural Science*, 4th ed.; McGraw Hill, **2000**.
- (2) Weber, T.; Zemelman, B. V.; McNew, J. A.; Westermann, B.; Gmachl, M.; Parlati, F.; Sollner, T. H.; Rothman, J. E. *Cell* **1998**, 92, 759-772.
- (3) Chen, T. K.; Luo, G.; Ewing, A. G. *Anal Chem* **1994**, 66, 3031-3035.
- (4) Wightman, R. M.; Jankowski, J. A.; Kennedy, R. T.; Kawagoe, K. T.; Schroeder, T. J.; Leszczyszyn, D. J.; Near, J. A.; Diliberto, E. J., Jr.; Viveros, O. H. *Proc Natl Acad Sci U S A* **1991**, 88, 10754-10758.
- (5) Wightman, R. M. *Science* **2006**, 311, 1570-1574.
- (6) Mosharov, E. V.; Sulzer, D. *Nat Methods* **2005**, 2, 651-658.
- (7) Schroeder, T. J.; Jankowski, J. A.; Senyshyn, J.; Holz, R. W.; Wightman, R. M. *J Biol Chem* **1994**, 269, 17215-17220.
- (8) Stefan, R. I.; Staden, J. F. V.; Aboul-Ensin, H. Y. *Crit. Rev. Anal. Chem.* **1999**, 29.
- (9) Droge, M. H.; Gross, G. W.; Hightower, M. H.; Czisny, L. E. *J Neurosci* **1986**, 6, 1583-1592.
- (10) Wilson, M. In *Visualizing Large-Scale Pattern of Activity in the Brain: Optical and Electrical Signals*; Society of Neuroscience: Atlanta, GA, 2006, pp 9-16.
- (11) Arcibal, I. G.; Santillo, M. F.; Ewing, A. G. unpublished data.
- (12) Maher, M. P.; Pine, J.; Wright, J.; Tai, Y. C. *J Neurosci Methods* **1999**, 87, 45-56.
- (13) Suzuki, I.; Sugio, Y.; Jimbo, Y.; Yasuda, K. *Lab Chip* **2005**, 5, 241-247.
- (14) Stett, A.; Egert, U.; Guenther, E.; Hofmann, F.; Meyer, T.; Nisch, W.; Haemmerle, H. *Anal Bioanal Chem* **2003**, 377, 486-495.

- (15) Yeung, C. K.; Sommerhage, F.; Wrobel, G.; Offenhausser, A.; Chan, M.; Ingebrandt, S. *Anal Bioanal Chem* **2007**, *387*, 2673-2680.
- (16) Cammarata, V.; Talham, D. R.; Crooks, R. M.; Wrighton, M. S. *Journal of Physical Chemistry* **1990**, *94*, 2680-2684.
- (17) Licht, S.; Cammarata, V.; Wrighton, M. S. *Science* **1989**, *243*, 1176-1178.
- (18) Belmont-Hebert, C.; Tercier, M. L.; Buffle, J.; Fiaccabrino, G. C.; de Rooij, N. F.; Koudelka-Hep, M. *Analytical Chemistry* **1998**, *70*, 2949-2956.
- (19) Fan, Y.; Chen, X. T.; Trigg, A. D.; Tung, C. H.; Kong, J. M.; Gao, Z. Q. *Journal of the American Chemical Society* **2007**, *129*, 5437-5443.
- (20) Feeney, R.; Kounaves, S. P. *Analytical Chemistry* **2000**, *72*, 2222-2228.
- (21) Gavin, P. F.; Ewing, A. G. *Journal of the American Chemical Society* **1996**, *118*, 8932-8936.
- (22) Gavin, P. F.; Ewing, A. G. *Analytical Chemistry* **1997**, *69*, 3838-3845.
- (23) Niwa, O.; Xu, Y.; Halsall, H. B.; Heineman, W. R. *Analytical Chemistry* **1993**, *65*, 1559-1563.
- (24) Wang, J.; Chen, Q. *Analytical Chemistry* **1994**, *66*, 1007-1011.
- (25) Feeney, R.; Kounaves, S. P. *Electroanalysis* **2000**, *12*, 677-684.
- (26) Lanyon, Y. H.; Arrigan, D. W. M. *Sensors and Actuators B-Chemical* **2007**, *121*, 341-347.
- (27) Li, J.; Ng, H. T.; Cassell, A.; Fan, W.; Chen, H.; Ye, Q.; Koehne, J.; Han, J.; Meyyappan, M. *Nano Letters* **2003**, *3*, 597-602.
- (28) Li, X. H.; Zhou, Y. L.; Sutherland, T. C.; Baker, B.; Lee, J. S.; Kraatz, H. B. *Analytical Chemistry* **2005**, *77*, 5766-5769.

- (29) Nagale, M. P.; Fritsch, I. *Analytical Chemistry* **1998**, *70*, 2902-2907.
- (30) Nagale, M. P.; Fritsch, I. *Analytical Chemistry* **1998**, *70*, 2908-2913.
- (31) Nolan, M. A.; Kounaves, S. P. *Analytical Chemistry* **1999**, *71*, 3567-3573.
- (32) Sandison, M. E.; Anicet, N.; Glidle, A.; Cooper, J. M. *Analytical Chemistry* **2002**, *74*, 5717-5725.
- (33) Sandison, M. E.; Cooper, J. M. *Lab on a Chip* **2006**, *6*, 1020-1025.
- (34) Sreenivas, G.; Ang, S. S.; Fritsch, I.; Brown, W. D.; Gerhardt, G. A.; Woodward, D. J. *Analytical Chemistry* **1996**, *68*, 1858-1864.
- (35) Wang, K.; Fishman, H. A.; Dai, H. J.; Harris, J. S. *Nano Letters* **2006**, *6*, 2043-2048.
- (36) Zoski, C. G.; Simjee, N.; Guenat, O.; Koudelka-Hep, M. *Analytical Chemistry* **2004**, *76*, 62-72.
- (37) Zoski, C. G.; Yang, N. J.; He, P. X.; Berdondini, L.; Koudelka-Hep, M. *Analytical Chemistry* **2007**, *79*, 1474-1484.
- (38) Cepak, V. M.; Hulteen, J. C.; Che, G. L.; Jirage, K. B.; Lakshmi, B. B.; Fisher, E. R.; Martin, C. R.; Yoneyama, H. *Chemistry of Materials* **1997**, *9*, 1065-&.
- (39) Krishnamoorthy, K.; Zoski, C. G. *Analytical Chemistry* **2005**, *77*, 5068-5071.
- (40) Martin, C. R. *Science* **1994**, *266*, 1961-1966.
- (41) Menon, V. P.; Martin, C. R. *Analytical Chemistry* **1995**, *67*, 1920-1928.
- (42) Ugo, P.; Moretto, L. M.; Bellomi, S.; Menon, V. P.; Martin, C. R. *Analytical Chemistry* **1996**, *68*, 4160-4165.
- (43) Merritt, C. D.; Justus, B. L. *Chemistry of Materials* **2003**, *15*, 2520-2526.
- (44) Szunerits, S.; Walt, D. R. *Analytical Chemistry* **2002**, *74*, 1718-1723.

- (45) Baker, W. S.; Crooks, R. M. *Journal of Physical Chemistry B* **1998**, *102*, 10041-10046.
- (46) Crooks, R. M.; Ricco, A. J. *Accounts of Chemical Research* **1998**, *31*, 219-227.
- (47) He, H. X.; Li, Q. G.; Zhou, Z. Y.; Zhang, H.; Li, S. F. Y.; Liu, Z. F. *Langmuir* **2000**, *16*, 9683-9686.
- (48) Cheng, W. L.; Dong, S. J.; Wang, E. K. *Analytical Chemistry* **2002**, *74*, 3599-3604.
- (49) Dressman, S. F.; Peters, J. L.; Michael, A. C. *Journal of Neuroscience Methods* **2002**, *119*, 75-81.
- (50) Hafez, I.; Kisler, K.; Berberian, K.; Dernick, G.; Valero, V.; Yong, M. G.; Craighead, H. G.; Lindau, M. *Proceedings of the National Academy of Sciences of the United States of America* **2005**, *102*, 13879-13884.
- (51) Beriet, C.; Ferrigno, R.; Girault, H. H. *Journal of Electroanalytical Chemistry* **2000**, *486*, 56-64.
- (52) Lee, H. J.; Beriet, C.; Ferrigno, R.; Girault, H. H. *Journal of Electroanalytical Chemistry* **2001**, *502*, 138-145.
- (53) Morf, W. E. *Analytica Chimica Acta* **1997**, *341*, 121-127.
- (54) Morf, W. E.; de Rooij, N. F. *Sensors and Actuators B: Chemical* **1997**, *44*, 538-541.
- (55) Harper, C. A. E. *Handbook of Ceramics, Glasses, and Diamonds*; McGraw Hill: New York, **2001**.
- (56) Sombers, L. A.; Hanchar, H. J.; Colliver, T. L.; Wittenberg, N.; Cans, A.; Arbault, S.; Amatore, C.; Ewing, A. G. *Journal of Neuroscience* **2004**, *24*, 303-309.

- (57) Saito, Y. *Rev. Polarog. (Japan)* **1968**, 15, 177.
- (58) Miao, W. J.; Ding, Z. F.; Bard, A. J. *Journal of Physical Chemistry B* **2002**, 106, 1392-1398.
- (59) Shoup, D.; Szabo, A. *Journal of Electroanalytical Chemistry* **1984**, 160, 27-31.
- (60) Bard, A. J.; Faulkner, L. R. *Electrochemical Methods.*, 2nd ed.; John Wiley & Sons: New York, **2001**.
- (61) Baur, J. E.; Motsegood, P. N. *Journal of Electroanalytical Chemistry* **2004**, 572, 29-40.
- (62) Zhang, B.; Zhang, Y. H.; White, H. S. *Analytical Chemistry* **2004**, 76, 6229-6238.
- (63) The distance that the redox molecule diffuses,  $\delta = (2Dt_{\text{expt}})^{0.5}$ , at the time of the voltammetric experiment ( $t_{\text{expt}} = RT/\nu F$ ), is  $\sim 0.36 \mu\text{m}$ .

## Chapter 4

### **Estradiol inhibits depolarization-induced exocytosis in PC12 cells via N-type voltage-gated calcium channels**

#### **Introduction**

17- $\beta$ -estradiol (E2) is a neuromodulator known to affect calcium fluxes and intracellular signaling on a fast time scale through a membrane receptor.<sup>1-5</sup> However, the proposed mechanisms by which E2 influences intracellular calcium and subsequent exocytosis vary and are not well understood. Apparently an array of messenger systems is involved, including but not limited to the ERK1/2 MAP kinase,<sup>6</sup> protein kinase B/Akt, phosphoinositol 3-kinase, and p38 MAPK pathways<sup>7</sup>. Activation of one or more of these pathways is cell-type specific and can lead to either enhancement or inhibition of neuronal activity.<sup>7</sup> Understanding precisely how E2 affects exocytosis both at physiological and pharmacological levels could provide insight into related adaptive neuronal processes affected by E2 such as synaptic plasticity, neuroprotection, and synaptogenesis.<sup>7-11</sup>

PC12 cells have been used frequently as a model to study the presynaptic exocytosis machinery because they secrete dopamine from large dense-core vesicles, permitting detection of individual vesicle release events with carbon fiber amperometry.<sup>12</sup> They have been used as a model system to study both voltage-gated calcium channels (VGCCs) and intracellular calcium release mechanisms.<sup>13-15</sup> PC12 cells are also an appropriate model system to study the effects of estrogens. They express estrogen receptor  $\beta$  and lack estrogen receptor  $\alpha$  in an undifferentiated state<sup>16</sup> and also contain the membrane estrogen receptor GPR30 (unpublished observations). Others have shown that

high micromolar concentrations of E2 inhibit secretion,<sup>9</sup> but the effects of physiological levels (~10 nM) of E2 on secretion in PC12 cells have not been examined.

Here I report the effects of both physiological and higher pharmacological levels of E2 on exocytosis evoked by elevated extracellular  $K^+$ , a stimulus that activates VGCCs and increases cytosolic calcium. The concentration ranges of E2 used were selected based on previous reports (see references<sup>17-20</sup>). Additionally, the results suggest that E2 suppresses exocytosis with a bimodal dose-dependence. Both physiological nanomolar and pharmacological micromolar concentrations of E2 inhibit exocytosis while intermediate levels of 1  $\mu$ M and 5  $\mu$ M do not affect exocytosis. At the 10-nM E2 level, the inhibitory effect is shown to involve N-type VGCCs. Furthermore, two concentrations of E2 (10 nM and 50  $\mu$ M) were shown to provoke release events during the E2 application, but this was observed to occur only in a subpopulation of cells. Subdividing cells into those where E2 evoked release and those where E2 evoked no significant release allowed comparison of the effects of E2 on exocytosis without artifacts from loss of vesicles in the readily released pool.

## **Experimental Methods**

**Materials.** 17- $\beta$ -estradiol was purchased from Calbiochem. FURA-2 am was purchased from Invitrogen. All other reagents were purchased from Sigma.

**Solutions.** The experimental bathing solution was HEPES-buffered saline, containing (in mM) 150 NaCl, 5 KCl, 2 CaCl<sub>2</sub>, 1.2 MgCl<sub>2</sub>, 10 HEPES and 5 glucose (pH 7.4). The high  $K^+$  depolarizing solution had the same composition as the saline only with KCl raised to 100 mM and NaCl lowered to 55 mM to maintain osmotic balance. For treatments, drugs were dissolved into the HEPES-buffered saline with the addition of 0.1% ethanol to



dissolve E2 and  $\omega$ -conotoxin. This concentration of ethanol had no effect on exocytosis in control experiments (data not shown).

**Cell culture.** PC12 cells <sup>21</sup> were purchased from the American Type Culture Collection (www.atcc.org) and maintained in phenol red-free RPMI 1640 (Mediatech/VWR: West Chester, PA) supplemented with 10 % equine serum (Hyclone: Logan, UT), 5 % fetal bovine serum (Hyclone: Logan, UT), and 100 units/mL Penicillin/Streptomycin (Gibco-Invitrogen: Carlsbad, CA). Cells were grown in collagen IV coated flasks without nerve growth factor, incubated at 7 % CO<sub>2</sub> and 37 °C, and subcultured every 7-9 days or when confluency was reached. Experiments were performed on cells 4 to 7 days after subculturing.

**Carbon fiber amperometry.** Electrodes were prepared as described previously <sup>22</sup>. Briefly, 5  $\mu$ m carbon fibers were threaded into glass pipettes via aspiration and pulled using a commercial puller (P-97, Sutter Instruments, Novato, CA) to create a seal around the tip of the fiber. Electrode tips were cut to a uniform diameter of 8  $\mu$ m (larger than the fiber diameter because of the encasing glass) with a razor and dipped for 5 min in epoxy (Epotek-301, Billerica, MA) prior to heating for 24 to 72 h at 100°C. On the day of experiments, electrode tips were beveled at 45° to produce a smooth electroactive disk surface using a commercial micropipette beveler (Model BV-10, Sutter Instruments, Novato, CA). Beveled electrode tips were maneuvered to the surface of individual cells and lowered until the electrode surface made contact with the cell, indicated by a slight deformation of the cell surface. Detection of catecholamine release was performed by holding the potential of the electrode at +700 mV versus an Ag/AgCl reference electrode placed in the bathing solution. Electrodes were tested immediately before and after each

experiment in 100  $\mu$ M dopamine to ensure sensitivity was maintained. Results were discarded from experiments where electrode sensitivity was lost.

Cells were plated on 60 mm collagen IV coated dishes and tested at 37 °C using an Olympus IX-70 inverted microscope and heat stage (Linkam Scientific, London, UK). Micropipettes were pulled using a commercial puller, back-filled with test solutions (high  $K^+$  stimulation solution, isotonic saline, or E2) and cut to  $\sim 15$   $\mu$ m O.D. These pipettes were positioned  $\sim 100$   $\mu$ m from the experimental cell and solutions were ejected onto the cell (Picospritzer II, General Valve Corp). Three successive 5-s pulses of 100 mM  $K^+$  were applied at 40-s intervals. Next, the recording was suspended and the electrode was raised from the cell for 10 min to allow the cell to recover. This recovery period was intended to limit the effects of desensitization to the stimulus during the experiment. After the recovery period, the electrode was returned to the cell surface and a 45-s pulse of E2 (or other drugs) was applied. A 45-s pulse was chosen to adequately expose the cell to the desired E2 level as well as to eliminate any genomic-related effects brought about by prolonged exposure. The cell then received 3 more successive 5-s pulses of 100 mM  $K^+$  following a rapid ( $<30$  s) secretagogue pipette change. In situations where the objective was to eliminate the involvement of ion channels throughout the experiment, cells were either exposed to the appropriate drug mixed with the E2 solutions or the appropriate drug was added directly to the bathing solution throughout the duration of the experiment.

**Electrochemical data acquisition and analysis.** Amperometric data were recorded with an Axon 200B amplifier (Molecular Devices, Sunnyvale, CA). The output was digitized at 5 kHz and filtered at 2 kHz with an internal four-pole Bessel filter, and analyzed

without subsequent filtering. Peaks were counted and characterized with the MiniAnalysis software detection algorithm (Synaptosoft, Decatur, GA). Peaks were detected if both the amplitude of local maxima and the area under the curve exceeded a threshold of five times the root-mean-squared noise for a flat, 2-s recording acquired at the beginning of each experiment.<sup>23</sup> Peaks were visually inspected to confirm that electrical noise was not included and to include peaks manually that were not detected due to their proximity in the current trace. Overlapping events were discarded if the baseline for each peak could not be extrapolated using a built-in software algorithm. In cases where peaks appeared to rise above a broader background current, the detection algorithm assigned a baseline for the peak to the level of the background current. On average,  $176 \pm 13$  peaks ( $n = 129$  cells) were detected from three 5-s  $K^+$  stimulations prior to treatment.

Changes in depolarization-induced exocytosis following treatment was calculated as a treatment ratio according to

$$\text{Treatment Ratio} = \frac{\# \text{ events after treatment}}{\# \text{ events before treatment}} \quad \text{Equation 4-1}$$

with the number of events summed from a cell stimulated three times with 100 mM  $K^+$  for both the numerator and denominator. This ratio represents a percent change from baseline with each cell serving as its own control. To estimate changes in exocytosis over time in the absence of any treatment, a control ratio was calculated from a set of untreated cells with the same 10-min recovery interval between each stimulation set. Where inhibition is compared to control in the text, percent inhibition was calculated as

$$\text{Percent Inhibition (\%)} = 100 - \left( \frac{\text{Treatment ratio}}{\text{Control ratio}} \times 100 \right) \quad \text{Equation 4-2}$$

Because the number of evoked peaks per cell can vary from 20 to 400 events, cells are best represented by averaging ratios from each cell rather than pooling pre- and post-treatment peaks from all cells prior to averaging, and were thus analyzed in this manner.

<sup>23, 24</sup> Two-tailed t-tests were used to compare all treatment groups, and the Dunnett t-test was used to compare a range of E2 concentrations to control; *p*-values  $\leq 0.05$  were considered significant. All data are expressed as mean  $\pm$  SEM of *n* single cell experiments.

**Intracellular calcium imaging and analysis.** PC12 cells were subcultured on 60 mm collagen IV-coated dishes. After 4 to 7 days of subculturing, cells were loaded with 1  $\mu$ M FURA-2 in isotonic saline for 15 minutes at 37°C and 7% CO<sub>2</sub>. The FURA-supplemented solution was then removed and the cells were washed 3 times with fresh, warmed isotonic saline. The dish was then transferred to the microscope heat stage and maintained at 37°C. Experiments were conducted as outlined in the *Carbon fiber amperometry* section. Ratiometric fluorescence imaging data were collected and analyzed using Olympus Cell-R and its accompanying software (Olympus, Hamburg, Germany). Briefly, FURA-2 is a ratiometric dye utilized by exciting the probe molecule with two different excitation wavelengths (340 and 380 nm). The emission from both excitation wavelengths is collected separately at the same wavelength (510 nm) and a comparison of the emission intensities generated from the 340 nm and the 380 nm excitations can be made.

$$FURA \text{ Ratio} = \frac{(F \text{ intensity}_{340})}{(F \text{ intensity}_{380})} \quad \text{Equation 4-3}$$

Repetitive cycling of the 340/380 nm excitation with continuous monitoring at 510 was used to monitor changes in intracellular calcium of PC12 cells. When calcium binds to FURA-2 i.e. when calcium enters the cell upon depolarization with 100 mM K<sup>+</sup>, the wavelength at which the probe can be excited shifts from 380 nm to 340 nm. This would result in an increase in the FURA ratio because the intensity of the emission from the 340 nm excitation increases and the intensity of the emission from the 380 nm excitation decreases. Each data acquisition was background-subtracted using a cell-free region present in the field-of-view. FURA treatment ratios were calculated as

$$FURA \text{ Treatment Ratio} = \frac{\text{Average FURA Ratio (after)}}{\text{Average FURA Ratio (before)}} \quad \text{Equation 4-4}$$

where the average FURA ratio AFTER is equal to the average of the peak ratios for the 3 K<sup>+</sup> stimulations after the treatment period and the average FURA ratio BEFORE is equal to the average of the peak ratios for the 3 K<sup>+</sup> stimulations before the treatment.

## Results

**Estradiol inhibits depolarization-evoked exocytosis.** Three successive 5-s pulses of 100 mM K<sup>+</sup>, applied at 40-s intervals, evoked massive exocytosis. When cells were challenged 10 min later with E2 for 45 s prior to a second round of three successive stimulations, the number of K<sup>+</sup>-stimulated events either remained the same (Figure 4-1A) or decreased (Figure 4-1B). Some cells also showed release events during the E2 application (Figure 4-1C). This phenomenon is discussed in more detail below. To examine the change in exocytosis following treatment with E2, data from the three

stimulations prior to E2 (serving as same-cell control) were compared to those following E2 (treatment) and these data are shown as E2 dose response curves in Figure 4-2. The data shown with the solid line compares the number of events observed after treatment to the number of events observed before treatment (Equation 4-5)

$$\frac{\# \text{ events } AFTER}{\# \text{ events } BEFORE} \quad \text{Equation 4-5}$$

Comparing the change in exocytosis after E2 to that prior to treatment (Figure 4-2), it is observed that E2 inhibits the amount of  $K^+$ -stimulated exocytosis observed in a biphasic manner with a maximum inhibition of  $67 \pm 7 \%$  at  $100 \mu\text{M}$  ( $n = 11$ ), the highest concentration of E2 tested. Application of E2 at physiologically relevant levels ( $10 \text{ nM}$ ) also resulted in a  $46 \pm 11 \%$  inhibition as previously described, although intermediate doses ( $1 \mu\text{M}$  to  $5 \mu\text{M}$ ) were not effective. There was a trend towards inhibition at  $2.5 \text{ nM}$  ( $p = 0.07$ ,  $n = 14$ ) and  $100 \text{ nM}$  E2 ( $p = 0.06$ ,  $n = 12$ ) that did not reach statistical significance as defined by a  $p$  value  $\leq 0.05$ . Individual amperometric peaks did not vary in size (area under the peak) or shape (rise time, decay time, half-width, and rise slope) after exposure to E2 at any concentration, indicating that E2 did not have any direct effects on the exocytosis machinery.

The curve with the dashed lines in Figure 4-2 compares the number of events observed both during and after treatment to the number of events observed before treatment (Equation 4-6).

$$\frac{\# \text{ events } AFTER + \# \text{ events } TREATMENT}{\# \text{ events } BEFORE} \quad \text{Equation 4-6}$$

These data suggest that release during application of E2 might affect that observed during  $K^+$  stimulation after the treatment. Data for E2 concentrations where these two curves differ, i.e. at 10 nM and 50  $\mu$ M, have been sub-divided into two groups of cells: those with events during the treatment period (Group 1) and those without events (Group 2). An arbitrary threshold of less than five events per stimulation for a cell was set for a cell to be categorized as Group 2. Furthermore, only Group 2 cells were used to investigate E2 inhibitory effects as Group 1 cells may have significant depletion of the number of readily releasable vesicles available for the post- $K^+$  stimulations, thus reducing the amount released during the subsequent  $K^+$  stimulation.

A comparison of Group 1 versus Group 2 cells for 10 nM and 50  $\mu$ M E2 treatments is shown in Figure 4-3. The treatment ratio for both groups was also calculated using Equation 4-6. Group 1 cells did not show inhibition of exocytosis at 10 nM E2, but rather a  $25 \pm 4$  % increase in the number of events observed (n=13). Likewise, Group 1 cells show very little inhibition at 50  $\mu$ M E2 ( $11 \pm 4$  %, n = 7). However, Group 2 cells showed a  $46 \pm 11$  % inhibition at 10 nM E2 (n = 6, \*\*p<0.01) and a  $26 \pm 9$  % inhibition at 50  $\mu$ M E2 (n = 5, not significant).

**Estradiol modulates calcium influx initiated by depolarization with  $K^+$ .** To measure the effects of E2 on cellular calcium entry, three successive 5-s pulses of 100 mM  $K^+$  were used to evoke calcium entry as monitored by the ratiometric calcium-indicator FURA-2. In all cases, calcium entry was observed following  $K^+$  stimulation. When cells were challenged 10 min later with E2 for 45 s prior to a second round of three successive  $K^+$  stimulations, the level of the calcium entry decreased or showed no change relative to

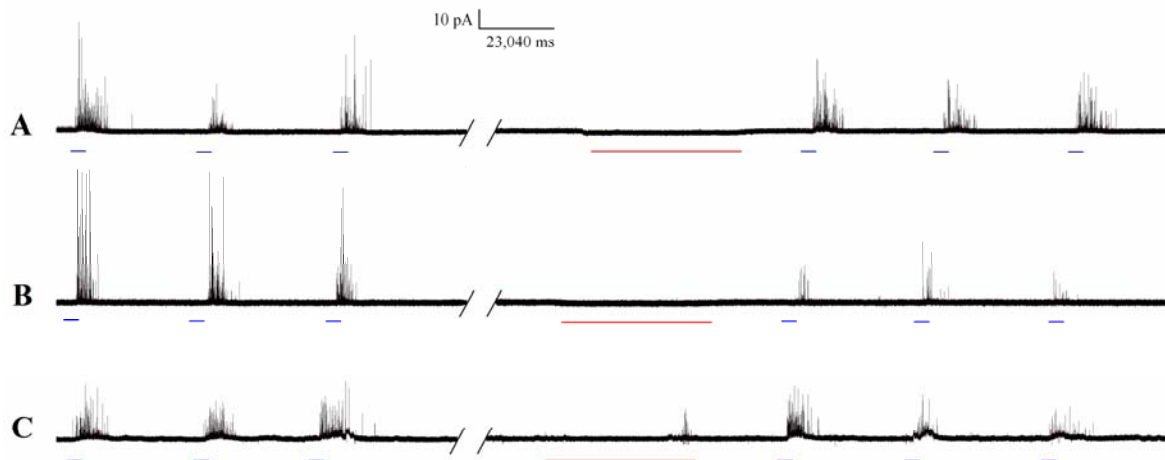


**Figure 4-1. Representative amperometric traces of exocytosis.** PC12 cells were stimulated three times for 5 s with 100 mM  $K^+$  (denoted by a blue line along the time axis of each current versus time amperometric trace below). The cells were then allowed to recover for 10 min (denoted as a break in the trace). Afterwards, the cells were exposed to a 45-s pulse of E2 of varied concentration (indicated by a red line along the time axis) and then followed with three more 5-s stimulations with 100 mM  $K^+$ . Cells generally responded in one of three ways: (A) Representative amperometric trace of a cell treated with 100 nM E2. The number of events after E2 exposure was approximately the same as the number of events seen before E2 exposure. No events were observed during the application of E2. (B) Representative amperometric trace of another cell treated with 100 nM E2. The number of events after E2 exposure dramatically decreased as compared to the number of events before E2 exposure. Again no events were seen during the application of E2. (C) Representative amperometric trace of another cell treated with 100 pM E2. The number of events after treatment was slightly reduced after E2 exposure as compared to the number of events before E2 exposure. However, events were also observed during the E2 application. Cells with events during the E2 treatment (C) are referred to as “Group 1” cells in the text. Cells without events during the E2 treatment (A and B) are collectively referred to as “Group 2” cells.



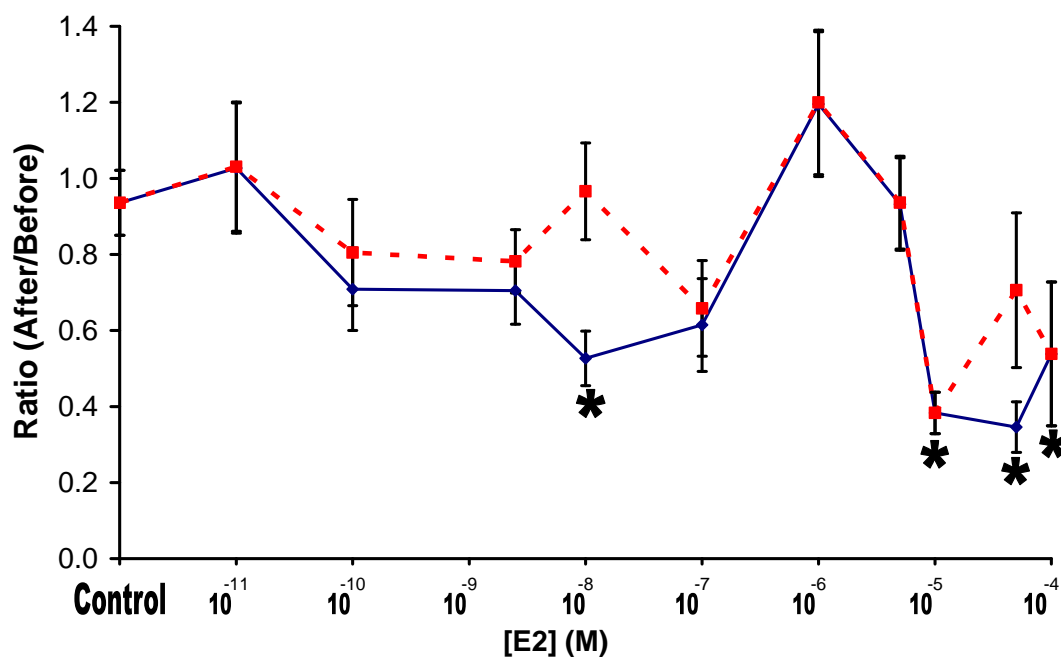


**Figure 4-2. Dose response curves for the effect of E2 on exocytosis.** The ratio of the number of events after E2 treatment is compared to the number of events before E2 treatment as a function of the concentration of the E2 treatment. The solid line shows the data from all cells investigated. Exocytosis events that occurred during the E2 treatment were excluded from this curve. The dashed line shows the data from all cells investigated but in this analysis, the number of exocytosis events during the E2 treatment have been added to those during the follow up  $K^+$  stimulations thus excluding bias that might occur from loss of releasable vesicles. At a physiological E2 concentration (10 nM), E2 appears to inhibit exocytosis (solid line). This inhibition is not observed, however, when events during E2 treatment period are included in the ratio calculation (dashed line). Likewise at pharmacological E2 concentrations (~10  $\mu$ M – 100  $\mu$ M), E2 appears to inhibit exocytosis. Only at 50  $\mu$ M does this calculated ratio change even when the events during E2 treatment are included in the analysis. Averages at each concentration are compiled from  $n = 16$  (control), 11 (10 pM), 9 (100 pM), 14 (2.5 nM), 19 (10 nM), 12 (100nM), 12 (1  $\mu$ M), 6 (5  $\mu$ M), 8 (10  $\mu$ M), 12 (50  $\mu$ M), and 11 (100  $\mu$ M) single cell experiments. \*  $p < 0.05$  versus control.

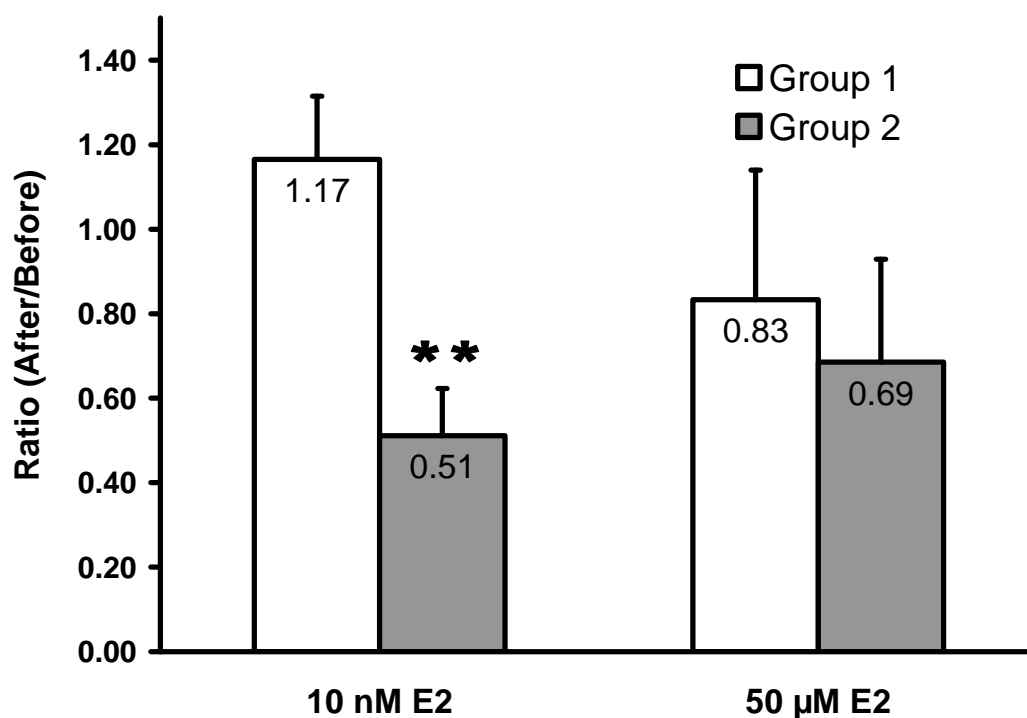
control (Figure 4-4). To examine the change in calcium entry following E2 treatment (Figure 4-5), the ratiometric fluorescence of FURA-2 with excitation at 340 and 380 nm was monitored (as described in the *Methods* section). Calcium entry following 10 nM E2 decreased by  $26 \pm 2\%$  ( $n=40$  cells from 4 separate dishes,  $**p<0.01$ ); however, 50  $\mu$ M E2 only decreased calcium entry by  $7 \pm 1\%$  ( $n=40$  cells from 4 separate dishes), a value not statistically different from isotonic saline control ( $p=0.44$ ).

### **Estradiol inhibition of exocytosis depends on N-type voltage-gated calcium channels.**

Exocytosis initiated by depolarization with  $K^+$  depends primarily on L- and N-type VGCCs in PC12 cells.<sup>14</sup> I used the specific N-type VGCC antagonist,  $\omega$ -conotoxin GVIA,<sup>25</sup> to test whether the action of E2 on N-type VGCCs was sufficient to account for its inhibition of exocytosis. To eliminate bias owing to stimulated release caused by E2, only cells categorized as Group 2 (no significant release caused directly by E2) were examined. When 500 nM  $\omega$ -conotoxin was present throughout the experiment, neither 10 nM nor 50  $\mu$ M E2 inhibited exocytosis. The number of post-E2 exocytosis events was  $102 \pm 11\%$  of the pre-E2 events at 10 nM ( $n = 12$ ) and  $104 \pm 16\%$  at 50  $\mu$ M ( $n = 7$ ) compared to untreated cells that decreased to  $94 \pm 8\%$  of initial activity over the same time interval (Figure 4-6). The results suggest that N-type VGCCs are required for the inhibitory effects of E2 at 10 nM, although other VGCCs and additional downstream targets could also be involved.

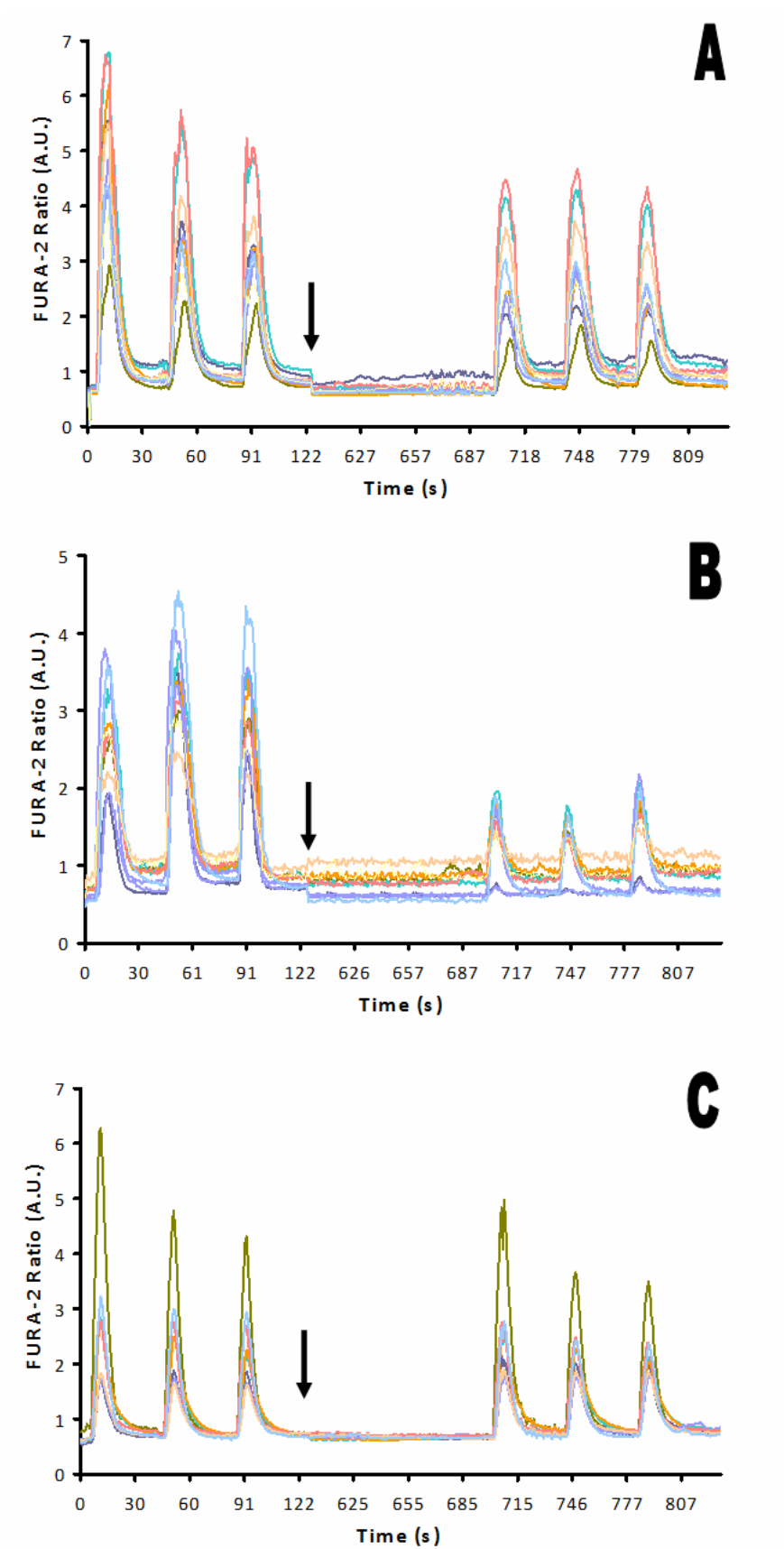
### **Discussion**

Brief application of E2 at near-physiological (10 nM) or higher pharmacological (10 or 100  $\mu$ M) concentrations significantly reduced the number of exocytosis events in



**Figure 4-3. Comparison of the effects of E2 on exocytosis for selected cell types.** The number of events observed during  $K^+$  stimulation after E2 treatment compared to the number of events before E2 treatment for cells treated with 10 nM and 50 µM E2. Group 1 contains cells having events (5 or more) during the E2 treatment period. Group 2 contains cells having few or no events (less than 5) during the E2 treatment period. To calculate the ratio for Group 1, events during the E2 application were added to the number of events seen after E2 treatment and this total was compared to the number of events seen prior to E2 treatment. At 10 nM, E2 inhibited release by 46 % for the Group 2 cells (\*\*  $p < 0.01$  compared to control). There was a trend toward inhibition at 50 µM E2 for the Group 2 cells ( $p=0.22$ ) that might become statistically significant with an increased  $n$  for this group.  $n=13, 6, 7$ , and  $5$  for 10 nM Group 1, 10 nM Group 2, 50 µM E2 Group 1, and 50 µM E2 Group 2, respectively.

**Figure 4-4. Potassium-evoked intracellular calcium levels are affected by E2 application.** Representative FURA-2 intracellular calcium traces for three separate dishes of cells treated with either isotonic saline control (A), 10 nM E2 (B), or 50  $\mu$ M E2 (C) are shown. The protocol replicates that implemented for electrochemistry experiments, with three 5-s 100 mM  $K^+$  stimulations applied every 40 s prior followed by a 10-min break in the collection to allow the cells to recover (indicated by a black arrow). The cells were then treated for 45 s with the appropriate concentration of E2 or isotonic saline as a control. The ratio of the intensities collected at emission 510 nm for excitation 340 nm and excitation 380 nm were calculated over time. An increase in the FURA-2 ratio indicates an increase in intracellular calcium, an activity known to precede the exocytosis process. A ratio of calcium entry during stimulations after treatment to that before treatment was calculated from the fluorescence data by comparing the average FURA-2 ratios for the 3  $K^+$  stimulations after treatment with the average FURA-2 ratios for the 3  $K^+$  stimulations before treatment.



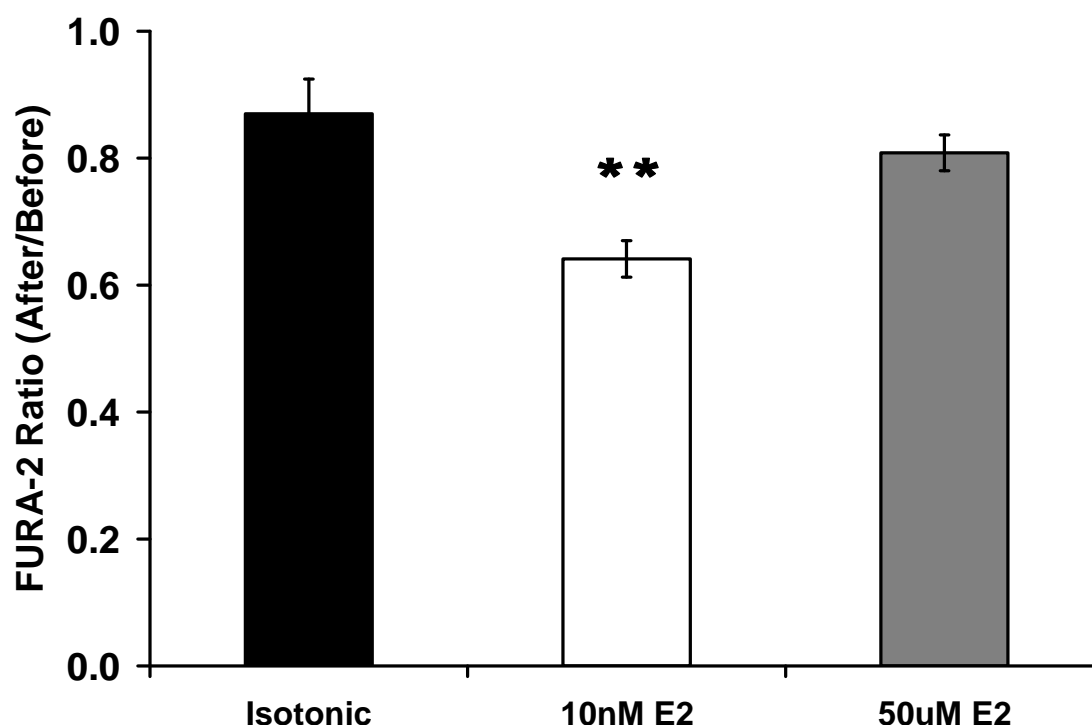


**Figure 4-5. Calcium entry during cell stimulation is reduced by low levels of E2.** When isotonic saline was administered during the drug treatment segment of the protocol as a control, the intracellular calcium levels slightly decreased compared to levels observed prior to the treatment period ( $87 \pm 5$  % of the number of events before) and this was used as the control value. Treatment with 10 nM E2 resulted in  $26 \pm 2$  % less calcium entry versus the isotonic control, a decrease statistically different from the control (\*\*  $p < 0.01$ ). Treatment with 50  $\mu$ M E2 resulted in a slight ( $7 \pm 1$ %), but not statistically different ( $p = 0.44$ ) decrease in the amount of calcium entry post-treatment.  $n = 80, 40$ , and  $40$  cells from  $7, 4$ , and  $4$  dishes for isotonic saline control, 10 nM E2, and 50  $\mu$ M E2, respectively.

PC12 cells, a model neuroendocrine cell. The reduction of exocytosis by E2 was abolished in the presence of the N-type VGCC antagonist,  $\omega$ -conotoxin GVIA. Furthermore, E2 at 10 nM and 50  $\mu$ M, in some cells, elicits exocytotic release (as determined by amperometry experiments), thus requiring cells challenged at these concentrations to be divided into two groups: one with events (Group 1) and one without events (Group 2) during the E2 application. Lastly, the magnitude of calcium influx following 10 nM E2 application was significantly reduced while calcium entry following 50  $\mu$ M E2 application remained nearly constant.

A vast body of work confirms that E2 can rapidly modulate calcium and intracellular messenger systems in the picomolar to nanomolar range.<sup>1-3, 26-28</sup> Depending on cell type and concentration, E2 can activate PKC, PKA, or ERK1/2 MAP kinase on a time scale similar to effects described here.<sup>7</sup> Moreover, these pathway activation(s) have been shown to either enhance or inhibit neuronal activity, a similar effect to that observed in the model system presented in this chapter at both 10 nM and 50  $\mu$ M E2 with events being provoked in some cases (i.e. Group 1 cells) during treatment period, or absent and subsequently reduced post-treatment (i.e. Group 2 cells). Levels of E2 in the micromolar range have also been reported to affect exocytosis.<sup>1, 2, 9</sup> However, a biphasic dose response to E2 that encompasses both response ranges has not previously been recorded. Within the concentration range tested here (10 pM-100  $\mu$ M), both the nanomolar and micromolar actions of E2 in PC12 cells on a short time scale might involve the same pathway, though the involvement of multiple and/or differing pathways cannot be ruled out.

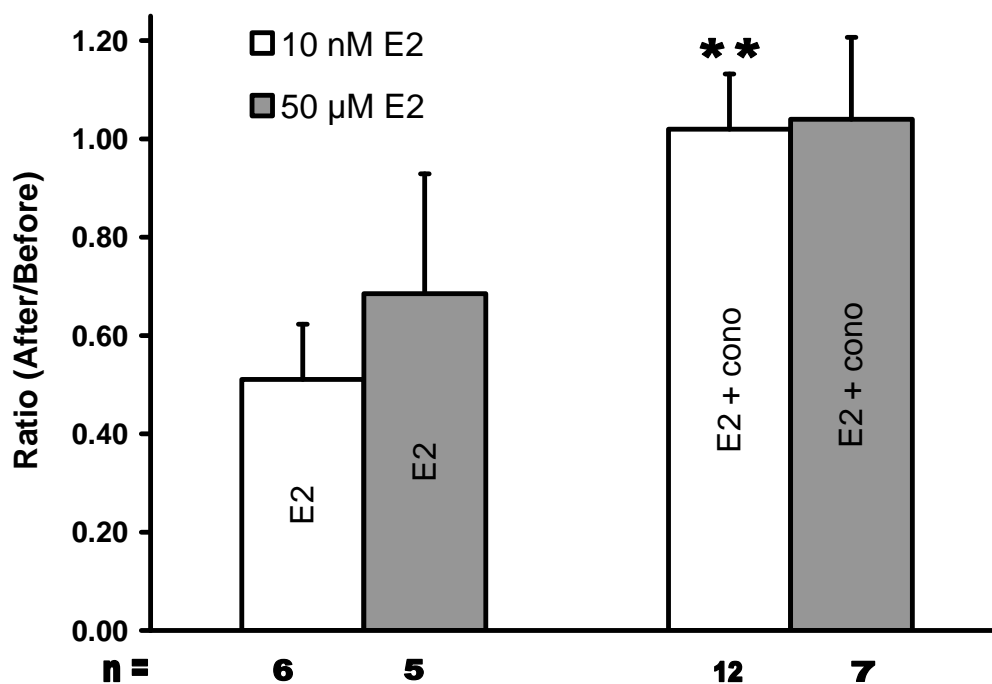


**Figure 4-6. E2-induced inhibition of exocytosis depends on N-type VGCCs in PC12 cells.** Addition of 500 nM  $\omega$ -conotoxin eliminated the decrease in exocytosis observed following 10 nM E2 (\*\*  $p < 0.01$ ) and 50  $\mu$ M E2, albeit the result is not statistically different for the 50  $\mu$ M E2 case. Treatment groups were comprised of Group 2 cells only (no E2-stimulated events during the treatment period).



It is interesting to speculate that the difference between Group 1 and Group 2 cells might involve differential expression of an estrogen receptor that facilitates stimulated exocytosis. This release might involve initial opening, rather than restricting of calcium channels on plasma membrane. The added stimulated release might deplete the vesicle pool available for further release and thereby reduce the number of exocytosis events observed with subsequent  $K^+$  stimulations. As expected then, the reduction in the number of events is smaller for Group 1 cells where the E2 stimulated release occurs. It is also interesting to speculate that the low and high E2 concentrations operate on the cell to alter exocytosis via different mechanisms. The change in the  $K^+$ -stimulated intracellular calcium increase after 10 nM E2 is significantly different from that for control, whereas following 50  $\mu$ M E2 it is not significantly affected. This suggests that low (physiological) levels of E2 affect VGCC's and that the higher potentially pharmacological levels might directly affect overall cell function. This could be important in understanding the neuroprotective mechanism of estrogen.

In summary, the data presented in this chapter suggest that, at least at low levels, E2 can act on N-type VGCCs to affect secretion of neurotransmitters, providing another potential mechanism for the modulation of neuronal communication and plasticity *in vivo*.

## References

- (1) Lee, D. Y.; Chai, Y. G.; Lee, E. B.; Kim, K. W.; Nah, S. Y.; Oh, T. H.; Rhim, H. *Life Sci* **2002**, *70*, 2047-2059.
- (2) Machado, J. D.; Alonso, C.; Morales, A.; Gomez, J. F.; Borges, R. *J Pharmacol Exp Ther* **2002**, *301*, 631-637.
- (3) Mermelstein, P. G.; Becker, J. B.; Surmeier, D. J. *J Neurosci* **1996**, *16*, 595-604.
- (4) Morales, A.; Diaz, M.; Ropero, A. B.; Nadal, A.; Alonso, R. *Eur J Neurosci* **2003**, *18*, 2505-2514.
- (5) Ronnekleiv, O. K.; Kelly, M. J. *Front Neuroendocrinol* **2005**, *26*, 65-84.
- (6) Thomas, W.; Coen, N.; Faherty, S.; Flatharta, C. O.; Harvey, B. J. *Steroids* **2006**, *71*, 256-265.
- (7) Kelly, M. J.; Levin, E. R. *Trends Endocrinol Metab* **2001**, *12*, 152-156.
- (8) Green, P. S.; Simpkins, J. W. *Int J Dev Neurosci* **2000**, *18*, 347-358.
- (9) Kim, Y. J.; Hur, E. M.; Park, T. J.; Kim, K. T. *J Neurochem* **2000**, *74*, 2490-2496.
- (10) McEwen, B. S. *J Appl Physiol* **2001**, *91*, 2785-2801.
- (11) Toran-Allerand, C. D.; Singh, M.; Setalo, G., Jr. *Front Neuroendocrinol* **1999**, *20*, 97-121.
- (12) Chen, T. K.; Luo, G.; Ewing, A. G. *Anal Chem* **1994**, *66*, 3031-3035.
- (13) Bennett, D. L.; Bootman, M. D.; Berridge, M. J.; Cheek, T. R. *Biochem J* **1998**, *329* ( Pt 2), 349-357.
- (14) Taylor, S. C.; Peers, C. *J Neurochem* **1999**, *73*, 874-880.
- (15) Tully, K.; Treistman, S. N. *J Neurophysiol* **2004**, *92*, 135-143.
- (16) Nilsen, J.; Mor, G.; Naftolin, F. *Menopause* **1998**, *5*, 211-216.

- (17) Cario-Toumaniantz, C.; Loirand, G.; Ferrier, L.; Pacaud, P. *J Physiol* **1998**, 508 (Pt 3), 659-666.
- (18) Kitazawa, T.; Hamada, E.; Kitazawa, K.; Gaznabi, A. K. *J Physiol* **1997**, 499 ( Pt 2), 497-511.
- (19) Yamamoto, T. *Am J Physiol* **1995**, 268, C64-69.
- (20) Zhang, F.; Ram, J. L.; Standley, P. R.; Sowers, J. R. *Am J Physiol* **1994**, 266, C975-980.
- (21) Greene, L. A.; Tischler, A. S. *Proc Natl Acad Sci U S A* **1976**, 73, 2424-2428.
- (22) Kozminski, K. D.; Gutman, D. A.; Davila, V.; Sulzer, D.; Ewing, A. G. *Analytical Chemistry* **1998**, 70, 3123-3130.
- (23) Colliver, T. L.; Hess, E. J.; Pothos, E. N.; Sulzer, D.; Ewing, A. G. *J Neurochem* **2000**, 74, 1086-1097.
- (24) Westerink, R. H.; de Groot, A.; Vijverberg, H. P. *Biochem Biophys Res Commun* **2000**, 270, 625-630.
- (25) Hirning, L. D.; Fox, A. P.; McCleskey, E. W.; Olivera, B. M.; Thayer, S. A.; Miller, R. J.; Tsien, R. W. *Science* **1988**, 239, 57-61.
- (26) Beyer, C.; Raab, H. *Eur J Neurosci* **1998**, 10, 255-262.
- (27) Vasudevan, N.; Pfaff, D. W. *Endocr Rev* **2007**, 28, 1-19.
- (28) Watson, C. S.; Campbell, C. H.; Gametchu, B. *Exp Physiol* **1999**, 84, 1013-1022.

## Chapter 5

### Steady-state electrochemical determination of lipidic nanotube diameter utilizing an artificial cell model

#### Introduction

Membrane tethers have sparked great interest concerning their potential role in fundamental cellular operations as well as their function within biological mimics. Lipid tubes help facilitate both intra- and intercellular transport of surface proteins, vesicles, and other small membranous entities. More specifically, membranous tubes facilitate trafficking between organelles within the same cell, such as within the Golgi-ER complex<sup>1, 2</sup>, but also between cells *in vitro*, for example, between specific cells contained in the immune system<sup>3</sup>, or even different cell types entirely.<sup>4</sup> Aside from lipid nanotubes found in cells performing “active” shuttling of materials, artificial lipid nanotubes have been implemented as connective channels in miniaturized nanotube-vesicle networks analogous to microfluidic systems.<sup>5, 6</sup> These systems are constructed from soybean liposomes and have been used to study small-scale enzymatic reactions with mass transport-based mixing.<sup>7</sup> For a more comprehensive review of applications employing liposomes, the reader can consult Reference 8.

Another variation of the nanotube-vesicle system has been developed into a suitable model to explore the role lipids play in the final stages of exocytosis, a process central to neuronal communication.<sup>9, 10</sup> The artificial cell model has a large, outer parent vesicle acting as a cell membrane and a small, inner vesicle connected by a lipid nanotube. This nanotube can be compared to the fusion pore created between the cell plasma membrane and the membrane of a synaptic vesicle. The synaptic vesicle diffuses

to the plasma membrane surface, docks, and fuses, forming a fusion pore. Subsequently the pore dilates and the vesicle content is released into the extracellular space. If electroactive molecules are in the vesicle, their release can be detected electrochemically by a microelectrode positioned over the cell. My coworkers and I were highly motivated to further characterize this tube dimension within the model system. Knowledge of the tube diameter provides a better understanding of the physical nature of the membrane structure and would lead to quantitative estimations of the magnitude and types of forces necessary to expel material through such an opening. For example, an osmotic pressure differential has been shown to increase the likelihood of “feet” in PC12 cells undergoing exocytosis.<sup>11</sup> These feet, manifested by small increases in current prior to the current transient associated with full release, represent small leakages of transmitter molecules from the vesicle through the initial fusion pore opening. This pre-release or a “foot” is detected electrochemically by the microelectrode positioned over the cell. Such leakage may be partially regulated by the physical dimensions of the pore opening thus making it an important parameter to measure.

Lipid nanotubes created from soy polar lipid extract have previously been estimated as having diameters in the 100- to 300-nanometer range. These estimates were based on two methods: a video pixel analysis<sup>5</sup> and a tube coalescence method<sup>12</sup> previously described by Cuvelier and coworkers.<sup>13</sup> Other methods such as transmission electron microscopy<sup>14</sup>, freeze fracture electron microscopy<sup>14, 15</sup>, scanning electron microscopy<sup>16</sup>, atomic force microscopy<sup>17</sup>, and lipid tether pulling experiments<sup>18-20</sup> have been employed to characterize membranous tubes. Most of these methods require a stable, non-fluidic sample in order to successfully carry out analysis. It is difficult to

obtain a viable, fluidic sample to measure the tube dimensions in its dynamic, more biologically relevant state.

Electrochemical methods are ideally suited for measurements in aqueous environments. More specifically, steady-state amperometry is appropriate for measuring the net flux of electroactive material through a defined geometry. Previously steady-state electrochemistry was utilized to characterize a conical pore leading to a nanometer sized electrode<sup>21</sup>, to evaluate the dimensions of a recessed nanometer-sized platinum nanoelectrode<sup>22</sup>, and to characterize various nanostructures through impedance measurements.<sup>23</sup>

In this chapter, I utilize steady-state carbon fiber amperometry combined with a model of diffusion-based transport to determine the inner diameter of a lipid nanotube present in the liposome model of exocytosis. This nanotube mimics a fusion pore and more direct comparisons to this pore can be made with a well-characterized, known nanotube diameter. Additionally, two experimental configurations were examined where a lipid nanotube was either connected between two vesicles (two-vesicle configuration) or attached/adhered directly to a glass pipette on one end and the outer vesicle on the other (tube-only configuration). The results show significant differences in lipid nanotube diameter between the two different configurations when tube lengths were  $<10\ \mu\text{m}$ . I report the direct measurement of the nanotube diameter versus nanotube length as calculated from steady-state current measurements. Finally, I present a theoretical model describing the differences between the two-vesicle and tube-only configurations.

## Experimental Methods

**Chemicals and materials.** The buffer for the liposome preparation was composed of 5 mM Trizma base/15 mM  $K_3PO_4$ /30 mM  $KH_2PO_4$ /10 mM  $K_2HPO_4$ /0.5 mM EDTA/1 mM  $MgSO_4$  at pH 7.4. Dopamine, catechol, and chloroform were all used as received. All chemicals were of analytical grade and purchased from Sigma-Aldrich (Sweden). Borosilicate glass (1.0 mm O.D., 0.78 mm I.D.) was obtained from Harvard Apparatus, UK.

**Liposome preparations and manipulations.** Surface immobilized liposomes were made from soybean polar lipid extract (Avanti Polar Lipids, Alabaster, AL) using a dehydration/rehydration method described previously<sup>10</sup>. Briefly, 1 mg of soybean polar extract in chloroform was dried in a round-bottom flask using a rotation evaporator (Büchi, Switzerland). The dried lipid film was rehydrated with 1 mL of buffer and stored in the refrigerator for ~24 h. The flask was then sonicated for ~15 min prior to 5  $\mu$ L of the lipid suspension being micropipetted onto a borosilicate coverslip (Menzel-Gläser, Braunschweig, Germany; 24 mm x 60 mm, #1) and subsequently dehydrated in a vacuum desiccator. The slide was transferred to the microscope and the film was rehydrated with buffer. This method yields liposomes of a specific lipid conformation: a unilamellar component attached to a multilamellar component that acts as a lipid reservoir.

Once this liposome conformation was identified, an injection pipette pulled with a commercial pipette puller (Model PE-21, Narishige Inc., London, UK) was back-filled with a 50 mM catechol solution and inserted into the unilamellar part of the liposome by means of a micromanipulator (Model MHW-3, Narishige, Inc, London, UK) with the aid

of an electroporation voltage pulse ( $\sim 30$ - $50$  V,  $\sim 1$  ms duration) generated by a constant voltage isolated stimulator (DS2A-Mk. II, Digitimer, Inc., Hertfordshire, UK). The counter electrode for electroporation was made from a pre-constructed  $5\text{-}\mu\text{m}$  carbon fiber tip (ProCFE from Dagan Corp, Minneapolis, MN). This counter electrode was maneuvered opposite the injection pipette via another micromanipulator. The injection pipette was used to eject catechol solution ( $50$  mM), by means of a Femtojet microinjector (Eppendorf / Brinkmann Instruments, Hauppauge, NY), into the unilamellar component.

Once the liposome was at a workable size (generally  $>50$   $\mu\text{m}$  in diameter), two different nanotube configurations were formed, examined, and compared. First, the injection pipette was manipulated to puncture through the second wall of the unilamellar liposome. The pipette was then slowly retracted into the interior of the parent vesicle, bringing with it lipid material adhered to the pipette tip and forming a lipid nanotube between parent vesicle and attachment pipette. This is the tube-only configuration and is illustrated in schematic B of Figure 5-1. Second, by injection of solution from the glass pipette, a small, inner vesicle (generally  $>5$   $\mu\text{m}$  in diameter) was created inside the parent vesicle with a lipid nanotube connection to the exterior. This is the two-vesicle configuration and is illustrated in schematic A of Figure 5-1. The inner vesicle for all experiments herein was filled with  $50$  mM catechol unless otherwise noted.

**Microscopy and digital video recording.** Liposome experiments were monitored using an Olympus IX-71 microscope (Olympus, Melville, NY) with a  $40\times$  oil objective (Olympus, UApo/340  $40\times$  oil iris, NA 1.35) using differential interference contrast (DIC) to give a pseudo-three dimensional appearance to the liposome. Experiments were



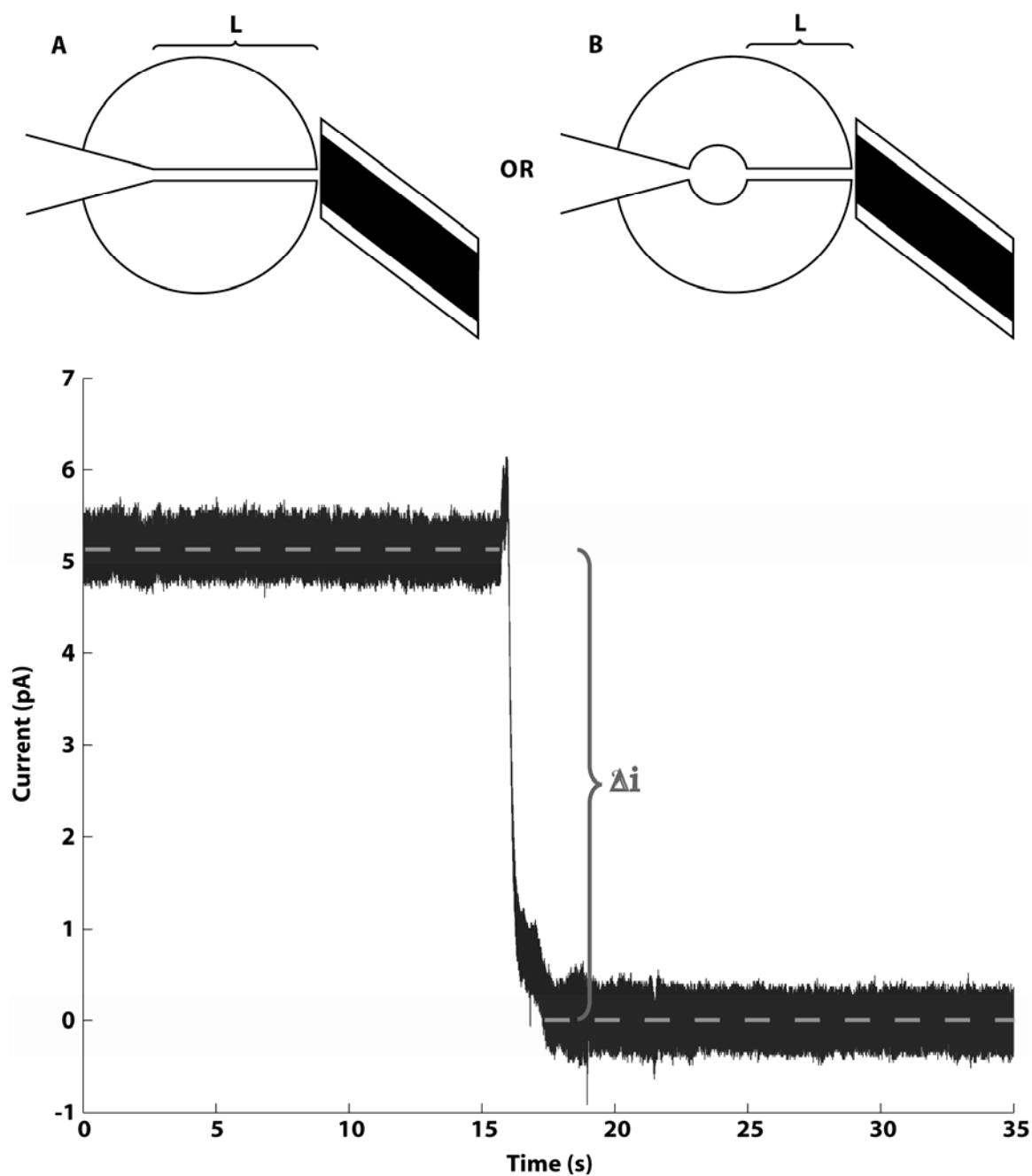


**Figure 5-1.** Representative current vs. time amperometric trace (bottom) illustrating how the change in current ( $\Delta i$ ) was measured. A steady-state current due to flux of material through the nanotube was measured in the tube-only configuration for this example. The background steady-state current was then established by removing the electrode from the nanotube-liposome junction, indicated by the  $\sim 5$  pA drop in baseline current. This corresponded to a calculated tube diameter of  $\sim 127$  nm for a tube  $\sim 17$   $\mu\text{m}$  in length. Schematics A and B represent the tube-only and two-vesicle configurations, respectively, and  $L$  indicates the nanotube length.

visually recorded using an Olympus SC20 digital color camera interfaced to a personal computer with Cell-A software (Olympus, Hamburg, Germany). Nanotube lengths were measured within the Cell-A software from digital images captured during electrochemistry measurements.

**Electrode fabrication and electrochemical data acquisition.** Carbon fiber working electrodes were fabricated by aspirating isolated 5- $\mu\text{m}$  diameter fibers into borosilicate glass capillaries (1.2 mm O.D., 0.69 mm I.D., Sutter Instrument Co., Novato, CA). The capillaries were subsequently pulled with a commercial micropipette puller (Model PE-21, Narishige, Inc., London, UK) and sealed with epoxy (Epoxy Technology, Billerica, MA). After beveling (Model BV-10, Sutter Instrument Co., Novato, CA) at 45 degrees and testing in 0.1 mM dopamine, electrodes were placed against the liposome-nanotube junction using a piezomicropositioner (PCS-750/1000, Burleigh Instruments, Fishers, NY). Working electrodes were held at +800 mV versus a silver/silver chloride reference electrode (Scanbur, Sweden) using an Axon 200B potentiostat (Molecular Devices, Sunnyvale, CA). The output was digitized at 5 kHz and filtered at 2 kHz via an internal four-pole lowpass Bessel filter. The output was further filtered via a 10 Hz lowpass digital filter within the AxoScope 10.2 software (Molecular Devices, Sunnyvale, CA) prior to analysis via MiniAnalysis software (Synaptosoft, Inc., Decatur, GA)

**Tube radius measurements.** With the nanotube in place, the 5- $\mu\text{m}$  carbon fiber electrode was placed at the nanotube-liposome junction and was allowed to rest until the current detected reached a stable, unchanging level. On average, this baseline was recorded for  $\sim 30$  s. Once a stable baseline had been observed, the injection pipette was moved to either lengthen or shorten the nanotube length (L). After the new length was

obtained, the measured current level was allowed to reestablish. This typically took as little as 10 s, but at times required several minutes. The reason for this is not entirely clear. This process of tube lengthening or shortening may be repeated several times for the same liposome. To obtain a background baseline measurement at the conclusion of an experiment, the electrode was maneuvered away from the nanotube-liposome junction and allowed to reach a steady-state current in the absence of electroactive species i.e. in buffer solution only. The difference in the measured current ( $\Delta i$ , illustrated by Figure 5-1) from this background can then be used to compute the diameter of the nanotube.

## Results and Discussion

**Initial nanotube measurements.** Using a steady-state amperometric detection allows determination of both the nanotube diameter and the effect that tube length has on this calculated diameter. The approach uses a steady-state diffusion measurement assuming two conditions: (1) the concentration gradient for the electroactive species along the tube is linear, and (2) the effective concentration at the end of the nanotube (i.e. at the nanotube-liposome junction) is zero. The second condition results because the redox species is totally consumed at the electrode surface when using constant potential amperometry, maintaining the redox species concentration at zero at the outer nanotube-liposome junction. To quantify the results of the electrochemical measurements, Fick's first law of diffusion was used, here written as diffusion through the nanotube as

$$J(\ell) = -D \frac{\partial C(\ell)}{\partial \ell} \quad \text{Equation 5-1}$$

where  $J$  is the flux of material at a given distance  $\ell$  along the tube,  $D$  is the diffusion coefficient of the selected redox molecule,  $\partial C$  is the change in concentration of the redox

molecule at a given distance  $\ell$ , and  $\partial\ell$  is the change in distance along the tube. With the assumption that the concentration gradient along the tube length is constant, one can rewrite Equation 5-1 as follows:

$$\frac{\Delta i}{nFA} = D \left[ \frac{dC}{d\ell} \right]_{\ell=0} \quad \text{Equation 5-2}$$

where  $\Delta i$  is the difference in current measured during the experiment,  $n$  is the number of moles of electrons transferred per mole of electroactive species,  $F$  is Faraday's constant (96,485 coulombs/mole electrons), and  $A$  is the cross-sectional area of the nanotube. Further substituting for the area of the tube cross-section, employing the assumption of a constant linear concentration gradient, and examining at a tube length ( $L$ ) gives Equation 5-3 as

$$\frac{\Delta i}{nF\pi r^2} = D \frac{\Delta C}{L} \quad \text{Equation 5-3}$$

Solving for the radius gives

$$r = \sqrt{\frac{\Delta i}{nF\pi D \frac{\Delta C}{L}}} \quad \text{Equation 5-4}$$

This provides a relationship between the nanotube radius (or diameter when  $r$  is doubled) and the measurable experimental parameters  $\Delta i$  and  $L$ . For all experiments reported herein, catechol was the redox molecule used at a concentration of 50 mM,  $n$  is 2 moles of electrons per mole of catechol oxidized, and a diffusion coefficient ( $D$ ) of  $7.0 \times 10^{-6} \text{ cm}^2 \cdot \text{s}^{-1}$  was used.<sup>24</sup> To determine the  $\Delta i$  attributed to catechol flux out of the nanotube,

the steady-state current obtained without the nanotube present (background) was subtracted from the steady-state current established in the presence of the nanotube. A representative current versus time trace illustrating a typical  $\Delta i$  is shown in Figure 5-1.

A series of electrochemical measurements have been collected sequentially to generate a “staircase-like” current vs. time plot (Figure 5-2). Here a lipid nanotube has been pulled inside the parent vesicle to a starting length of  $\sim 17\ \mu\text{m}$ . After a steady current was established (at  $t = \sim 20\ \text{s}$  in Figure 5-2), the tube length was decreased to  $\sim 12\ \mu\text{m}$ . This was accompanied by an increase in the measured current due to an anticipated increase in catechol flux through this new, shorter tube length. Decreasing the tube length further to  $\sim 7\ \mu\text{m}$  brought about another current rise and a new, higher current level. This effect was reversible with the current levels subsequently decreasing upon increasing the nanotube length to  $\sim 13\ \mu\text{m}$  and  $\sim 18\ \mu\text{m}$ , respectively. The background current to be subtracted was determined at the conclusion of the experiment by maneuvering the electrode away from the nanotube-liposome junction (at  $t = \sim 120\ \text{s}$ , Figure 5-2). Making measurements in this manner can help minimize small experimental variabilities due to electrode sensitivity and injection pipette tip sizes as well as interrogate a range of tube lengths for both configurations under nearly identical conditions.

**Comparison of tube measurements in the two-liposome and tube-only configurations.** Using the sequential method of data collection outlined above, the two-vesicle and tube-only configurations were investigated to examine the effect of liposome neck geometry on tube diameter. The two-vesicle mode is of particular interest with its relation to the fusion pore between a cell and a releasing vesicle. The fusion pore is analogous to a small, hollow nanotube allowing materials to be exchanged from the

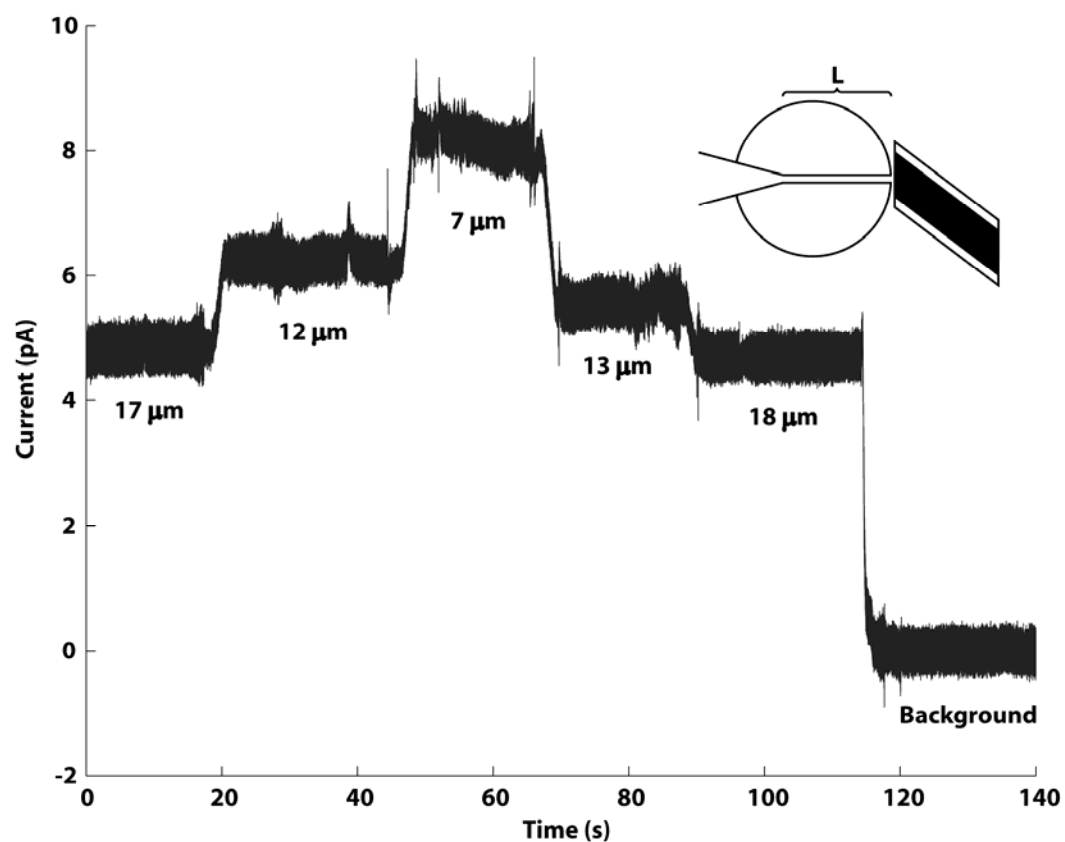


**Figure 5-2.** Representative current vs. time amperometric trace for a tube-only configuration experiment. The steady-state currents for a series of 5 nanotube lengths (indicated below each baseline) from the same liposome generate a staircase-like amperometric trace when collected sequentially. At the end of the series, the background steady-state current was established by removing the electrode from the nanotube-liposome junction.

vesicle interior to the extracellular space. Previously this laboratory has shown that the nanotube connecting the inner and parent vesicles in the liposome artificial cell model acts similarly to that observed for exocytotic release of dopamine from PC12 cells.<sup>10</sup> Likewise, the tube-only configuration is of interest for two reasons. First, this configuration could serve as a systematic control of the liposome-lipid nanotube model. Other studies suggest that tubes made by point-force methods using micropipettes have diameters independent of length.<sup>25</sup> Second, the tube-only configuration is similar to the structures used to obtain previous estimates of soybean lipid extract nanotube diameters. In particular, the aforementioned coalescence measurements required the lipidic tube to be directly adhered to the tip of the manipulation pipette.

Using the diffusion-based model (Equations 5-1 to 5-4) with its applied assumptions, a comparison of  $\Delta i$  relative to the inverse of tube length can be written as follows:

$$\Delta i = nF\pi r^2 D \Delta C \frac{1}{L} \quad \text{Equation 5-5}$$

Here the linear trend observed for  $\Delta i$  versus  $1/L$  suggests the model is suitable for determining the nanotube dimensions over the range of nanotube lengths probed. This analysis assumes, however, that the diameter of the nanotube remains nearly constant over the range of nanotube lengths examined. As one can see from Figure 5-3, a linear trend for each configuration is observed. The apparent slopes differ, however, indicating different nanotube dimensions for the two configurations. An *average* tube diameter over the range of nanotube lengths investigated was calculated from the slope of the linear fit for  $\Delta i$  versus  $1/L$ . The slope is the product of  $n$ ,  $F$ ,  $\pi$ ,  $r^2$ ,  $D$ , and  $\Delta C$  as per

Equation 5-5. The *average* tube diameter was found to be  $114 \pm 19$  nm and  $47 \pm 7$  nm for the tube-only and two-vesicle configurations, respectively.

Alternatively, the nanotube diameter can be directly computed via substitution of measured  $\Delta i$  and nanotube length into Equation 5-4. The resultant data for calculated nanotube diameter at a given length is shown in Figure 5-4. The two configurations yielded different relationships over the range of lengths examined. With a tube-only configuration (Figure 5-4, gray trace), a nearly constant tube diameter independent of nanotube length is suggested ( $123 \pm 4$  nm for 11 point measurements). Linear regression analysis confirmed the slope was statistically non-different from zero. The linear trend observed for the  $\Delta i$  vs.  $1/L$  relationship (Figure 5-3) also supports this observation because this relationship assumes the nanotube dimension is independent of nanotube length. This agreement supports not only the validity of the measurement protocol, but also the electrochemical model with its basic assumptions.

Conversely, the two-vesicle configuration (Figure 5-4, black trace) exhibited a dependence on tube length. If the slope of the  $\Delta i$  vs.  $1/L$  relationship is used to determine an *average* tube diameter for the two-vesicle configuration, the estimation will be considerably smaller than what is observed from individually calculated measurements. This is because, as revealed in Figure 5-4, the diameter is *not* independent of nanotube length.

#### **Modeling the difference in the trend of diameter between nanotube configurations.**

The deviation of tube diameter with length at  $L < 10$   $\mu\text{m}$  for the two-vesicle configuration might be attributed to the flexible, high curvature “neck” regions present (this is shown in the model in Figure 5-5). To investigate these differences, a simple model has been



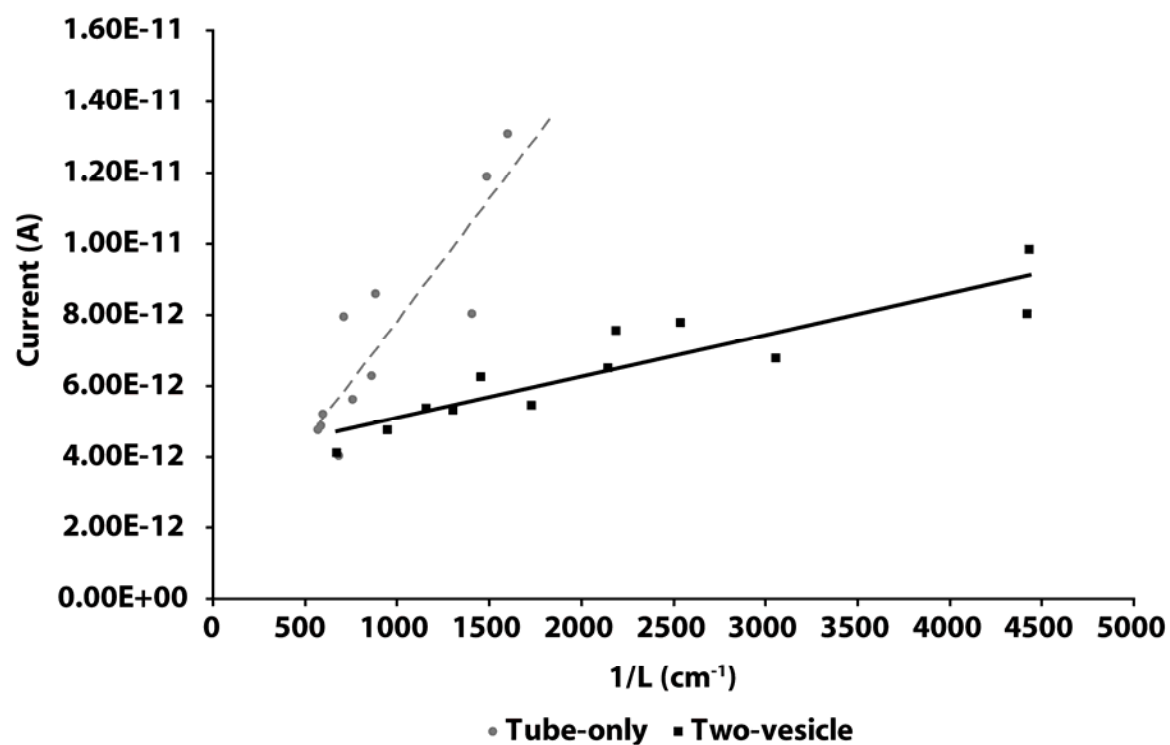


**Figure 5-3.** Measured current versus inverse of the nanotube length for two-vesicles (■) and tube-only configuration (●). The linear fits verify that the diffusion-based model and applied assumptions can be used to approximate the *average* diameter of the nanotube.

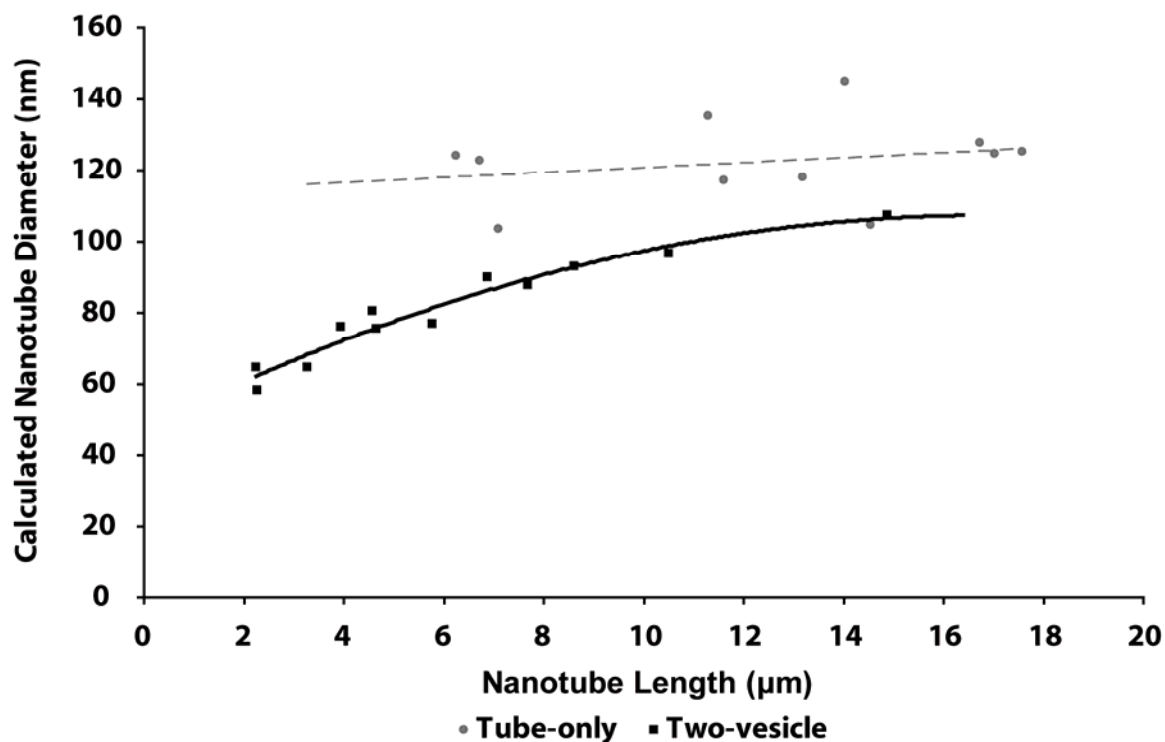


**Figure 5-4.** Calculated diameter versus nanotube length for the two-vesicle configuration (■) and the tube-only configuration (●);  $n=3$  different liposome preparations were used for each configuration. The two-vesicle and tube-only configurations have 12 and 11 individual point measurements, respectively. Lines represent quadratic and linear fits for two-vesicle and tube-only, respectively.

developed considering that the two-vesicle system contains two flexible neck regions (one where the nanotube connects to the parent vesicle and one where the nanotube connects to the inner vesicle) and the tube-only configuration has just one flexible neck region (where the nanotube connects to the membrane of the parent vesicle). To model the effect of length on tube diameter, the neck region at the glass pipette-lipid interface is assumed to be constant or “fixed” regardless of nanotube length.<sup>26</sup> This might be the dominant factor in determining lack of change in nanotube diameter as a function of length. Alternatively, one could use membrane properties to explain the data. Membrane properties that are dependent on tube length include membrane tension and bending rigidity. As this system contains a multilamellar reservoir of lipid, tension is essentially constant. However, as nanotube diameter is increased the bending energy is decreased driving the tube to wider diameter at longer tube lengths. I propose that the pipette-nanotube neck is constant and the energy of the remaining liposome-nanotube neck drives the tube to smaller diameter. The bending and neck energies counteract and lead to a nearly constant measured nanotube diameter as a function of length in the tube-only configuration.

The situation when two vesicles are present at either end of the nanotube is different. Experimentally, a larger tube dimension is observed at increased tube length. The thermodynamic bending energy of the tube is reduced as the tube diameter is larger. If the two flexible necks in this configuration energetically repel each other, this would result in a promotion of tube thinning at shorter tube lengths (Figure 5-5, arrows). The thinning brought about by neck repulsion could be in direct competition with the tube bending energy trying to expand its size, which would prevail at longer tube lengths. At

shorter nanotube lengths (<10  $\mu\text{m}$ ), the interaction between the two necks must be taken into account in the free energy of the tube, thus driving the calculated tube diameter to be smaller than that observed for the tube-only configuration. As the distance between the two necks increases (i.e. by increasing nanotube length), the bending energy of the tube increases and appears to overcome and dominate the apparent reduced repulsive interaction between the necks.

The rigorous theoretical explanation for the neck interactions and their effect on tube diameter has been suggested. This model introduces a term for the changing energy of this neck interaction dependent on the distance that separates the necks. First the free energy of the membrane can be expressed as<sup>27</sup>

$$F = \int \frac{\kappa}{2} (2H)^2 dA + \sigma A - pV - fL \quad \text{Equation 5-6}$$

where  $\kappa$  is the bending rigidity,  $H$  is the mean curvature of the membrane,  $A$  is the surface area of the membrane,  $\sigma$  is the membrane surface tension,  $p$  is the interior pressure of the volume ( $V$ ) enclosed by the membrane, and  $f$  is the point force necessary to pull the membrane a distance  $L$ . The elastic free energy of the overall system can be expressed as a sum of the individual contributions of the membrane geometries present

$$F_{TOTAL} = F_V + F_T + F_N + F_{INTER} \quad \text{Equation 5-7}$$

where  $F_{TOTAL}$  is the total elastic energy of the system equaling the sum of the elastic energy of the vesicles ( $F_V$ ), the nanotube ( $F_T$ ), the neck regions ( $F_N$ ), and the neck interaction ( $F_{INTER}$ ). For the experimental set-up, it can be assumed that  $F_V$ ,  $F_T$ , and  $F_N$  are constant and independent of tube length<sup>25</sup>, thus  $F_{INTER}$  can be combined with the

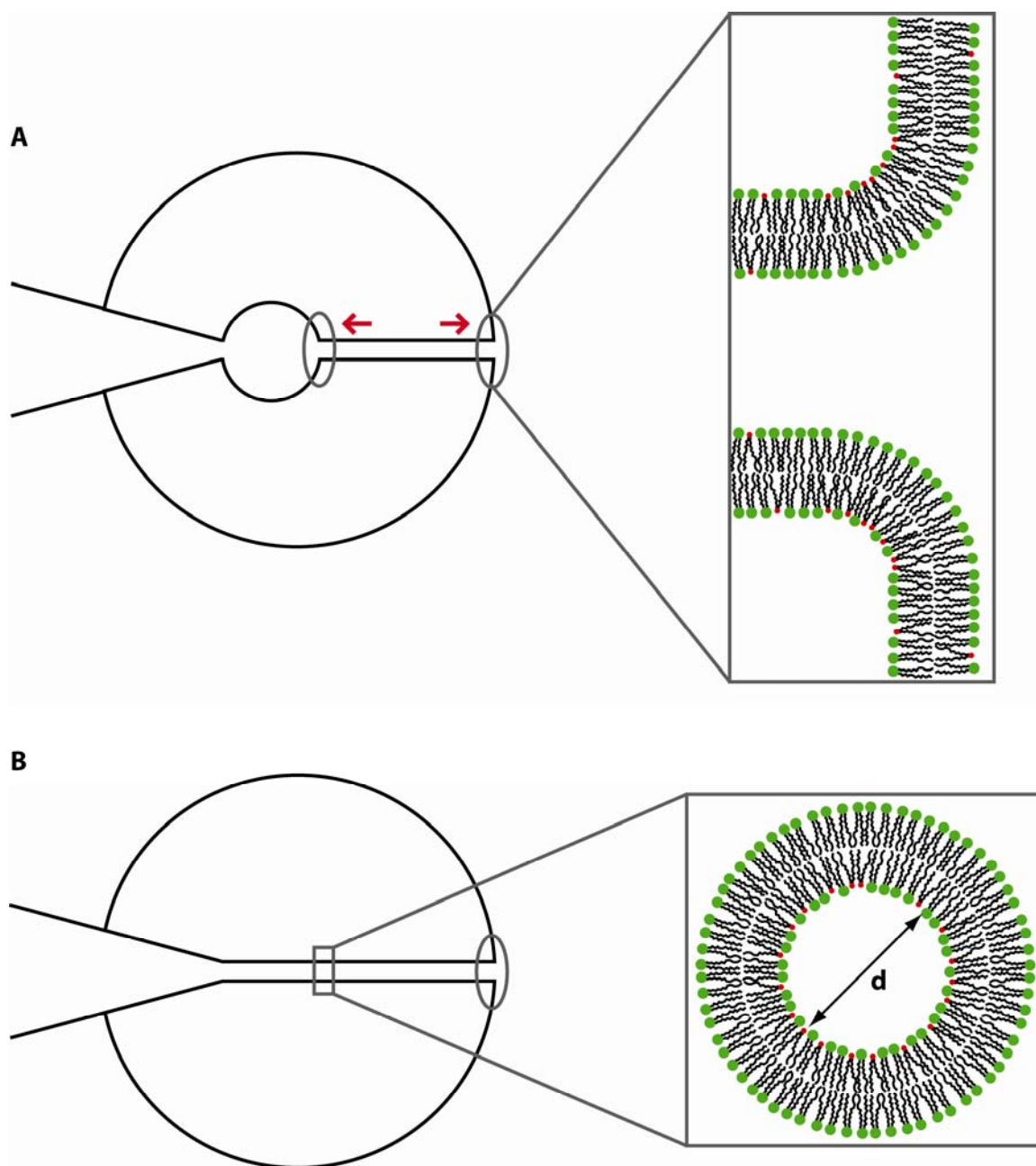


**Figure 5-5.** Model of the two-vesicle (A) and tube-only (B) configurations. The grey ovals indicate where the flexible neck regions are located in each configuration. The red arrows represent the repulsion of the necks present in the two-vesicle configuration. The enlargement in A is a side-view of the flexible neck region present in both configurations. Here the nanotube continues into the outer parent vesicle membrane via a junction of high curvature. The enlargement in B is a cross-sectional view of the nanotube present in both configurations with the inner diameter ( $d$ ) indicated. The lipids are not drawn to scale.

bending energy to derive how these two energies can influence the tube diameter as length is varied.  $F_{\text{INTER}}$  for the two-vesicle and tube-only configurations can be expressed as

$$F_{\text{INTER}(\text{Two-Vesicles})} = \frac{R_t^2}{L^\alpha} \quad \text{Equation 5-8}$$

$$F_{\text{INTER}(\text{Tube-Only})} = \frac{R_t R_2}{L^\alpha} \quad \text{Equation 5-9}$$

where  $R_t$  is nanotube radius,  $R_2$  is the radius of the tube closest to the orifice of the injection pipette, and  $L$  is the distance separating the necks (which is analogous to the nanotube length) with model fitting parameter  $\alpha$ .  $R_2$  was assumed to be constant relative to tube length according to Bensimon and coworkers.<sup>26</sup> Using the formula for the free elastic energy expression for the membrane,  $\alpha$  was phenomenologically observed to be  $\frac{1}{3}$  and 1 for two-vesicle and tube-only, respectively. This is consistent with the theory that at short nanotube lengths the neck interactions have a greater effect on the nanotube diameter and at long nanotube lengths the lipid bending energy effects are more likely to dominate.

## Conclusions

By exploiting the capabilities of steady-state electrochemical measurements, I have measured the inner diameter of a lipid nanotube using Fick's first law of diffusion in conjunction with an imposed linear concentration gradient of electroactive molecules over the length of the nanotube. Comparing the nanotube diameter to the corresponding

nanotube length suggested membrane elastic energy was important in determining the size of the tube and differed when the nanotube was connected on either end to two vesicles or to a vesicle on one end and a pipette tip on the other. I assumed that a repulsive interaction between neck regions could be used, in part, to explain the trends observed. A more rigorous approach based on the minimization of the elastic energies of the different regions of the nanotube, vesicles, and connecting necks was consistent with this assumption. As a final comment, these data also exemplify that electrochemical measurements can be used in special cases to exceed the limits of dimensional analysis for optical microscopy.

## References

- (1) Hirschberg, K.; Miller, C. M.; Ellenberg, J.; Presley, J. F.; Siggia, E. D.; Phair, R. D.; Lippincott-Schwartz, J. *J Cell Biol* **1998**, *143*, 1485-1503.
- (2) Polishchuk, R. S.; Polishchuk, E. V.; Marra, P.; Alberti, S.; Buccione, R.; Luini, A.; Mironov, A. A. *J Cell Biol* **2000**, *148*, 45-58.
- (3) Onfelt, B.; Nedvetzki, S.; Yanagi, K.; Davis, D. M. *J Immunol* **2004**, *173*, 1511-1513.
- (4) Rustom, A.; Saffrich, R.; Markovic, I.; Walther, P.; Gerdes, H. H. *Science* **2004**, *303*, 1007-1010.
- (5) Karlsson, M.; Sott, K.; Cans, A. S.; Karlsson, A.; Karlsson, R.; Orwar, O. *Langmuir* **2001**, *17*, 6754-6758.
- (6) Karlsson, R.; Karlsson, M.; Karlsson, A.; Cans, A. S.; Bergenholtz, J.; Akerman, B.; Ewing, A. G.; Voinova, M.; Orwar, O. *Langmuir* **2002**, *18*, 4186-4190.
- (7) Karlsson, A.; Sott, K.; Markstrom, M.; Davidson, M.; Konkoli, Z.; Orwar, O. *Journal of Physical Chemistry B* **2005**, *109*, 1609-1617.
- (8) Jesorka, A.; Orwar, O. *Annual Review of Analytical Chemistry* **2008**, *1*, 801-832.
- (9) Cans, A. S.; Wittenberg, N.; Eves, D.; Karlsson, R.; Karlsson, A.; Orwar, O.; Ewing, A. *Analytical Chemistry* **2003**, *75*, 4168-4175.
- (10) Cans, A. S.; Wittenberg, N.; Karlsson, R.; Sombers, L.; Karlsson, M.; Orwar, O.; Ewing, A. *Proc Natl Acad Sci U S A* **2003**, *100*, 400-404.
- (11) Sombers, L. A.; Wittenberg, N. J.; Maxson, M. M.; Adams, K. L.; Ewing, A. G. *ChemPhysChem* **2007**, *8*, 2471-2477.



- (12) Tokarz, M.; Hakonen, B.; Dommersnes, P.; Orwar, O.; Akerman, B. *Langmuir* **2007**, *23*, 7652-7658.
- (13) Cuvelier, D.; Derenyi, I.; Bassereau, P.; Nassoy, P. *Biophysical Journal* **2005**, *88*, 2714-2726.
- (14) Polidori, A.; Michel, N.; Fabiano, A. S.; Pucci, B. *Chem Phys Lipids* **2005**, *136*, 23-46.
- (15) Lauf, U.; Fahr, A.; Westesen, K.; Ulrich, A. S. *ChemPhysChem* **2004**, *5*, 1246-1249.
- (16) Brazhnik, K. P.; Vreeland, W. N.; Hutchison, J. B.; Kishore, R.; Wells, J.; Helmerson, K.; Locascio, L. E. *Langmuir* **2005**, *21*, 10814-10817.
- (17) Kameta, N.; Masuda, M.; Minamikawa, H.; Shimizu, T. *Langmuir* **2007**, *23*, 4634-4641.
- (18) Bo, L.; Waugh, R. E. *Biophysical Journal* **1989**, *55*, 509-517.
- (19) Hochmuth, R. M.; Wiles, H. C.; Evans, E. A.; Mccown, J. T. *Biophysical Journal* **1982**, *39*, 83-89.
- (20) Waugh, R. E.; Hochmuth, R. M. *Biophysical Journal* **1987**, *52*, 391-400.
- (21) Zhang, B.; Zhang, Y.; White, H. S. *Analytical Chemistry* **2006**, *78*, 477-483.
- (22) Sun, P.; Mirkin, M. V. *Journal of the American Chemical Society* **2008**, *130*, 8241-8250.
- (23) Sun, L.; Crooks, R. M. *Journal of the American Chemical Society* **2000**, *122*, 12340-12345.
- (24) Durgbanshi, A.; Kok, W. T. *Journal of Chromatography A* **1998**, *798*, 289-296.

- (25) Frolov, V. A.; Lizunov, V. A.; Dunina-Barkovskaya, A. Y.; Samsonov, A. V.; Zimmerberg, J. *Proc Natl Acad Sci U S A* **2003**, *100*, 8698-8703.
- (26) Michalet, X.; Bensimon, D.; Fourcade, B. *Phys Rev Lett* **1994**, *72*, 168-171.
- (27) Derenyi, I.; Julicher, F.; Prost, J. *Phys Rev Lett* **2002**, *88*, 238101.

## **Chapter 6**

### **Lipid membrane composition controls the diameter of a lipid nanotube in an artificial cell model for exocytosis**

#### **Introduction**

The major component of lipid bilayer membranes in the eukaryote cell consists of phospholipids, where phosphatidylcholine (PC) is the most predominant. Other major phospholipids found are phosphatidylethanolamine (PE), phosphatidylserine, phosphatidylinositol, and phosphatidic acid. Lipid membranes serve essential functions within living cells,<sup>1</sup> including the establishment of compartmentalization of the cell and boundaries for organelles, the transduction of cellular signaling,<sup>2, 3</sup> and the regulation of both electrical and physical cellular properties.<sup>4</sup> Furthermore, the dynamic properties of the membrane allow budding, fission, fusion, and deformation of the lipid bilayer into high-curvature nanotubes and vesicles that are important features in cell division, exocytosis, endocytosis, as well as intercellular transport and intracellular trafficking.<sup>5</sup> Lipid membranes can be forced to bend by membrane proteins by way of physical forces pulling and bending the membrane upon insertion of the protein into the lipid bilayer. Membrane shape can also be affected by the composition of lipids in the membrane.<sup>5</sup> The intracellular shuttling of material between organelles and the plasma membrane involves budding or tubulation of the donor membrane followed by fusion of the cargo material with the target membrane. However, this intracellular trafficking occurs while still maintaining the distinctly different composition of proteins and lipids in organelles and the plasma membrane. Therefore, the two most common phospholipids present in the endoplasmic reticulum (ER), mitochondria, and Golgi of eukaryotic cells are

phosphatidylcholine (PC) and phosphatidylethanolamine (PE),<sup>6</sup> though the relative amounts vary widely between the different organelles. These variations in membrane composition are thought to depend on mechanisms for sorting of lipids and proteins in the membrane that might involve deformation into high-curvature membrane structures, but this is still not fully understood. It has, however, been shown, using imaging mass spectrometry, that the lipid composition of the mating junction of *Tetrahymena* contains elevated amounts of conical-shaped lipids, specifically PE, as compared to unmated cells.<sup>7</sup> The mating regions have many highly curved pore openings to facilitate the exchange of genetic material between the two cells. These examples suggest that the properties of lipids might play a significant role in lipid sorting through the formation of nano-sized, highly contoured structures like fusion pores and tubular-like structures.

Depending on the molecular geometry, phospholipids can be described as having an influence on a positive, negative, or neutral intrinsic curvature of the lipid bilayer. This classification is based on the cross-sectional area of the hydrophilic headgroup as compared to the hydrophobic acyl chain tailgroup. PC is categorized as a cylindrically-shaped lipid with its headgroup occupying approximately the same cross-sectional area as compared to its two acyl chains (Figure 6-1A). A lipid of this shape preferentially forms lamellar bilayers with little to no curvature (i.e. a flat, non-bending structure), where the head and tail groups occupy approximately the same area. In contrast to PC, PE has a significantly smaller headgroup when compared to PC due to three fewer methyl groups (Figure 6-1B). PE therefore, exhibits more of an inverted cone shape as its headgroup is smaller in cross-sectional area with respect to its tailgroups. When incorporated into a flat leaflet, PE induces a negative spontaneous curvature, preferentially bending the

membrane in a concave direction relative to normal. Previous work has shown that augmentation with phospholipids of various shapes can influence the dynamic aspects of exocytosis (release of neurotransmitters from vesicles into the extracellular space) as monitored by carbon fiber amperometry.<sup>8</sup> More specifically, PE accelerated the release while PC slowed it down. The inverted cone shape of PE likely aids in the formation of the fusion pore geometry (i.e. a short nanotube with two transition neck regions), thus leading to acceleration of the release process. PC, however, with its cylindrical shape does not fit as well into the fusion pore geometry and therefore prolongs the kinetics of release.

In this chapter, I employed a protein-free artificial cell model for exocytosis, previously described in Chapter 5 in order to examine the role of phospholipids controlling the size of a lipid nanotube based on intrinsic curvature theory. Basically an inside-out electroinsertion of a glass pipette filled with solution of the oxidizable substance catechol was made in the membrane of a giant unilamellar liposome. This was then used to pull a lipid nanotube into the inside of the liposome by moving the pipette tip towards the center. A model of diffusion-based transport previously described in Chapter 5 was implemented to relate the steady-state amperometric current from an oxidizable substance diffusing from the pipette tip through the connecting tube to the outside by use of a carbon fiber electrode placed at the nanotube opening. Simultaneous video microscopy was used to measure the lipid nanotube length and a steady-state diffusion model was used to determine the inner diameter of the nanotube in the same manner as in Chapter 5. Lipid augmentations of the liposomes made from soybean polar lipid extract were prepared using two different shaped phospholipids, PC and PE. The

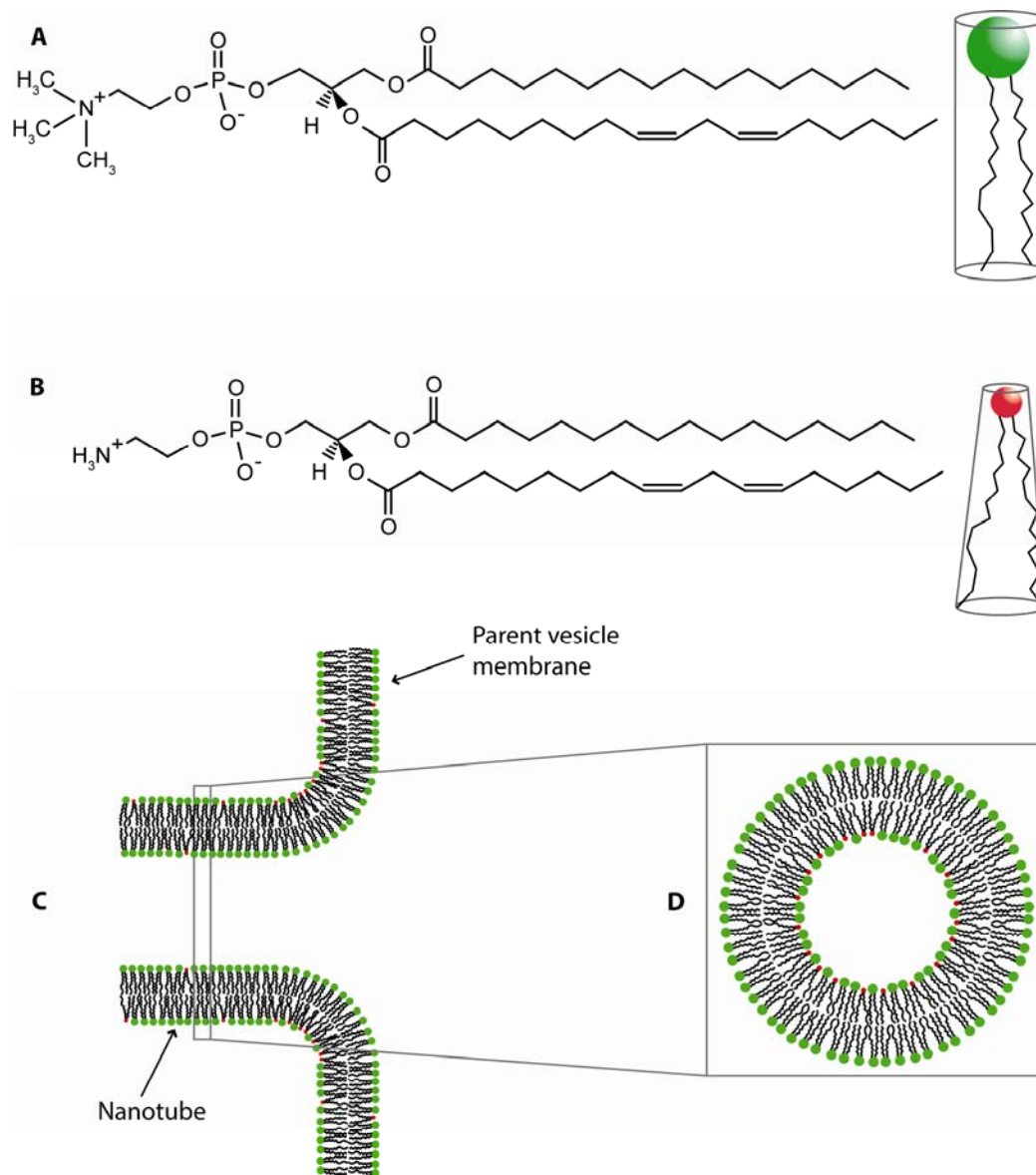


**Figure 6-1.** Chemical structures of (A) phosphatidylcholine (PC) and (B) phosphatidylethanolamine (PE) along with a corresponding illustration showing the volumes occupied by the head- and tailgroups. (C) Flexible neck region where the highly-curved nanotube meets the relatively flat parent vesicle membrane. (D) Cross-section of the nanotube.

cylindrical shaped PC increased the diameter of the nanotube, whereas the inverted cone shaped PE decreased the diameter, supporting the hypothesis that lipid intrinsic curvature has the ability to affect the sizes of highly-contoured structures in biology.

## **Experimental Methods**

**Chemicals and materials.** The rehydration buffer for the liposome preparation was composed of 5 mM Trizma base/15 mM  $K_3PO_4$ /30 mM  $KH_2PO_4$ /10 mM  $K_2HPO_4$ /0.5 mM EDTA/1 mM  $MgSO_4$  at pH 7.4. Dopamine, catechol, and chloroform were all used as received. All lipids were purchased from Avanti Polar Lipids, Alabaster, AL and all other chemicals were of analytical grade and purchased from Sigma-Aldrich (Sweden). Borosilicate glass (1.0 mm O.D., 0.78 mm I.D.) was obtained from Harvard Apparatus, UK.

**Liposome preparations and manipulations.** Surface-immobilized giant unilamellar soybean liposomes (SBL) were made from soybean polar lipid extract as previously described in Chapter 5. Augmentations of the SBL preparation were made with soy phosphatidylcholine (PC) or soy phosphatidylethanolamine (PE) at 25% by total weight. Briefly, 250  $\mu$ g of lipid to be added (either PC or PE) was combined with 750  $\mu$ g of soybean polar lipid extract for 1 mg of total lipid material. This quantity of lipid is analogous to the total weight of lipid used to make control SBLs. A summary of the resultant membrane compositions studied can be found in **Table 6-1**.

**Nanotube radius measurements and calculations.** Previously I described the determination of the inner diameter of a lipid nanotube as a function of its length by implementing electrochemical detection for two different sample configurations: two-

vesicle and tube-only in Chapter 5. For this chapter, the tube-only configuration shown in Figure 6-2 will solely be used to simplify data interpretation as well as to illustrate how lipid membrane composition can regulate nanotube dimensions in the absence of protein involvement. This configuration has the nanotube directly adhered to the injection pipette, forming a tubular contact to the outer parent vesicle membrane. From this nanotube, the flux of catechol was measured using carbon fiber amperometry. A 5- $\mu\text{m}$  carbon fiber microelectrode was placed at the nanotube-liposome junction and when a stable current level was reached, a baseline was recorded for  $\sim 30$  s. Once a stable baseline had been recorded, the injection pipette was maneuvered to either elongate or truncate the nanotube length. After the new length was obtained, the current was allowed to stabilize. This could take from as little as 10 s up to several minutes. The reason for this is not entirely clear. This process of tube lengthening or shortening may be repeated several times for the same liposome, allowing for a range of nanotube lengths to be investigated under controlled conditions i.e. same injection pipette, liposome, detection electrode, temperature, etc. The electrode was then moved away from the nanotube-liposome junction and allowed to reach a steady current in the absence of electroactive species to establish a background level. The difference in the measured current ( $\Delta i$ , illustrated by Figure 6-2, bottom) from this background along with nanotube length can then be used to compute the diameter of the nanotube based on the previously derived



<b>Lipid Component</b>	<b>% for SBL</b>	<b>% for PC+</b>	<b>% for PE+</b>
PE	22.1	16.6	41.6
PI	18.4	13.7	13.7
PC	45.7	59.3	34.3
PA	6.9	5.2	5.2
LPC	---	---	---
OTHER	6.9	5.2	5.2

**Table 6-1.** Membrane composition for soybean liposomes (SBL), elevated PC (PC+), and elevated PE (PE+). All amounts are percentages (based on weight) of the total lipid content. SBL information was provided by Avanti Lipids. Lipid augmentation was made by combining 250  $\mu$ g of the lipid to be elevated with 750  $\mu$ g of soy polar extract to give 1 mg of total lipid in the preparation. This is equivalent to 1 mg of total lipid used to construct control SBLs.

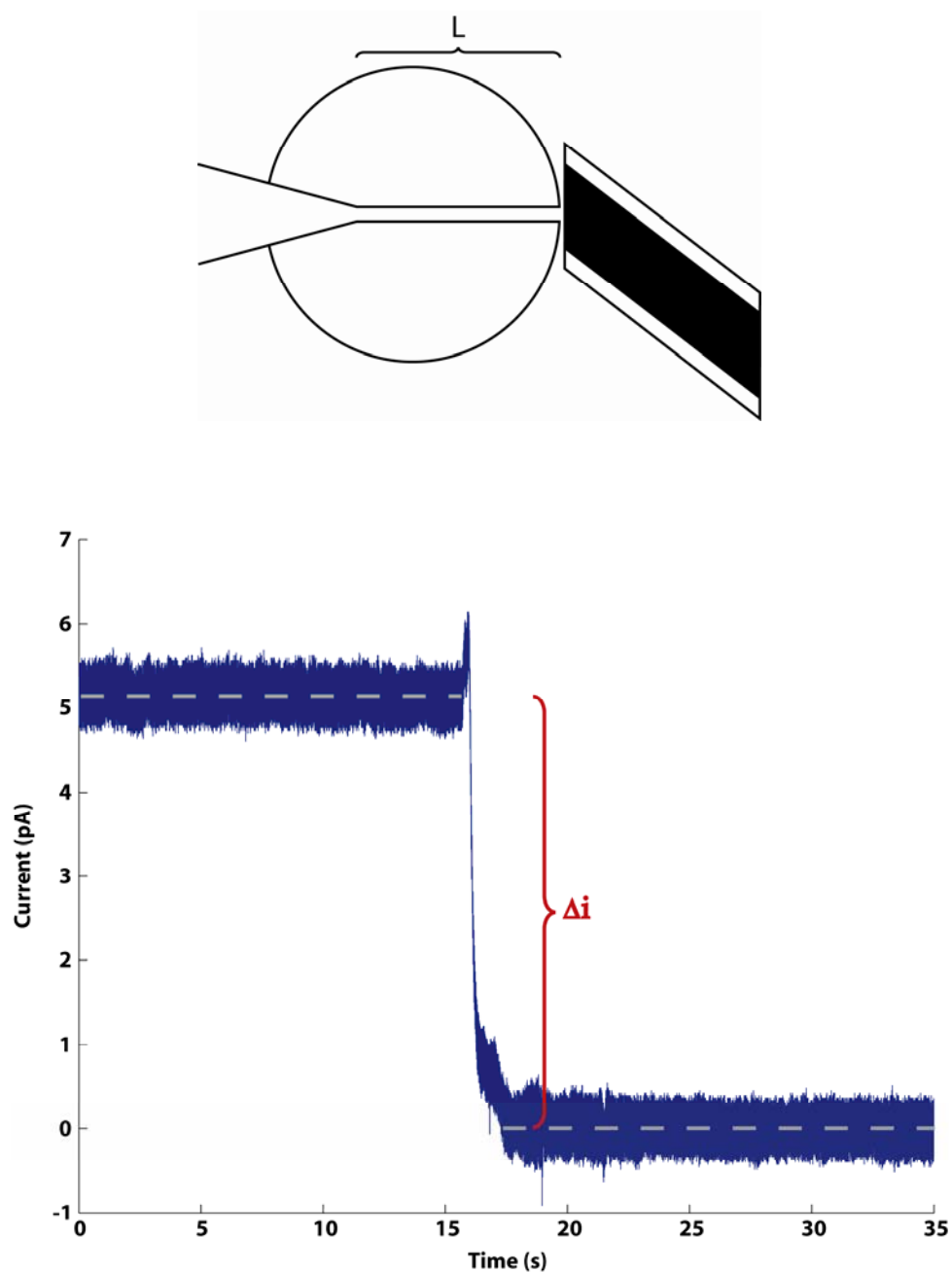


**Figure 6-2.** (Top) Schematic model of the tube-only configuration (top).  $L$  indicates the nanotube length. (Bottom) Representative current vs. time amperometric trace illustrating how the change in current ( $\Delta i$ ) was measured. A steady-state current due to flux of material through the nanotube was measured and the background steady-state current was then established by removing the electrode from the nanotube-liposome junction. This was followed by the  $\sim 5$  pA drop in baseline current and corresponded to a calculated nanotube diameter of  $\sim 127$  nm for a nanotube  $\sim 17$   $\mu\text{m}$  in length. For this example, the lipid preparation used was the control soybean polar lipid extract (SBL).

relationship

$$r = \sqrt{\frac{\Delta i}{nF\pi D \frac{\Delta C}{L}}} \quad \text{Equation 6-1}$$

where  $r$  is the radius of the nanotube of a given length ( $L$ ),  $\Delta i$  is the change in measured current with respect to background,  $n$  is the number of moles of electrons transferred per mole of redox species (for catechol, this is equal to 2),  $F$  is Faraday's constant (96,485 coulombs/mole of electrons),  $D$  is the diffusion coefficient of the selected redox species (for catechol, this is equivalent to  $7.0 \times 10^{-6} \text{ cm}^2 \cdot \text{s}^{-1}$ )<sup>9</sup>,  $\Delta C$  is the change in concentration of catechol over the nanotube length.  $\Delta C$  for all experiments, unless otherwise noted, was 50 mM catechol.

## Results and Discussion

**Lipid composition affects intrinsic curvature in lipid nanotubes.** In a protein-free liposome cell model the effect of lipid composition on lipid nanotube size was investigated using three different liposome compositions. The preparation of soybean liposomes (SBL) was constructed solely from soybean polar lipid extract, and the two other SBLs were either augmented with 25% by weight addition of phosphatidylcholine (PC+) or phosphatidylethanolamine addition (PE+). A summary of the lipids present (and their relative abundance percentages) for each of the three liposome preparation can be found in **Table 6-1**. These three compositions have similar PC and PE content to that in some cellular organelles and junctions<sup>6</sup> where some of these are known to form tubules facilitating intracellular transport.<sup>10, 11</sup> First, the SBL preparation has similar PC and PE

content to both the inner mitochondria and Golgi. Next, the PC and PE levels found in the rough ER are comparable to composition of the PC+ preparation. Lastly, the PC and PE content of a synapse is similar that of the PE+ preparation.

Based on intrinsic curvature theory, it was hypothesized that upon addition of a cylindrically-shaped lipid like PC, the measured nanotube diameter would increase due to this lipid shape not being able to accommodate the high-curvature demands of a tube-shaped geometry (see Figure 6-1C and D). In addition, PC preferentially accumulates in the outer leaflet of eukaryote cell membrane,<sup>12-14</sup> thus driving the expansion of the inner nanotube diameter. This occurs via an inadvertent expansion of the nanotube outer diameter that is thermodynamically driven by the overall increased membrane bending rigidity due to additional PC. Conversely, I hypothesized that upon addition of an inverted cone-shaped lipid like PE, the measured nanotube diameter would decrease due to a lowering of the energy in the high curvature regions, such as the flexible neck region where the nanotube meets the outer vesicle membrane (Figure 6-1C) and the inner leaflet of the nanotube cross-section (Figure 6-1D).

**Electrochemical measurements of lipid nanotube diameter.** To probe the theory that lipid composition regulates intrinsic curvature of lipid nanotubes, electrochemical measurements of catechol diffusion from nanotubes were carried out for the three different lipid preparations summarized in **Table 6-1**. The two experimental parameters measured ( $\Delta i$  and nanotube length) can be related to one another by a rearrangement of Equation 6-1 to give

$$\Delta i = nF\pi r^2 D \Delta C \frac{1}{L} . \quad \text{Equation 6-2}$$

A plot of the  $\Delta i$  versus the inverse of the nanotube length for each preparation is shown in Figure 6-3. Here a qualitative assessment of the nanotube size can be made via a comparison of the slopes for the best-fit linear regressions for each preparation. Based on Equation 6-2,  $\Delta i$  versus  $\frac{1}{L}$  should yield a linear trend with the numerical value of the slope representing the product of  $n$ ,  $F$ ,  $\pi$ ,  $r^2$ ,  $D$ , and  $\Delta C$ . Since  $n$ ,  $F$ ,  $\pi$ ,  $D$ , and  $\Delta C$  remain constant for all experiments, a change in the nanotube area (i.e. a change in the nanotube radius) is assumed to be the sole variable affecting the magnitude of the slope. Figure 6-3 reveals that the PC+ preparation leads to a larger, more positive slope compared to the SBL preparation. In turn, a larger, more positive slope is observed for the SBL preparation compared to the PE+ preparation. Therefore, the nanotube diameters for these preparations can be qualitatively related as follows: tube diameter for PC+ > SBL > PE+.

An alternative method of comparing the data is to directly substitute  $\Delta i$  and  $L$  into Equation 6-1 to calculate the nanotube diameter (with the diameter being twice the calculated  $r$ ). The individually calculated nanotube diameters were then related to the corresponding nanotube lengths and the trend in the nanotube diameter as a function of nanotube length was observed (Figure 6-4). A slightly increasing trend as a function of nanotube length is observed for all preparations. Choosing all the data for each composition, the average calculated nanotube diameter for PC+, SBL, and PE+ was  $153 \pm 4$  nm,  $117 \pm 4$  nm, and  $57 \pm 1$  nm, respectively (Figure 6-5). Statistical analysis of these data provided that the average calculated diameters for the preparations were significantly different from each other at the 95% confidence interval using a Student's t-

test ( $p < 0.05$ ). This was also in agreement with the qualitative trend shown previously in Figure 6-3.

In addition to intrinsic curvature theory, membrane composition might be a factor in regulating nanotube size via membrane elastic free energy. The free energy of the membrane ( $F$ ) can be expressed as<sup>15</sup>

$$F = \int \frac{\kappa}{2} (2H)^2 dA + \sigma A - pV - fL \quad \text{Equation 6-3}$$

where  $\kappa$  is the bending rigidity of the membrane,  $H$  is the membrane mean curvature,  $A$  is the membrane surface area,  $\sigma$  is the surface tension of the membrane,  $p$  is the interior pressure of the volume ( $V$ ) enclosed by the membrane, and  $f$  is the point force necessary to pull and sustain the membrane a distance  $L$ . More specifically, if a membranous tube is considered, its free energy ( $F_{tube}$ ) for a specified tube length may be expressed as<sup>15</sup>

$$F_{tube} = \left[ \frac{\kappa}{2r^2} + \sigma \right] 2\pi rL - fL \quad \text{Equation 6-4}$$

where  $r$  is the nanotube radius. The surface tension is working to minimize the nanotube radius while, conversely, the bending rigidity is working to drive the expansion of the tube.<sup>15</sup> By taking the first derivative of  $F_{tube}$  with respect to nanotube radius ( $r$ ) and setting it equal to zero, an expression for the equilibrium nanotube radius ( $r_0$ ) can be written as

$$r_0 = \sqrt{\frac{\kappa}{2\sigma}}. \quad \text{Equation 6-5}$$

In the system presented here, the artificial cell model, an attached lipid reservoir in the form of a multilamellar component is directly adhered to the unilamellar parent vesicle.

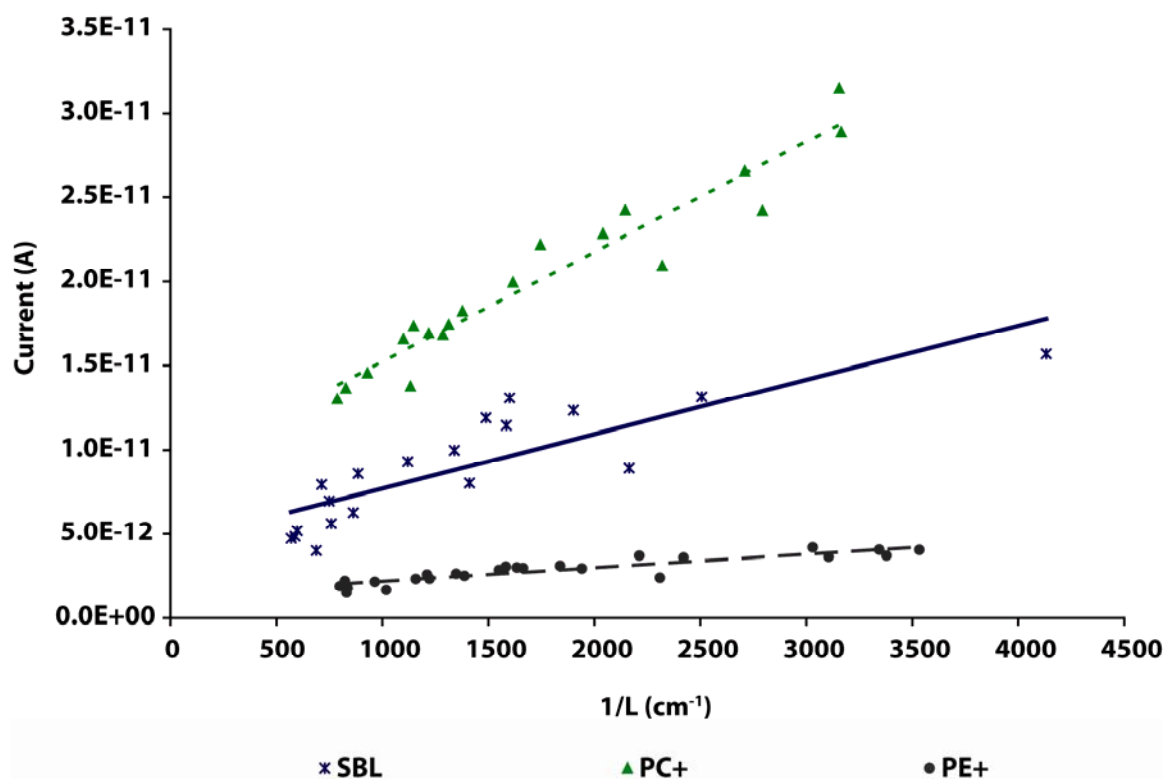


**Figure 6-3.** A plot of current versus  $\frac{1}{L}$  for control SBL, PC+, and PE+ for the tube-only configuration. A qualitative assessment of the nanotube diameter may be made using the magnitude of the slopes from the best-fit linear regression of each membrane composition. The slope for PC+ is greater than that of SBL. In turn, the slope of SBL is greater than that of PE+. Therefore, the qualitative relationship of the nanotube diameter for each preparation can be expressed as  $\text{PC+} > \text{SBL} > \text{PE+}$ .

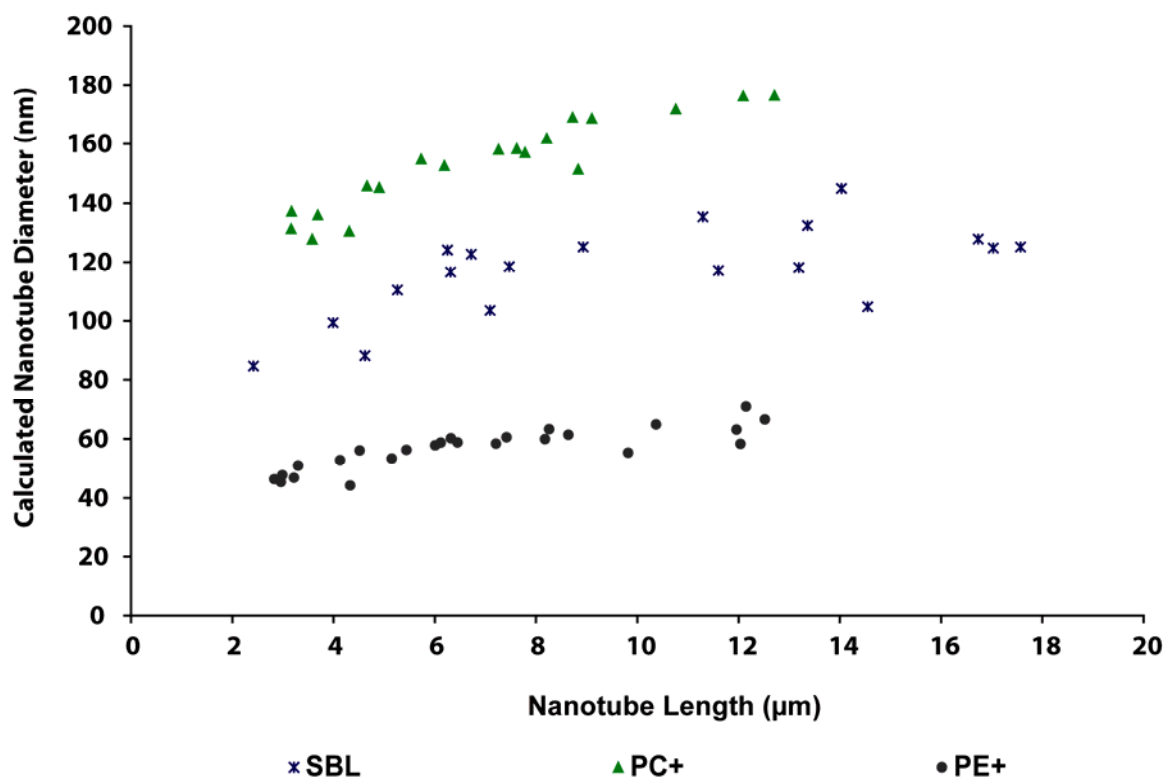


**Figure 6-4.** Calculated nanotube diameter as a function of nanotube length for control SBL, PC+, and PE+. The calculated diameter for each composition was relatively constant, albeit a slight positive slope as nanotube length increased. (n=19, 19, and 25 point measurements from 3 different liposomes for SBL, PC+, and PE+, respectively).



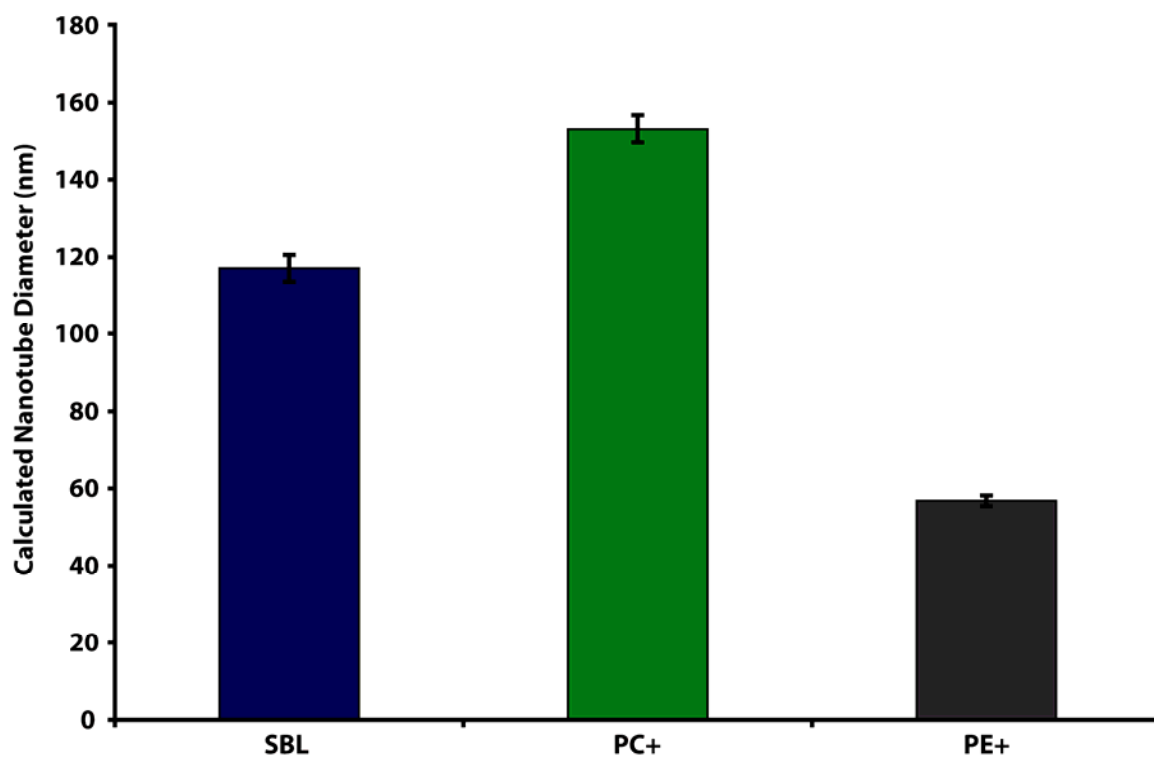


**Figure 6-5.** Average nanotube diameters for control soybean liposomes (SBL), elevated PC (PC+), and elevated PE (PE+) for the tube-only configuration. Each composition was statistically different from the other two treatments at the 95% confidence level (Student's t-test). (n=19, 19, and 25 point measurements from 3 different liposomes for SBL, PC+, and PE+, respectively). Error bars represent  $\pm$  SEM.

This reduces the surface tension term to a small and negligible constant. Therefore, a change in the apparent radius of the nanotube would be consequential to a change in the membrane bending rigidity, a parameter dependent on the membrane composition.<sup>16, 17</sup> Among other things, these data suggest that the dimensions of a tubular structure *in a live cell* might be fine-tuned via cellular regulation of the lipid composition in the organelles and in the inner versus outer leaflets. Of course, for this to be effective, the cells would have to have a means to rapidly and selectively transport or synthesize lipids to and at these structures, respectively.

## Conclusions

An artificial cell model for exocytosis was used to evaluate the effect of lipid composition on the size of tubule formation. Lipid tethers were pulled from the membrane of a giant unilamellar liposome to the inside of the liposome using a glass pipette filled with catechol solution. The diffusion of catechol from the tip of the pipette through the lipid nanotube and to the outside was monitored using steady-state electrochemical measurement methodology by placing a carbon fiber microelectrode at the nanotube outlet. A diffusion-based model was used to determine the inner diameter of the lipid nanotube formed from liposomes made from soybean polar extract, soybean polar extract with elevated PC, or soybean polar extract with elevated PE.

Nanotube diameters were compared both qualitatively and quantitatively as a function of nanotube length. The average diameter of a lipid nanotube from SBL preparation was  $117 \pm 4$  nm, in agreement with previous estimations of nanotube diameters from this preparation.<sup>18, 19</sup> By augmenting the SBL lipids with 25% additional cylindrically-shaped lipid PC, the tubule size increased in size to  $153 \pm 4$  nm, and,

conversely, by adding 25% of the inverted cone-shape lipid PE into this liposome preparation, the average tubule size decreased in size to  $57 \pm 1$  nm. These data demonstrate that the intrinsic curvature of an elevated concentration of PC or PE lipids in a membrane made from a fairly complex lipid mixture is substantial enough to increase or decrease the level of curvature during tubule formation. This is accomplished via an alteration of the membrane bending rigidity of the nanotube. As a final comment, these data also exemplify that it is possible for phospholipids, without protein involvement, play an active role in controlling the dimensions of tubular structures *in vivo*.

## References

- (1) Sushmita, M.; Frederick, R. M. *Traffic* **2000**, *1*, 203-211.
- (2) Giusto, N. M.; Pasquare, S. J.; Salvador, G. A.; Ilincheta de Boschero, M. G. *J. Lipid Res.* **2009**, jlr.R001891.
- (3) Kiyan, J.; Smith, G.; Haller, H.; Dumler, I. *Biochemical Journal* **2009**, *423*, 343-351.
- (4) Cooper, J. R., Bloom, F.E., Roth, R.H. *The Biochemical Basis of Neuroparmacology*, 8th ed.; Oxford University Press: New York, 2003.
- (5) Roman, S. P.; Mariagrazia, C.; Elena, V. P. *FEBS Letters* **2009**.
- (6) Smith, C. U. M. *Elements of Molecular Neurobiology*, 3rd ed.; John Wiley & Sons: West Sussex, 2002.
- (7) Ostrowski, S. G.; Van Bell, C. T.; Winograd, N.; Ewing, A. G. *Science* **2004**, *305*, 71-73.
- (8) Uchiyama, Y.; Maxson, M. M.; Sawada, T.; Nakano, A.; Ewing, A. G. *Brain Res* **2007**, *1151*, 46-54.
- (9) Durgbanshi, A.; Kok, W. T. *Journal of Chromatography A* **1998**, *798*, 289-296.
- (10) Hirschberg, K.; Miller, C. M.; Ellenberg, J.; Presley, J. F.; Siggia, E. D.; Phair, R. D.; Lippincott-Schwartz, J. *J Cell Biol* **1998**, *143*, 1485-1503.
- (11) Polishchuk, R. S.; Polishchuk, E. V.; Marra, P.; Alberti, S.; Buccione, R.; Luini, A.; Mironov, A. A. *J Cell Biol* **2000**, *148*, 45-58.
- (12) Kalin, N.; Fernandes, J.; Hrafnisdottir, S.; van Meer, G. *J Biol Chem* **2004**, *279*, 33228-33236.

- (13) Verkleij, A. J.; Zwaal, R. F.; Roelofsen, B.; Comfurius, P.; Kastelijn, D.; van Deenen, L. L. *Biochim Biophys Acta* **1973**, *323*, 178-193.
- (14) Zwaal, R. F.; Roelofsen, B.; Comfurius, P.; van Deenen, L. L. *Biochim Biophys Acta* **1975**, *406*, 83-96.
- (15) Derenyi, I.; Julicher, F.; Prost, J. *Phys Rev Lett* **2002**, *88*, 238101.
- (16) Rawicz, W.; Olbrich, K. C.; McIntosh, T.; Needham, D.; Evans, E. *Biophys J* **2000**, *79*, 328-339.
- (17) Tian, A.; Capraro, B. R.; Esposito, C.; Baumgart, T. **2009**, *97*, 1636-1646.
- (18) Karlsson, M.; Sott, K.; Cans, A. S.; Karlsson, A.; Karlsson, R.; Orwar, O. *Langmuir* **2001**, *17*, 6754-6758.
- (19) Tokarz, M.; Hakonen, B.; Dommersnes, P.; Orwar, O.; Akerman, B. *Langmuir* **2007**, *23*, 7652-7658.

## Chapter 7

### Future Directions and Thesis Conclusions

#### Introduction

Several new, original, and mainly electrochemistry-based approaches aimed toward gaining a better understanding of release via the exocytosis process have been presented in this thesis. Both biological and artificial model systems were implemented, each having their own inherent advantages and challenging intricacies. Due to the complex nature of both exocytosis and these implemented model systems, many vastly different research directions could be pursued based on the body of work presented here. A few such areas will be briefly explored and put into context in this chapter.

**Hypotonic conditions and cellular release.** In Chapter 2, the effects high osmolarity (hypertonic) saline have on exocytosis were examined, particularly the number of pre-spike “feet” and the total amount of transmitter released in these feet compared to the entire vesicular fusion event. However, the alternative i.e. low osmolarity, hypotonic conditions was not examined. It was concluded in Chapter 2 that the high osmolarity condition decreased the total tension differential (through the fusion pore) between the fusing vesicle and the cell plasma membrane by reducing the membrane tension of the plasma membrane (visualized by wrinkling of the cell membrane). This yielded a more stable, longer-lasting fusion pore, thus leading to an increased number of observed feet as well as an increased amount of neurotransmitter able to escape via the fusion pore. One would presume that if given low osmolarity, hypotonic conditions, a greater tension differential through the pore may be present due to an increased tension of the plasma membrane. This increased membrane tension could be invoked by swelling the cell. For

example, glial cells had increased cell volumes to as much as 35% of their original control volumes upon exposure to hypotonic conditions.<sup>1</sup> Therefore, one might hypothesize under hypotonic conditions that the foot frequency would decrease and less transmitter molecules would be released during the foot as compared to hypertonic conditions, adding to the body of evidence that membrane biophysics is an important component in regulating release via the fusion pore.

Preliminary results suggest the number of feet observed in hypotonic conditions as well as the number of transmitter molecules released per foot event is not different compared to isotonic saline control; however, the average number of transmitter molecules released per vesicle surprisingly increased to a similar level observed for generation-matched PC12 cells probed in hypertonic conditions. This was unexpected because the differences in membrane tension across the fusion pore are inverse to each other. In the case of hypertonicity, a lipid flow through the pore compensated this tension differential from the normal tension of vesicle to the lower tension of plasma membrane. Hypotonic conditions, therefore, would be expected to have reverse lipid flow (i.e. toward the normal tension of vesicle from the now higher tension of the plasma membrane). Such reversal of lipid flow through the fusion pore, in part, explains the lack of feet seen in hypotonic conditions; however, the reason for an increased total amount of transmitter released per vesicle remains unclear. Borges and coworkers examined catecholamine release from bovine chromaffin cells under similar osmotic conditions and found release was more frequent and peak amplitudes were increased, yet total amount released was unchanged.<sup>2</sup> Furthermore, Amatore and coworkers similarly reported increased peak amplitudes yet unchanged total amount released upon investigating

chromaffin cells under hypo-osmotic conditions.<sup>3</sup> This contradictory result for PC12 cells should be examined further as it might be caused by differences in the vesicle machinery between PC12 and adrenal chromaffin cells.

**Exploiting the spatial resolution of microelectrode arrays.** In Chapter 3, the fabrication and characterization of a seven-barrel carbon fiber microelectrode array (MEA) was presented. The MEA was also utilized to study release of neurotransmitter molecules from single cells, a process traditionally studied using single carbon fiber microelectrodes. The temporal and spatial resolution afforded by the MEA allows sub-cellular release activity to be probed in a new and exciting way. Alternating the direction from which a secretagogue is introduced to a cell, for example, could reveal if the area of the cell closest to the secretagogue produces an electrochemical response first compared to other cell areas located farther away. If such a secretagogue location-dependency exists, how and where this response propagates over time could be determined. Furthermore, changing the origin from where the secretagogue was administered could affect the global release pattern of the cell. These are interesting questions that could potentially be answered through the practical use of MEAs.

**Coupling microelectrode arrays with calcium imaging.** Implementing an MEA simultaneously with a complimentary imaging technique, such as intracellular calcium imaging with FURA-2 previously described in Chapter 4, could also be valuable. Correlating calcium influx with “hot” and “cold” spots observed via the recorded electrochemical responses could be used to unravel a possible mechanism explaining the differences between these active and inactive cell areas. It would be more interesting to determine whether a change from a “hot” to a “cold” release spot exhibited a dependence



on a change in the intracellular calcium levels or if this change in activity was completely random.

**Utilizing microelectrode arrays in conjunction with E2.** Likewise, MEAs should also be useful for studying the inhibitory effects of estrogen as outlined in Chapter 4, particularly investigating the 10 nM and 50  $\mu$ M E2 concentrations, the two concentrations that promoted exocytotic release during their application. The use of MEAs could be used to determine the specific area(s) from which these release events originated from as well as uncover any specific pattern of release (from the cell center versus the cell rim, for example). Furthermore, MEAs could be used to visualize conversion of “hot” release spots to “cold” areas directly after estrogen treatment, suggesting a suppression of active release areas as a mode of inhibition. Another interesting possibility would be to determine if 10 nM and/or 50  $\mu$ M estrogen treatment increased the presence of “hot” spots during application and if these areas revert to dormant activity levels once the estrogen is removed. This would implicate a fast, reversible modulation by estrogen that would help further explain the vesicular release present during E2 application at these concentrations.

**Elucidating the involvement of an estrogen membrane receptor in the mechanism by which E2 inhibits exocytosis.** The possible involvement of an estrogen membrane receptor in the modulation of exocytotic release has been suggested.<sup>4-7</sup> A reliable and receptor-specific pharmacological agent is necessary to elucidate E2 membrane receptor involvement and has proven to be challenging. E2 linked to bovine serum albumin (E2-BSA) was implemented as it was thought to be membrane impermeable, thus allowing this E2 conjugate to only interact with E2 membrane receptors on the outer cell

membrane. Application of 10 nM and 50  $\mu$ M E2-BSA (concentration denoting the concentration of E2) resulted in inhibited exocytosis as observed with amperometry. This inhibition was similar to levels observed for free-estrogen concentration equivalents. These data were suggestive of E2 inhibiting release via an interaction with membrane receptors because E2-BSA was unable to transverse the cell membrane. Moreover, both 10 nM and 50  $\mu$ M E2-BSA treatments decreased the calcium influx post-treatment, implying inhibition of release could be partially due to a decreased influx of calcium modulated by an E2 membrane receptor. However, BSA alone also decreased the intracellular calcium levels after treatment, confounding the effect observed for E2-BSA. An alternative impermeable form of estrogen, or purified BSA, must be obtained to continue this investigation.

**Lysolipid addition and estimation of nanotube size.** The direct measurement of a lipid nanotube present in the artificial cell model for exocytosis was presented in Chapters 5 and 6. A critical difference between the tube-only and two-vesicle configurations at shorter nanotube lengths was presented in Chapter 5, and a theoretical model for the elastic free energy of different membrane structures comprising the model system subsequently supported this finding. Membrane composition and lipid curvature theory and the effect of increased lipid concentration in the membrane were examined in Chapter 6. Lipid composition has a direct effect on the measured size of the lipid nanotube, therefore implicating a more active role for phospholipids in size determination of nanostructures present in nature. One lipid that was not considered in Chapter 6 was a lysolipid, or a phospholipid containing only one acyl chain tailgroup, and thus categorizing it as a positive curvature lipid. This lipid would preferentially accumulate in

the outer leaflet of the bilayer and affect the bending modulus of both the nanotube and the neck regions much like negative curvature lipids. Preliminary attempts to prepare liposomes with 250  $\mu\text{g}$  of lysophosphatidylcholine and 750  $\mu\text{g}$  soybean polar lipid extract have been unsuccessful with a lack of workable liposomes forming upon rehydration. This is understandable, as soybean polar lipid extract does not contain lysophosphatidylcholine.<sup>8</sup> Relatively large additions of such a structurally different lipid might be too disruptive to the membrane environment for proper liposome formation. Smaller, incremental additions of lysophosphatidylcholine are planned for future experiments.

**Measuring a lipid nanotube constructed from a liposome-lipid nanotube system within a “blebbed” cell.** Altering the membrane composition to more closely mimic cellular membranes is an exciting challenge that would benefit from the use of “blebbed” cells to create the liposome-lipid nanotube system.<sup>9</sup> Briefly, a bleb can be formed by loosening/detaching membrane material from the cell cytoskeleton by way of incubation in a formaldehyde-based blebbing solution. This loosened membrane material forms a structure analogous that of the unilamellar vesicle in the artificial cell model for exocytosis. However, the bleb has the numerous membrane proteins associated with the cell incorporated into its structure. These proteins constitute a major cellular component that is absent in the artificial cell model that would be interesting to examine with respect to their effect on the nanotube measurements obtained in Chapters 5 and 6.

**Inducing lipid phase separation within the liposome-lipid nanotube system.** Vesicles constructed from various lipid mixtures have been shown to have distinct separation into different lipid phases upon changes in temperature.<sup>10</sup> Lipid domain position, moreover,

can be influenced by the environment which they encapsulate.<sup>11</sup> It would be interesting to induce a lipid phase separation in the liposome-lipid nanotube system after a nanotube was pulled and observe the effect this phase separation would have on the measured inner diameter. Moreover, the reversibility of the phase separation in such a specialized configuration would be interesting to monitor by simultaneous optical and electrochemical methods as this might provide insights into how cells control the diameter of processes that extend from the cell body.

## **Conclusions**

In this thesis, electrochemical detection at single or multiple microelectrodes was employed in conjunction with complimentary optical microscopy techniques to investigate fundamental aspects related to exocytosis, an important process facilitating neuronal communication. Both biological and artificial cell model systems were implemented in these projects, allowing individual parameters such as membrane mechanics, for example, to be examined in two different yet comparable environments. In Chapter 2, the effects of increased osmolarity on vesicular exocytosis from PC12 cells were examined using carbon fiber amperometry. The number of pre-spike “feet” and the amount of transmitter released during these feet were notably increased compared to isotonic saline control, a finding that strongly suggested membrane biophysics plays a modulatory role in vesicular release by way of fusion pore stabilization. The fabrication and characterization of a seven-barrel carbon fiber microelectrode array were presented in Chapter 3. Here, too, release from single PC12 cells was monitored amperometrically, a process traditionally studied with a single electrode atop the cell. The high spatial resolution of the tightly-packed, individually-addressable microelectrodes allowed the

resolution of exocytotic release at the sub-cellular level. In Chapter 4, the inhibitory effect estrogen has on depolarization-induced release from PC12 cells was discovered to be dose-dependent and to be regulated via N-type voltage-gated calcium channels, both results previously not reported for this neuromodulator. Two concentrations of E2 (10 nM and 50  $\mu$ M) elicited release observed with amperometry; however, intracellular calcium imaging with FURA-2 revealed that calcium influx was significantly decreased for 10 nM E2 yet unaffected for 50  $\mu$ M E2. This suggested that E2 may act through two mechanisms: at low (physiological) levels, E2 might inhibit release by affecting VGCCs and at higher, potentially pharmacological levels, E2 might directly affect overall cell function. Such dissimilarity is important to consider when postulating a neuroprotective mechanism of estrogen. In Chapters 5 and 6, the direct measurement of a lipid nanotube present in the artificial cell model for exocytosis was presented. A critical difference between the tube-only and two-vesicle configurations at shorter nanotube lengths was presented in Chapter 5, and this result was subsequently supported by a theoretical model considering the elastic free energy of the different membrane structures comprising the model system. In Chapter 6, membrane composition, lipid curvature theory, and the effect of increased lipid concentration in the membrane were explored. Lipid composition was shown to directly affect the measured size of the lipid nanotube, therefore implicating a more active role for phospholipids in size determination of nanostructures present in nature. The combined application of the ideas, methods, and model systems presented in this thesis provide great potential to advance our current understanding of the exocytotic release process and to further detail the role membrane biophysics has at the single- and sub-cellular level.

## References

- (1) Chvátal, A.; Anderová, M.; Kirchhoff, F. *Journal of Anatomy* **2007**, *210*, 671-683.
- (2) Borges, R.; Travis, E. R.; Hochstetler, S. E.; Wightman, R. M. *J Biol Chem* **1997**, *272*, 8325-8331.
- (3) Amatore, C.; Arbault, S.; Bonifas, I.; Bouret, Y.; Erard, M.; Guille, M. *Chemphyschem* **2003**, *4*, 147-154.
- (4) Filardo, E.; Quinn, J.; Pang, Y.; Graeber, C.; Shaw, S.; Dong, J.; Thomas, P. *Endocrinology* **2007**.
- (5) Fiorini, S.; Ferretti, M. E.; Biondi, C.; Pavan, B.; Lunghi, L.; Paganetto, G.; Abelli, L. *Endocrinology* **2003**, *144*, 3359-3367.
- (6) Machado, J. D.; Alonso, C.; Morales, A.; Borges, R. *Ann N Y Acad Sci* **2002**, *971*, 284-286.
- (7) Mermelstein, P. G.; Becker, J. B.; Surmeier, D. J. *J Neurosci* **1996**, *16*, 595-604.
- (8) Avanti Polar Lipids.
- (9) Bauer, B.; Davidson, M.; Orwar, O. *Langmuir* **2006**, *22*, 9329-9332.
- (10) Veatch, S. L.; Keller, S. L. *Biophys J* **2003**, *85*, 3074-3083.
- (11) Cans, A. S.; Andes-Koback, M.; Keating, C. D. *J Am Chem Soc* **2008**, *130*, 7400-7406.

## VITA

**Kelly L. Adams**

### EDUCATION

**Ph.D. Chemistry**, The Pennsylvania State University, May 2010.

**B.S. Chemistry**, State University of New York College at Oneonta, May 2004.

### AWARDS

**Apple Fellowship**, The Pennsylvania State University, 2008-2009.

**Dan Waugh Teaching Award**, October 2005 & 2006.

**Department of Chemistry Travel Award**, February 2006.

**Roberts Graduate Fellowship**, August 2004.

**Binghamton ACS Award in Chemistry**, May 2004.

### PUBLICATIONS

Label-free imaging of exocytosis in neuroendocrine cells by using ultra-thin pH optodes as cell growth platforms. N. Strömberg, M. Puchades, **K.L. Adams**, A.G. Ewing. *In preparation for Anal. Chem.*

Estradiol inhibits depolarization-induced exocytosis in PC12 cells via N-type voltage-gated calcium channels. **K.L. Adams**, M.M. Maxson, L. Mellander, R.H.S. Westerink, A.G. Ewing. *In preparation for J. Neurosci. Res.*

Lipid membrane composition regulates the diameter of a lipid nanotube in an artificial cell model. **K.L. Adams**, J. Engelbrektsson, M. Voinova, A.G. Ewing, A.-S. Cans. *In preparation for Langmuir.*

An *in situ* fracture device to image lipids in single cells using ToF-SIMS. I. Lanekoff, M.E. Kurczy, **K.L. Adams**, J. Malm, R. Karlsson, P. Sjövall, A.G. Ewing. *Submitted to Surface and Interface Analysis.*

Steady-state electrochemical detection of lipidic nanotube diameter utilizing an artificial cell model. **K.L. Adams**, J. Engelbrektsson, M. Voinova, B. Zhang, D.J. Eves, R. Karlsson, M.L. Heien, A.-S. Cans, A.G. Ewing. *Anal. Chem.* **2010**, 82, 1020-1026.

*In Vitro* Electrochemistry of Biological Systems. **K.L. Adams**, M. Puchades, A.G. Ewing. *Annual Rev. Anal. Chem.* **2008**, 1, 329-355.

Spatially and temporally resolved single-cell exocytosis utilizing individually addressable carbon microelectrode arrays. B. Zhang, **K.L. Adams**, S. J. Lubner, D.J. Eves, M.L. Heien, A.G. Ewing. *Anal. Chem.* **2008**, 80, 1394-1400.

High osmolarity and L-DOPA augment release via the fusion pore in PC12 Cells. L.A. Sombers, N. J. Wittenberg, M. M. Maxson, **K.L. Adams**, A.G. Ewing. *Chem. Phys. Chem.* **2007**, 8, 2471-2477.